Département de Physique
Université de Fribourg (Suisse)

Re-examination of $M_{2,3}$ atomic level widths of elements $69 \leq Z \leq 95$ and Double K-shell ionization of Al induced by photon and electron impact

THESE

Présentée à la Faculté des Sciences de l'Université de Fribourg (Suisse)
pour l'obtention du grade de *Doctor rerum naturalium*

Karima Fennane
du
Maroc

Numéro de la thèse:
1597

Imprimerie Saint-Paul, Fribourg
2008

Acceptée par la Faculté des Sciences de l'Université de Fribourg (Suisse) sur proposition de :

Prof. Dr. Dionys Baeriswyl, Université de Fribourg, Président du Jury,
Prof. Dr. Jean-Claude Dousse, Université de Fribourg, Directeur de Thèse,
Prof. Dr. Gunther L. Borchert, Université technique de München (Allemagne), Rapporteur,
Dr. Joanna Hoszowska, Université de Fribourg, Rapporteure.

Fribourg, le 18 Mars 2008

Le directeur de thèse : Le doyen :

Prof. Dr. Jean-Claude Dousse Prof. Dr. Titus Jenny

Contents

Abstract 1

Résumé 4

Part I: Re-examination of $M_{2,3}$ atomic level widths of elements $69 \leq Z \leq 95$ 7
1. Introduction 8
   1.1 Motivation 8
   1.2 Atomic level widths 10
   1.3 Experimental methods to determine atomic level widths 10
   1.4 Spectral line shape 12
   1.5 Content of the present work 12
2. Experiment 13
   2.1 Choice of the proper x-ray emission lines 13
   2.2. Experimental setup 13
      2.2.1 Measurements of the elements $81 \leq Z \leq 95$ 14
      2.2.2 Measurements of the elements $69 \leq Z \leq 77$ 16
3. Data analysis 20
4. Results and discussion 32
   4.1 $L_1M_{2,3}$ transition energies 32
   4.2 $L_1M_{2,3}$ transition widths 35
   4.3. $M_{2,3}$ atomic level widths 38
      4.3.1 Theoretical $M_{2,3}$ atomic level widths 38
      4.3.2. Experimental $M_{2,3}$ atomic level widths 39
         4.3.2.1 M_3 level widths 40
         4.3.2.2 M_2 level widths 44
5. Concluding remarks 46
Bibliography 48

Part II: Double K-shell ionization of Al induced by photon and electron impact. 53
1. Introduction 54
   1.1 Motivation 54
   1.2 Methods to produce double 1s vacancy states 55
   1.3 Experimental methods to detect double 1s vacancy states 57
   1.4. Hypersatellite x-ray lines 59
      1.4.1 Selection rules 59
      1.4.2 Energies 60
      1.4.3 Natural widths 60
      1.4.4 Relative intensities 61
   1.5 Content of the present work 61
2. Measurements with synchrotron radiation 62
   2.1. Experiment 62
      2.1.1 Beam line setup 62
      2.1.2 Von Hamos setup 62
      2.1.3 Method of data acquisition 63

2.2. Data analysis 64
2.2.1 Beam profile correction 64
2.2.2 Intensity normalisation 65
2.2.3 Self absorption correction 66
2.2.4 Energy calibration and spectrometer resolution 67
2.2.5 Overlap with the KβL$^{(2)}$ spectra 68
2.2.6 Analysis of the Kα hypersatellite spectra 70
2.3 Results 72
3. Measurements with electrons 74
3.1. Experiment 74
3.1.1 Experimental setup 74
3.1.2 Method of data acquisition 76
3.2. Data analysis 77
3.2.1 Beam profile correction and data normalisation 77
3.2.2 Average energy calculations 78
3.2.3 Analysis of the Kα hypersatellite spectra 79
3.3 Results 85
4. Discussion 87
4.1. Results from synchrotron radiation measurements 87
4.1.1 $K\alpha_2^h$ Energy 87
4.1.2 $K\alpha_2^h$ line width 88
4.1.3 $K\alpha_2^h L$ satellite 88
4.2 Results from electron measurements 89
4.3 Double K-shell photo-ionization probabilities 90
4.4 Comparison between the double to single K-shell ionization cross sections produced by photon and electron impact 93
5. Concluding remarks and future perspectives 99
Bibliography 101

Acknowledgements 111

Curriculum Vitae 113

List of publications 114

Abstract

The present Ph.D. thesis contains two different research projects in Atomic Physics, whose common denominator is high-resolution x-ray emission spectroscopy. The first project belongs to the field of x-ray transition metrology and concerns the determination of the M_2 ($3p_{1/2}$) and M_3 ($3p_{3/2}$) level widths of elements with atomic numbers in the region $69 \leq Z \leq 95$. The second part is devoted to the investigation of double K-shell ionization of metallic aluminium induced by photon and electron impact.

The x-ray transition metrology project of the L_1M_2 and L_1M_3 x-ray transitions widths for elements ranging from Thulium (Z=69) to Americium (Z=95) was incited by the work of Professor J. L. Campbell from the University of Guelph, Canada. Campbell et al. had assembled recently a large number of experimental data from which they derived an internally consistent set of level widths for the K shell to the N_7 subshell for all elements across the periodic table [At. Data Nucl. Data Tables **77**, 1 (2001)]. In the plot representing the variation of the M_3 level width as a function of the atomic number Z, the authors found a hump around Z=83 which is not predicted by the DHS (Dirac-Hatree-Slater) theoretical calculations. Campbell had suspected the L_1M_3 transitions widths measured by J.N. Cooper [Phys. Rev. **65**, 155 (1944)], which were the main source of his recommended M_3 level widths in the Z region $75 \leq Z \leq 92$, to be too high and had suggested that new high resolution measurements of these transitions would be useful to clarify the Z dependence of the M_3 level width. Furthermore, as Campbell's M_2 recommended level widths in this Z region are also based on the L_1M_2 transition widths of Cooper, a new set of measurements for the L_1M_2 transitions widths was called for.

The measurements were performed at the University of Fribourg by means of two different high resolution crystal spectrometers. Elements up to $_{77}$Ir were measured with a reflection-type von Hamos crystal spectrometer. As this instrument cannot be used efficiently for photon energies above 11 keV, elements with higher atomic numbers were measured with a transmission-type DuMond crystal spectrometer. The fluorescence x-ray emission was produced by irradiating the samples with the bremsstrahlung of an x-ray tube.

From the linewidths of the measured L_1M_2 and L_1M_3 x-ray transitions of $_{69}$Tm, $_{70}$Yb, $_{71}$Lu, $_{73}$Ta, $_{74}$W, $_{75}$Re, $_{77}$Ir, $_{81}$Tl, $_{83}$Bi and $_{95}$Am an accurate set of M_2 and M_3 level widths was determined assuming for the L_1 level widths the values reported recently by Raboud [Phys.

Rev. A **65**, 022512 (2002)]. Furthermore, the experimental $M_{2,3}$ data set was extended to $_{80}$Hg, $_{90}$Th and $_{92}$U, using former $L_1M_{2,3}$ high-resolution XES measurements performed by the Fribourg group. A detailed comparison of the determined M_2 and M_3 level widths with those recommended by Campbell and other available experimental data as well as theoretical predictions was done. The obtained values for the $M_{2,3}$ widths were found to be higher than the tabulated ones and lower than the independent-particle model predictions. In general, present results are 3-5 times more accurate than the former existing data. The observed abrupt changes of the $M_{2,3}$ level widths versus atomic number Z could be explained satisfactorily by the cut-offs and onsets of the $M_2M_4N_1$, respectively $M_3M_4N_{3,4,5}$ and $M_3M_5N_{2,3}$ CK (Coster-Kronig) transitions deduced from the Z+1 semi-empirical rule.

As a spin-off result of this study, precise L_1M_2 and L_1M_3 transition energies were obtained for the investigated elements. A very good agreement with MBPT theoretical values was found.

The second project concerns the investigation of double K-shell ionization of metallic aluminium induced by photon and electron impact. Two objectives were set for this project. The first was to overcome the lack of experimental data on double K-shell ionization in light elements. The second was to investigate the energy dependence of both the photon- and electron-induced double to single 1s ionization cross section from threshold to the expected broad maximum in order to better understand the mechanisms by which the double 1s vacancy production is achieved in each case. The x-ray synchrotron based measurements of the double to single photoionization cross sections for Al represent the first of the kind.

The experimental method consisted to measure the Kα hypersatellites spectra resulting from the radiative decay of the double K-shell vacancy states by means of high resolution x-ray emission spectroscopy using the Fribourg Bragg type von Hamos crystal spectrometer. Measurements of the photon-induced spectra were carried out at the x-ray microscopy beam line ID21 at the European Synchrotron Radiation Facility (ESRF), Grenoble, France, whilst those of the electron-induced spectra were performed at the University of Fribourg. The double to single 1s ionization cross sections were derived from the hypersatellite $K\alpha_2$ ($[1s^{-2}] \rightarrow [1s^{-1}2p_{1/2}^{-1}]$) to diagram ($[1s^{-1}] \rightarrow [2p^{-1}]$) line intensity ratios for photon beam energies ranging between 3122 eV and 5451 eV and for different incident electron beam energies ranging from 4 keV to 20 keV.

The energy-dependent evolution of the double 1s ionization probability for photon and electron impact was compared. It was found that the maximum value of the ratio of double to single ionization cross section P_{KK} for electron impact of $9.81 \cdot 10^{-5}$ is well below the one obtained with photons of $1.65 \cdot 10^{-3}$. This difference is discussed in terms of the residual ion's

recoil momentum in case of photo-absorption and projectile impact ionization. The threshold energy for the production of double K-shell vacancies was estimated to be comprised between 3235 eV and 3318 eV in the case of photoionization and at about 4.6 keV for the electron-induced ionization.

The energy and linewidth of the $K\alpha_2$ hypersatellite x-ray emission line were also determined. Both the photon and electron impact data lead to consistent results of 1610.38(10) and 1610.37(11) respectively for the $K\alpha_2$ hypersatellite transition energy and 1.88(10) eV and 1.87(17) eV for the linewidth. No trace of the $K\alpha_1$ ($[1s^{-2}] \rightarrow [1s^{-1}2p_{3/2}^{-1}]$) hypersatellite transition was detected in the measured x-ray spectra due the prevailing LS coupling scheme for light elements.

Moreover, it was found that the evolution of the measured double to single K-shell photoionization cross section with photon energy deviates considerably from the predictions of the Thomas model based on the time-dependent perturbation theory and accounting solely for the shake process. These findings evince the relative importance of the electron-electron scattering contribution to the double 1s ionization for Al. The P_{KK} value in the maximum of the double ionization cross-section was compared to the Z-dependence of P_{KK} reported by Kanter et al. in [Phys. Rev. A 73, 062712 (2006)]. A good agreement with the value deduced from the proposed scaling law $1/Z^{1.6}$ for neutral elements was obtained.

Résumé

Ce travail de thèse en physique atomique expérimentale comprend deux études distinctes dont le dénominateur commun est la spectroscopie X de haute résolution. La première étude s'inscrit dans le domaine de la métrologie des rayons X et concerne la détermination de la largeur des niveaux atomiques $3p_{1/2}$ (sous-couche M_2) et $3p_{3/2}$ (sous-couche M_3) des éléments ayant un numéro atomique $69 \leq Z \leq 95$. La deuxième étude concerne la double ionisation K de l'aluminium produite par l'impact de photons et d'électrons.

Le projet de métrologie de rayons X dont l'objectif était de déterminer les largeurs naturelles des sous-couches atomiques M_2 et M_3 nous a été suggéré par le professeur J. L. Campbell de l'Université de Guelph, Canada. Campbell et Papp ont publié récemment une synthèse des résultats expérimentaux concernant les largeurs naturelles de transitions atomiques dont ils ont extrait un ensemble auto-consistant des largeurs des couches atomiques K à N_7 de tous les éléments du tableau périodique [At. Data Nucl. Data Tables **77**, 1 (2001)]. Dans le graphique représentant la variation de la largeur de la sous-couche M_3 en fonction du numéro atomique Z, les auteurs ont observé une bosse centrée autour de Z = 83 qui n'est pas prédite par les calculs théoriques DHS (Dirac-Hartree-Slater). Les valeurs recommandées par Campbell et Papp pour les largeurs du niveau $3p_{3/2}$ dans la région $75 \leq Z \leq 92$ ayant été extraites principalement des largeurs des transitions L_1M_3 mesurées par J. N. Cooper plus de 50 ans auparavant [Phys. Rev. **65**, 155 (1944)], Campbell a suggéré que ces anciennes valeurs étaient peut être surestimées et que de nouvelles mesures de haute résolution des transitions L_1M_3 seraient donc très utiles pour clarifier la dépendance en Z des largeurs M_3. Comme les valeurs recommandées par Campbell et Papp pour la largeur du niveau atomique M_2 dans la région $75 \leq Z \leq 92$ avaient aussi été déduites des mesures de Cooper, il nous a paru judicieux d'étendre nos mesures aux transitions L_1M_2.

Les mesures ont été effectuées à l'Université de Fribourg au moyen de deux spectromètres à cristal courbé de haute résolution. Les éléments jusqu'à $_{77}$Ir ont été mesurés avec le spectromètre de type réflexion von Hamos. Toutefois, comme cet instrument ne peut pas être utilisé pour des photons ayant une énergie plus grande que 11 keV environ, les éléments les plus lourds ont été mesurés avec le spectromètre de type transmission DuMond. La fluorescence des échantillons a été produite en irradiant les cibles avec le bremsstrahlung d'un tube de rayons X.

A partir des largeurs mesurées des transitions L_1M_2 et L_1M_3 des éléments $_{69}$Tm, $_{70}$Yb, $_{71}$Lu, $_{73}$Ta, $_{74}$W, $_{75}$Re, $_{77}$Ir, $_{81}$Tl, $_{83}$Bi et $_{95}$Am et en utilisant les largeurs du niveau atomique L_1 déterminées récemment par Raboud et al. [Phys. Rev. A **65**, 022512 (2002)], des résultats précis et fiables concernant les largeurs naturelles des sous-couches M_2 et M_3 ont été obtenus. De surcroît, la nouvelle base de données pour les largeurs $M_{2,3}$ déduite de nos mesures a été étendue à $_{80}$Hg, $_{90}$Th et $_{92}$U en utilisant les résultats de mesures des transitions $L_1M_{2,3}$ effectuées précédemment par notre groupe. Nous avons comparé nos résultats avec les valeurs recommandées par Campbell et Papp et avec d'autres valeurs expérimentales et théoriques reportées dans la littérature. D'une manière générale, les largeurs $M_{2,3}$ obtenues dans ce travail sont plus grandes que celles de Campbell et Papp mais plus petites que les valeurs prédites par des calculs théoriques basés sur le modèle de particules indépendantes. Nos résultats sont aussi 3-5 fois plus précis que les quelques résultats antérieurs existants. Les abrupts changements observés dans les graphes représentant la variation des largeurs M_2 et M_3 en fonction du nombre atomique Z ont pu être expliqués de façon satisfaisante par le fait que les transitions Coster-Kronig $M_2M_4N_1$, respectivement $M_3M_4N_{3,4,5}$ et $M_3M_5N_{2,3}$, deviennent soudainement interdites ou au contraire permises pour certains éléments. La plupart des valeurs Z pour lesquels ces sauts dans les largeurs $M_{2,3}$ apparaissent ont pu être expliquées par la règle semi-empirique Z+1.

Des mesures de ce premier projet, nous avons également pu extraire un ensemble d'énergies précises et fiables pour les transitions L_1M_2, et L_1M_3 des 10 éléments énumérés ci-dessus. Un excellent accord a été trouvé entre nos énergies expérimentales et les valeurs théoriques prédites par des calculs MBPT (many body perturbation theory).

Le deuxième projet est une étude de la double ionisation K de l'aluminium métallique produite par l'impact de photons et d'électrons. Deux objectifs avaient été ciblés pour cette étude. Le premier visait à combler le manque de données expérimentales concernant la double ionisation K des éléments légers. Le deuxième but était d'étudier la dépendance en énergie du rapport des sections efficaces d'ionisation double et simple de la couche K depuis le seuil de production de doubles lacunes 1s jusqu'à la région du « broad maximum ». Ce deuxième objectif revêtait une importance particulière pour mieux comprendre les mécanismes par lesquels la double ionisation K est produite, aussi bien dans le cas du bombardement de l'échantillon par un faisceau d'électrons que dans celui de la photo-ionisation. On mentionnera ici qu'aucune mesure du rapport des sections efficaces de photo-ionisation double et simple de la couche K de l'aluminium n'a été effectuée avant cette thèse.

La méthode expérimentale adoptée a consisté à mesurer les spectres des transitions hypersatellites Kα résultant de la désexcitation radiative des états doublement ionisés $1s^{-2}$. Les

transitions hypersatellites ont été mesurées en haute résolution en utilisant le spectromètre von Hamos de Fribourg. Les mesures de photo-ionisation ont été effectuées auprès de la source de rayonnement synchrotronique européenne (ESRF), à Grenoble, France, alors que les mesures par impact d'électrons ont été effectuées à l'Université de Fribourg. Les rapports P_{KK} des sections efficaces d'ionisation double et simple de la couche K ont été déduits des intensités relatives des transitions hypersatellites $K\alpha_2$ ($[1s^{-2}] \rightarrow [1s^{-1}2p_{1/2}^{-1}]$) par rapport aux transitions diagrammes ($[1s^{-1}] \rightarrow [2p^{-1}]$). Les mesures ont été effectues pour des énergies de faisceau comprises entre 3122 eV et 5451 eV pour les photons et entre 4 keV et 20 keV pour les électrons.

Les dépendances en énergie des rapports P_{KK} obtenus avec les photons et les électrons ont été comparées. Nous avons trouvé que la valeur maximale du rapport était de $9.81 \cdot 10^{-5}$ dans le cas du bombardement d'électrons alors que pour la photo-ionisation une valeur maximale bien supérieure de $1.65 \cdot 10^{-3}$ a été obtenue. La différence a été expliquée par le transfert de quantité de mouvement sur l'ion résiduel, lequel transfert n'est pas le même dans les deux types de collisions. L'énergie de seuil pour produire une double ionisation K dans l'aluminium a pu être déduite des mesures. Elle est d'environ 4.6 keV dans le cas des électrons et comprise entre 3235 eV et 3318 eV dans celui du rayonnement synchrotronique.

Nous avons aussi déterminé l'énergie et la largeur naturelle de la transition hypersatellite $K\alpha_2$. Des valeurs consistantes de 1610.38(10) et 1610.37(11) pour l'énergie, et de 1.88(10) eV et 1.87(17) eV pour la largeur, ont été obtenues à partir des mesures effectuées, respectivement, avec les faisceaux de photons et d'électrons. Par contre, aucune trace de la transition hypersatellite $K\alpha_1$ ($[1s^{-2}] \rightarrow [1s^{-1}2p_{3/2}^{-1}]$) n'a été détectée dans nos mesures. Ceci n'est cependant pas surprenant car cette transition est interdite par les règles de sélection électriques dipolaires dans le modèle de couplage LS, lequel s'applique aux éléments légers comme l'aluminium.

Nos mesures ont aussi montré que la variation du rapport P_{KK} en fonction de l'énergie des photons incidents dévie considérablement des prédictions théoriques données par le modèle de Thomas. Ce modèle basé sur la théorie des perturbations dépendantes du temps ne prend en compte que les processus de « shake » si bien que le désaccord observé entre nos mesures et les prédictions de Thomas pour l'évolution du rapport P_{KK} met en évidence l'importance de la contribution de la diffusion électron-électron dans le processus de double photo-ionisation K. Finalement, la valeur maximale du rapport P_{KK} obtenue avec le rayonnement synchrotronique a été comparée à la valeur déduite de la récente étude de Kanter et al. [Phys. Rev. A 73, 062712 (2006)]. Un excellent accord a été trouvé, lequel tend à confirmer la dépendance en $1/Z^{1.6}$ proposée pour les éléments neutres dans le travail de Kanter.

Part I:

Re-examination of $M_{2,3}$ atomic level widths of elements $69 \leq Z \leq 95$

Chapter 1

Introduction

1.1 Motivation

Some years ago Campbell and Papp [1] presented an extensive set of K to N_7 atomic level widths for all elements across the periodic table, based upon a large number of literature experimental data. Their recommended M_2 and M_3 level widths were derived mostly from XPS (X-ray Photo-electron Spectroscopy) measurements for light elements and XES (X-Ray Emission Spectroscopy) measurements for elements above Z=54. For the XES measurements, Campbell and Papp extracted the M_2 and M_3 level widths mostly from the L_1M_2 and L_1M_3 line width measurements of Salem [2] and Cooper [3], assuming for the L_1 level widths their own recommended values [1] (see Fig.1).

More recently Raboud et al. [4] determined the L_1 atomic level width for several elements with atomic numbers $62 \leq Z \leq 83$ from high-resolution XES measurements of the quadrupole-allowed (E2) transitions $L_1M_{4,5}$, assuming for the $M_{4,5}$ level widths the values recommended by Campbell and Papp [1]. A fairly good agreement with Campbell's recommended L_1 level widths was found, except in the lanthanide region ($57 \leq Z \leq 70$) where a large discrepancy was observed. This discrepancy was explained by a splitting effect of the L_1 subshell resulting from the coupling in the initial excited state of the 2s electron spin with the total spin of the open 4f level. This splitting effect resulting in an increase of the L_1 level width that was not considered in the compilation of Campbell and Papp, it was concluded by Raboud et al. that the $M_{2,3}$ widths reported in [1] for the lanthanide region were too big. In other words, the bump occurring in the Campbell and Papp plot of the M_3 widths for $57 \leq Z \leq 70$ (see Fig. 1) is not real, since disappearing if the M_3 widths in this Z region are derived using the enhanced L_1 level widths observed for the lanthanides.

After the publication of Raboud's results, Campbell wondered whether the second bump occurring in the region $75 \leq Z \leq 92$ of the M_3 width plot could be also artificial as the first one. Actually Campbell found that the L_1 level widths in this Z region derived from L_1 Coster-Kronig and relative fluorescence yield measurements of Werner and Jitschin [5] were in

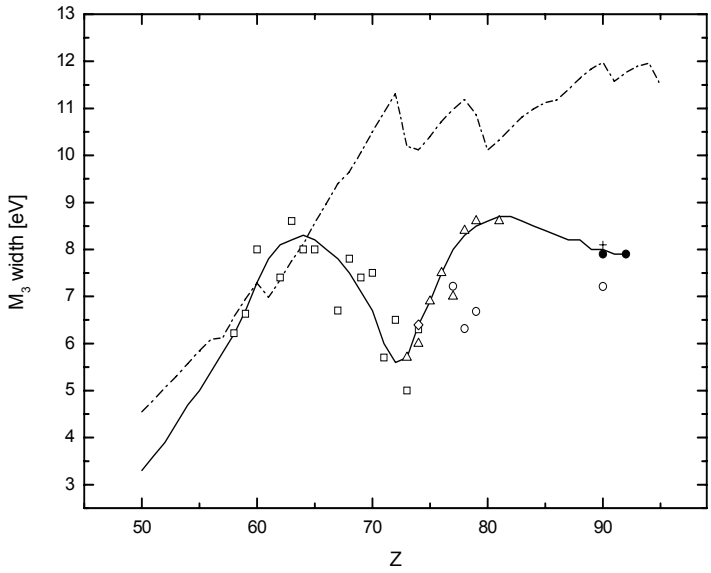

Fig. 1: (taken from Ref. [1]): Width of the M_3 level width versus atomic number Z. Experimental data were extracted from XES measurements using the following symbols: □ Ref. [2], Δ Ref. [3], ○ Ref. [6], ◊ Ref. [7], + Ref. [8], ● Refs. [9, 10]. The dashed dotted line represents the independent particle model calculations of Perkins et al [11], the solid line the recommended values of Campbell and Papp [1].

agreement with the new data of Raboud [4] and that both sets of values were significantly lower than the L_1 level widths obtained from the $L_1N_{2,3}$ XES measurements of Cooper [3] from which his L_1 level widths in the region $73 \leq Z \leq 81$ were mainly determined, using for the $N_{2,3}$ his own recommended values. Suspecting the widths of the $L_1M_{2,3}$ transitions measured by Cooper to be also overestimated, Campbell eliminated from his data base the M_3 level widths derived from these old measurements. Using then only the values determined from the newest L_1M_3 XES measurements [6, 7, 8, 9, 10] and the L_1 widths from Refs. [4, 5], he found that, as anticipated, there was no hump in this Z region of the M_3 plot but merely a smooth rise [12]. However, as these new XES data were scarce and strongly scattered, he suggested to perform a new series of modern XES measurements in order to obtain a more reliable data base for the M_3 level width in the region $75 \leq Z \leq 92$.

Following Campbell's suggestion, we undertook to perform a series of high-resolution XES measurements of the L_1M_3 transitions of $_{69}$Tm, $_{70}$Yb, $_{71}$Lu, $_{73}$Ta, $_{74}$W, $_{75}$Re, $_{77}$Ir, $_{81}$Tl, $_{83}$Bi and $_{95}$Am. As the single available L_1M_2 XES measurements in the region $75 \leq Z \leq 81$ were again those of Cooper, we decided to include in our measurements the L_1M_2 transitions. Furthermore, our experimental $M_{2,3}$ data set was extended to $_{80}$Hg, $_{90}$Th and $_{92}$U, using former $L_1M_{2,3}$ high-resolution XES measurements performed previously by our group [9, 10, 13].

1.2 Atomic level widths

An atomic inner-shell vacancy is usually filled with in a time interval of the order of 10^{-17} to 10^{-14} s. The mean lifetime τ of an atomic vacancy is related to the energy width Γ of the corresponding atomic level by the Heisenberg's uncertainty principle: $\tau \Gamma \cong \hbar$ ($\hbar$ is the Plank's constant divided by 2π). The energy width of a vacancy state is obtained by considering the sum of all decay probabilities. Neglecting the most improbable de-excitation modes, the width of a vacancy state is then given by the sum of the radiative, Auger and Coster-Kronig widths:

$$\Gamma = \Gamma_R + \Gamma_A + \Gamma_{CK} . \qquad (1)$$

Auger transitions are radiationless transitions in which the primary vacancy is filled by an electron from a higher shell with simultaneous ejection of an outer shell electron. Coster-Kronig transitions (CK) are particular Auger transitions in which at least one vacancy in the final state belongs to the same shell as the vacancy in the initial state. For instance, the Auger transition $L_1L_3M_5$ is a CK transition since there is one hole in the L-shell in the initial and final states. It should be noted that in equation (1) the CK width is excluded from the definition of the Auger width. The sum of the CK and Auger widths is sometimes named radiationless width in the literature. The probability that a vacancy in the shell S (S = K, L, M,…) becomes filled through a radiative decay is given by the fluorescence yield ω_S defined by:

$$\omega_S = \frac{\Gamma_{R,S}}{\Gamma_S} , \qquad (2)$$

where Γ_S and $\Gamma_{R,S}$ represent the total width, respectively the total radiative width, of the shell S. Note that the total decay probability W_S of the S vacancy and total radiative decay probability $W_{R,S}$ are related to the parent widths by:

$$W_S\left[s^{-1}\right] = \frac{\Gamma_S[eV]}{\hbar} \quad \text{and} \quad W_{R,S}\left[s^{-1}\right] = \frac{\Gamma_{R,S}[eV]}{\hbar} , \qquad (3)$$

with $\hbar = 6.582119 \cdot 10^{-16}\left[eV \cdot s\right]$

1.3 Experimental methods to determine atomic level widths

A vast number of spectroscopic techniques have been applied to measure the atomic level widths. The most usual are X-ray Absorption Spectroscopy (XAS), X-ray Photo-electron Spectroscopy (XPS), X-ray Emission Spectroscopy (XES) and Auger Electron Spectroscopy (AES).

In the x-ray absorption process, an atomic electron is transferred from a given atomic state to an empty bound state or to the continuum. Since there are a multitude of possible final states, the analysis of absorption spectra is generally difficult and does not lead to precise results. When the energy of the incoming photon is sufficiently high to ionise the target atom, one can investigate the energy spectra of the ejected photo-electrons (XPS) or decay products of the ionized atoms, namely the energy spectra of the Auger electrons (AES) or x-ray transitions (XES).

The XPS technique is a direct way to measure the atomic level widths since the photo-electron energy distributions reflect the widths of the states in which the atomic vacancies were produced. This technique requires, however, the use of γ-rays or monochromatic synchrotron radiation to avoid the broadening of the photo-electron line widths as a result of the energy scattering of the photon source. Ultra-high vacuum is also needed to avoid the re-absorption of the low energy photo-electrons. Furthermore, the XPS technique is extremely sensitive to the sample surface which should be extremely clean. The same conditions (monochromatized photon source, ultra-high vacuum and ultra-clean target surfaces) should be fullfilled in AES. In addition this technique has the disadvantage that the measured line widths reflect the combined effects of the widths of the three atomic levels involved in the considered Auger transition. Finally, XPS and AES spectra of solids are also influenced by phonon excitations which are generally considered to give a Gaussian broadening to the measured spectra (see Ref. [14] and references therein).

In XES, the measurements and spectra analysis are easier to perform, since this technique is less sensitive to the sample surface contamination and the measured spectra do not reflect the energy spread of the irradiation source, nor the energy losses of the incoming and outgoing particles. The spectra are neither affected by phonon excitations. However, here again, the measured line widths contain the contribution of the widths of the two atomic levels involved in the considered x-ray transition. In any of these spectroscopic methods, multi-ionization of the target atoms can lead to broadenings or asymmetries of the measured lines. This effect can be reduced by a proper choice of the irradiation source. In this respect, photon sources are particularly appropriate, multi-ionization being only possible via weak secondary mechanisms such as shake or TS1 processes.

Finally, it has to be mentioned that measured line profiles are always affected by the instrumental response of the employed detector or spectrometer. In most cases, the instrumental broadening varies with the energy of the particles to be detected. The observed energy distribution $f(E)$ results from the convolution of the "physical" distribution φ with the instrumental response ψ and can thus be written as:

$$f(E) = \int_0^{\infty} \varphi(E - E')\psi(E')dE' . \qquad (4)$$

As a consequence, the instrumental response should be determined accurately as a function of the energy and the measured lines deconvolved to obtain the natural line widths of the measured transitions.

1.4 Spectral line shape

When a core hole has a finite lifetime τ, all processes associated with the creation or filling of this hole are affected by a lifetime broadening. This lifetime broadening produces a Lorentzian contribution to the spectral line shapes which is given by:

$$I(E) = I(E_0)\frac{(\Gamma/2)^2}{(E - E_0)^2 + (\Gamma/2)^2}, \qquad (5)$$

Where E_0 is the centroid energy of the Lorentzian peak and Γ the core hole lifetime broadening or natural line width [14, 15].

The basic theory for the x-ray emission line widths was formulated by Weisskopf and Wigner in 1930 [16], following Dirac's radiation theory. In 1953, in a more sophisticated study based on modern quantum electrodynamics, Arnous and Heitler [17] concluded that the ''classical line shape'' of Weisskopf and Wigner is an excellent approximation to the exact result [18]. Denoting the initial state by *A* and the final state by *B*, they found in particular that a radiative transition has the following spectral distribution:

$$I(E)dE = \frac{(\Gamma_A + \Gamma_B)}{2\pi}\frac{dE}{(E_A - E_B - E)^2 + [(\Gamma_A + \Gamma_B)/2]^2} . \qquad (6)$$

The natural width of an x-ray transition line is given therefore by the sum of the widths of the initial and final atomic levels.

1.5 Content of the present work

In Chap. 2, the experimental technique employed to determine the M_2 and M_3 level widths and the two crystal spectrometers used for the measurements is described. The method of data analysis and the fitted x-ray spectra are presented in Chap.3. The obtained energies and line widths of the L_1M_2 and L_1M_3 transitions as well as the extracted M_2 and M_3 atomic level widths are presented and discussed in Chap. 4. Concluding remarks are given in Chap. 5.

Chapter 2

Experiment

2.1 Choice of the proper x-ray emission lines

The widths of the M_2 and M_3 atomic levels can be determined using either the $L_1M_{2,3}$ or the M_2N_4 and M_3N_5 dipole transitions. In the Z region studied in this work, the L_1 level widths [4] as well as the N_4 and N_5 ones [1] are known with a precision better than 16 %. The $N_{4,5}$ widths are, however, smaller than the L_1 ones and therefore the errors on the M_2 and M_3 level widths would be smaller if the latter were derived from the M_2N_4 and M_3N_5 transitions. Unfortunately, these M x-ray lines are about 10 times less intense than the $L_1M_{2,3}$ lines and, in addition, for the studied elements the M_3N_5 transitions are either hidden or affected by the presence of the strong L_3M_5 transitions which appear in fourth order of reflection at about the same Bragg angles as the M_3N_5 ones in first order. For these reasons, precise and reliable results cannot be obtained using these M x-ray lines. We have thus decided to measure the $L_1M_{2,3}$ transitions. A further advantage to use L_1 transitions resides in the fact that the latter are free of CK satellites, which makes their analysis more reliable. However, due to the competitive L_1L_2X and L_1L_3X CK transitions which transfer a significant part of the photo-induced 2s vacancies to the L_2 and L_3 subshells, L_1 x-ray lines are significantly weaker than L_2 and especially L_3 x-ray lines so that rather long acquisition times are required to get data with a good enough statistics. Furthermore, as the $L_1M_{2,3}$ transitions are close in energy to the strong L_2M_4 and L_3N_5 lines, not only the $L_1M_{2,3}$ transitions must be measured but all other close-lying x-ray lines. This point was found to be crucial for obtaining reliable fits of the $L_1M_{2,3}$ x-ray lines.

2.2. Experimental setup

The measurements were performed at the University of Fribourg by means of two different high-resolution bent crystal spectrometers. For the measurements of the L x-ray spectra of $_{81}$Tl, $_{83}$Bi and $_{95}$Am, a transmission DuMond-type crystal spectrometer, which has been designed to observe x rays above about 11 keV, was used. For $_{69}$Tm, $_{70}$Yb, $_{71}$Lu, $_{74}$W, $_{75}$Re and

$_{77}$Ir, the L x-ray lines were observed with a reflection von Hamos-type crystal spectrometer. Both instruments employed in this experiment have been previously described [9, 19, 20]. Therefore, only specific details concerning the set-up employed in the present experiment will be given below.

2.2.1 Measurements of the elements $81 \leq Z \leq 95$

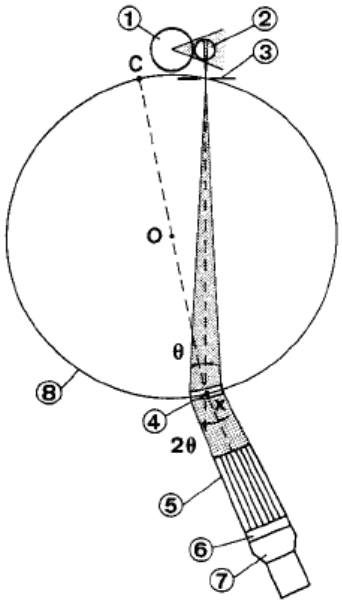

Fig. 2: (taken from Ref. [19]): Schematic view of the modified DuMond slit geometry (not to scale): (1) x-ray tube, (2) target, (3) ltor, (6) Phoswich scintillator, (7) phead slit, (4) bent crystal, (5) Soller-slit collimaotomultiplier, (8) Rowland circle. θ represents the Bragg angle, X the crystal axis, C the center of curvature of the crystal, and O the center of the focal circle.

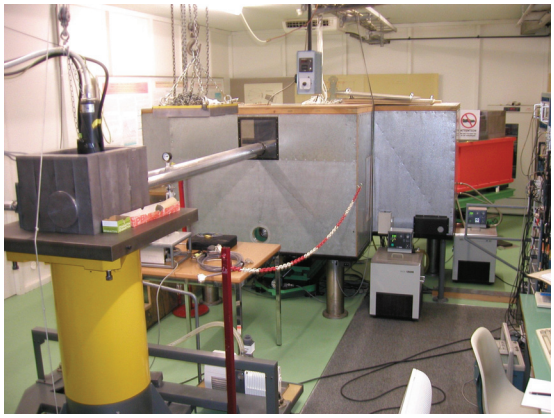

Fig. 3: Photograph of the transmission DuMond-type bent crystal spectrometer.

The transmission crystal spectrometer was operated in the so-called modified DuMond slit geometry. In this geometry a slit (0.1 mm wide) located on the focal circle at a fixed position served as the effective source of radiation (Fig. 2). The slit was made of two juxtaposed Pb plates, 25 mm high and 5 mm thick. The sample x-ray fluorescence was produced using the bremsstrahlung of a gold anode x-ray tube operated at 80 kV and 35 mA. The x-ray beam from the tube was perpendicular to the target-crystal direction. The targets were placed 1.75 cm behind the slit, at a distance of 45 mm from the tube anode, and tilted at a certain angle to the target-crystal direction. This angle was determined for each target in order to find the best compromise between the self absorption of the emitted x-rays in the target, which diminishes the fluorescence x-ray intensity, and the part of the target surface seen by the crystal through the slit, which increases the intensity of the measured x-rays.

For the diffraction of the fluorescence x-rays, the (110) planes of a 0.5 mm thick quartz crystal were used. The 10 cm x 10 cm crystal plate was bent cylindrically to a nominal radius of 315 cm. However, the best angular resolution was obtained for a radius of curvature of 317.5 cm. The effective crystal area contributing to the diffraction of the x rays was 12 cm^2. The diffracted x-rays were recorded by a 5-inches in diameter Phoswich scintillation detector consisting of a thin (0.25-inch) NaI(Tl) crystal followed by an optically coupled thick (2-inches) CsI(Tl) crystal, both crystals being mounted on the same photomultiplier. Due to their different rise times, the electric signals provided by the two scintillators can be distinguished. Good events are those for which only a photo-peak signal from the NaI scintillator is observed, events producing signals in both detectors being excluded by the electronics (anti-coincidence gate). This kind of anti-Compton detector permits to strongly reduce the background due to high-energy photons. The Soller-slit collimator placed in front of the detector serves mainly to reject photons that do not make an angle 2θ with respect to the direction of the incoming fluorescence x-ray beam, i.e. to photons that were not diffracted by the crystal. The collimator consists of 24 parallel slits, 660 mm long x 110 mm high x 2mm wide, the slits being defined by stainless steel plates with a trapezoidal horizontal cross section. To minimize the absorption of the fluorescence x rays in air, the target chamber was kept at low pressure (about 10^{-2} mbar), and evacuated tubes were mounted between the target chamber and the crystal and between the crystal and the collimator. The Bragg angles were measured by means of a Doppler-shift based optical laser interferometer with a precision of approximately $5 \cdot 10^{-3}$ arcsec. A photograph of the DuMond spectrometer is shown in Fig. 3.

All samples were measured in first order of reflection. For each target, the crystal to slit distance was adjusted to obtain the best resolution and the origin of the Bragg angle scale was determined by measuring the strong L_2M_4 transition on both sides of reflection. The Tl target was prepared by rolling high-purity (99.999%) granules. The average thickness of the so-obtained foil-like Tl sample was 112 mg/cm^2. The Bi target consisted of a 25 mm high x 5 mm wide metallic foil, with a purity of 99.97%. Bismuth being a brittle metal, the 5 μm thick Bi foil was mounted on a permanent polyester support. For the $_{95}$Am target, a ^{241}Am α-emitter source (~3-mm in diameter) mounted on a special backing was employed. The sample thickness was determined by comparing the widths of the 4.586 MeV α-particle line measured with this sample and a very thin ^{241}Am calibration source. A value of 1.35(25) μm was found.

For the energy calibration of the DuMond spectra, the spacing constant d_{110} of the quartz crystal was determined by assigning to the fitted peak centroid of the measured $K\alpha_1$ line of gold the reference energy taken from Kessler et al. [21]. The measurements were performed in fifth order on both sides of reflection, i.e., at Bragg angles close to those corresponding to the

$L_1M_{2,3}$ x rays of the studied elements. A value of 2.456596(8) Å was obtained for the lattice spacing constant d_{110}.

In the DuMond geometry the angular instrumental response[1] does not vary in first approximation with the Bragg angle. To get a precise value for the angular instrumental broadening, measurements of the $K\alpha_{1,2}$ x-ray spectrum of Gadolinium were performed in first, second, third, fourth and fifth orders of reflection. The angular spectra were fitted with Voigt functions. The intensities, energies, Lorentzian widths, Gaussian standard deviations and the parameters of the linear background were let free in the fitting procedure. The weighted average of the five Gaussian standard deviations obtained from the fits was found to be $\overline{\sigma}$ = 4.83 ± 0.28 arcsec, which corresponds for the L_1M_2 and L_1M_3 transitions to instrumental energy broadenings $\overline{\sigma}_E$ of 1.29(7) eV and 1.39(8) eV for $_{81}$Tl, 1.46(8) eV and 1.59(9) eV for $_{83}$Bi and 3.00(17) eV and 3.36(19) eV for $_{95}$Am. From the fits weighted average values of 26.1(2) eV and 26.4(3) eV were obtained for the Lorentzian widths of the $K\alpha_1$ and $K\alpha_2$ transitions of Gd, both results in very good agreement with the values of 26.1(2.1) eV and 26.3(2.1) eV reported by Campbell and Papp [1]. To further check the goodness of the instrumental resolution measurements, the $K\alpha_1$ line of Gold used for the determination of the constant d_{110} was re-fitted with a Voigt profile, letting free in the fitting procedure all parameters except the Gaussian instrumental broadening which was kept fixed at the value of 8.64 eV corresponding for this transition to the above mentioned angular resolution. From the fit, a value of 57.5(3) eV was obtained for the natural width of the Au $K\alpha_1$ transition, which is in perfect agreement with the result of 57.5(7) eV quoted in Ref. [22].

2.2.2 Measurements of the elements $69 \leq Z \leq 77$

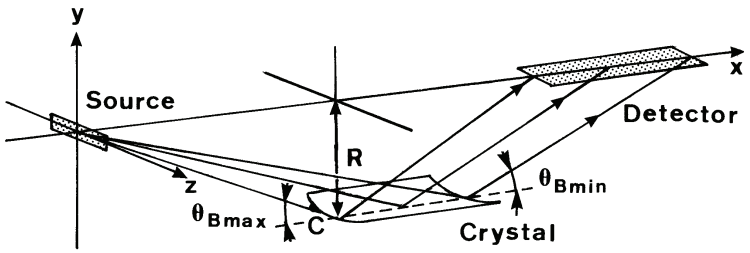

Fig. 4: (taken from Ref. [20]): Schematic drawing of the von Hamos spectrometer geometrical principle of operation. The crystal is curved around the x-axis. The figure is not to scale.

[1] Since nuclear states have mean lifetimes $\tau > 10^{-13}$ s, which correspond to natural level widths smaller than 0.007 eV, the instrumental broadening of a spectrometer can be directly determined from the observed FWHM of γ-ray lines. We have tried to make use of this property by measuring the 59 keV γ rays of the ^{241}Am source, but unfortunately the activity of the source (few mCi) was too weak for measurements with a crystal spectrometer.

Since the transmission-type spectrometer cannot be used for photon energies below about 11 keV, the L x-ray lines of $_{69}$Tm, $_{70}$Yb, $_{71}$Lu, $_{74}$W, $_{75}$Re and $_{77}$Ir were observed with a reflection-type crystal spectrometer, namely the von Hamos spectrometer of Fribourg. The principal elements of this instrument are an x-ray source defined by a rectangular slit, a cylindrically bent crystal and a position sensitive detector, located on the crystal axis of curvature (Fig. 4). The vertical rectangular slit consists of two juxtaposed Ta plates that are 0.3 mm thick and 20 mm high. The target, crystal and detector are all contained in a 180 x 62 x 24.5 cm^3 stainless steel vacuum chamber, which can be pumped down to about 10^{-6} mbar in 1-2 hours by a turbo-molecular pump.

Fig. 5: Photograph of the von Hamos spectrometer.

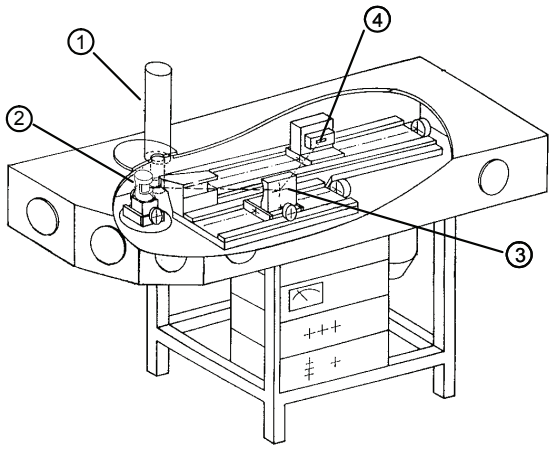

Fig. 6: Schematic drawing of the von Hamos spectrometer: (1) x-ray tube, (2) target barrel, (3) bent crystal, (4) CCD detector.

The fluorescence x-ray spectra were produced by irradiating the targets with the bremsstrahlung from a Cr anode x-ray tube operated typically at 60 kV and 35 mA. Each target was placed behind the slit at a distance of 2.9 cm, and tilted around a vertical axis in such a way that the normal to the sample surface made equal angles with the irradiation direction and the direction under which the sample x-ray emission was observed. A slit width of 0.2 mm was used for all samples. The emitted fluorescence x rays were reflected by a 5 cm wide x 10 cm high x 0.4 mm thick quartz $(2\bar{2}3)$ crystal (spacing constant 2d = 2.750 Å) bent to a radius of 25.4 cm. The diffracted x rays were detected with a 27.65 mm long and 6.9 mm high CCD (charge coupled device) camera, having a depletion depth of 50 μm and a pixel size of 27 x 27 μm^2. The CCD was thermoelectrically cooled down to –60°C. All targets were metallic foils, having a rectangular shape (20 mm high x 5mm wide), a specified purity ranging between 99.95 % and 99.99 %, and thicknesses varying from 8 μm to 125 μm. All measurements were carried out in first order of reflection. A photograph of the von Hamos spectrometer and a schematic drawing of the instrument are shown in Figs 5 and 6, respectively.

The energy calibration of the spectrometer was realized by measuring the $K\alpha_{1,2}$ transitions of Cu, Zn, Ge and As and assigning to the fitted centroid positions of these lines the corresponding transition energies reported by Deslattes et al. [23]. These $K\alpha_{1,2}$ transitions were also employed to determine the instrumental response of the von Hamos spectrometer. The four $K\alpha_{1,2}$ lines were fitted with Voigt profiles. The Lorentzian natural widths were kept fixed in the fits at the values quoted in Ref. [1] but the instrumental Gaussian broadenings were let free. For the latter, standard deviations σ of 0.96(5) eV at 8048 eV (Cu), 1.29(5) eV at 8638 eV (Zn), 1.71(6) eV at 9886 eV (Ge) and 1.83(8) eV at 10543 eV (As) were obtained from the fits. The uncertainties on the natural line widths quoted in [1] were taken into account in the determination of the errors Δσ. The instrumental broadenings corresponding to the L x-ray lines of interest were then computed by linear interpolations, using the two σ determined below and above the energies of the considered $L_1M_{2,3}$ transitions.

Since in the present experiment, the measurements were performed using two different spectrometers that are partly overlapping in the covered energy domains, we found useful to measure one transition with both instruments in order to probe the accuracy and reliability of our results. For this reason, the L_1M_3 transition of the lightest element measured with the DuMond spectrometer (i.e., $_{81}Tl$) was also measured with the von Hamos spectrometer. The same SiO_2 $(2\bar{2}3)$ crystal was employed but as the minimum Bragg angle that can be measured with the von Hamos spectrometer amounts to about 24 degrees which corresponds in 1st order to a maximum energy of about 11.1 keV, the $_{81}Tl$ L_1M_3 transition (E ≅ 12.4 keV) had to be

measured in 2nd order of reflection. For this line, the energy calibration and the instrumental response of the von Hamos spectrometer were determined by measuring in 2nd order the K$\alpha_{1,2}$ transitions of Se and gazeous Kr, using again for the reference energies and natural line widths the values quoted in Refs. [23] and [1]. Instrumental broadenings σ of 1.45(10) eV and 2.50(9) eV were found for Se and Kr, respectively. As shown later (see Tables 1 and 4), consistent results were obtained for the width and nearly consistent results for the energy of the L_1M_3 transition of Tl but the uncertainties of the results obtained with the von Hamos spectrometer are rather large due to the poor statistics of this measurement.

Chapter 3

Data analysis

As mentioned before, in order to obtain reliable results, not only the $L_1M_{2,3}$ transitions of interest have to be measured but also several neighbouring transitions so that for all samples rather broad energy domains should be scanned. However, because for measurements performed with the DuMond spectrometer the x-ray spectra are measured point by point, the times needed to measure such broad spectra would have been very long. In addition, as the absorption in the crystal is rather strong for such low photon energies as those corresponding to the $L_1M_{2,3}$ transitions, rather long acquisition times per point are needed to get data with a good enough statistics. For these reasons, the Tl and Bi measurements were performed in the following way: in a first stage, the energy domains comprised between 11764 eV and 12558 eV for Tl and between 12370 eV and 13307 eV for Bi were scanned with reasonably long acquisition times of 450 s per point, respectively 300 s per point. In a second stage, narrower energy domains corresponding to the L_1M_2 and L_1M_3 transitions only were measured in several successive scans. The different scans were then summed together off-line leading to total acquisition times of 1800 s and 1350 s per point for the L_1M_2 and L_1M_3 transitions of Tl, respectively 1100 s and 600 s per point for Bi. In the fits of the L_1M_2 and L_1M_3 lines obtained from the sum of the different scans, the linear background and the parameters of the neighbouring lines (intensities, centroid energies, widths) were kept fixed at the values obtained from the analysis of the broad spectra, values normalized beforehand for the acquisition time differences. For Am, only the L_1M_2 and L_1M_3 transitions of interest were measured, because in this case there is no strong line close in energy that may influence the widths of the $L_1M_{2,3}$ transitions. However, as the thickness of the employed Am target was very small, which resulted in poor intensities for the $L_1M_{2,3}$ transitions, the latter were also measured in several successive scans corresponding to total acquisition times per point of 8800 s and 7000 s for the L_1M_2 and L_1M_3 transitions, respectively.

For the measurements performed with the von Hamos spectrometer, energy domains of about 600 eV had to be measured to include the neighbouring lines. The von Hamos geometry permits at one position of the crystal and detector data acquisition over an energy bandwidth which is limited by the detector length [20]. For the same energy interval, measurements

performed with the von Hamos spectrometer are therefore usually shorter than those performed with the DuMond spectrometer. Depending on the central Bragg angle and the employed crystal, the covered energy interval varies between 30 eV and 300 eV. For the present project, the width of the energy interval was about 200 eV so that at least three different positions of the crystal and detector were needed. Actually, in order to have some overlap between the adjacent spectra, for each sample four partial spectra were measured. The intensities of the partial spectra were normalized off-line, using the intensity ratios between the overlapping energy regions, and then the four spectra were put together.

Except for Am for which only the $L_1M_{2,3}$ transitions were observed, the energy domains measured with the two spectrometers contained the transitions L_1M_2, L_3N_1, L_2M_4, L_1M_3, L_3N_4 and L_3N_5 and the M satellites of the $L_3N_{4,5}$ transitions. For Tl and Bi, the $L_3N_{6,7}$ transitions were also observed. As the energies of the diagram transitions depend on the target element, the above-mentioned sequence of transitions was not the same for each sample. All spectra were analysed by means of a last squares fitting program, employing Voigt profiles to fit the transitions. The Voigt profile results from the convolution of a Lorentzian representing the natural x-ray line shape with a Gaussian that corresponds to the response function of the spectrometer. The natural widths of the L x-ray lines were extracted by keeping fixed in the fitting procedure the Gaussian instrumental broadenings at their known values. The energies and the intensities of the transitions as well as a linear background were used as additional free fitting parameters. The x-ray lines measured with the von Hamos spectrometer were found to exhibit a small asymmetry on their low-energy flank. This asymmetry which originated from the crystal was investigated carefully and its variation with energy determined accurately. In the fits, the asymmetry was accounted for by adding a Voigtian on the low-energy side of all transitions.

The fits of the L x-ray spectra measured with the von Hamos and DuMond spectrometers are presented in Figs. 7 to 12 and 13 to 18, respectively. It is interesting to see that in each spectrum the L_1M_2 and L_1M_3 transitions occur always below and above the strong L_2M_4 transition, whereas the relative positions of the L_3 transitions change drastically with the atomic number of the sample. For instance, the L_3N_1 line lies above the L_2M_4 line for $_{69}$Tm (Fig. 7), between the L_1M_2 and L_2M_4 lines for $_{75}$Re (Fig. 12) and below the L_1M_2 line for $_{81}$Tl (Fig. 14).

The $L_3N_{4,5}$ lines of $_{73}$Ta, $_{75}$Re, $_{77}$Ir, $_{81}$Tl and $_{83}$Bi evince asymmetries on their high energy sides due to the presence of unresolved N spectator holes. Actually the energy shifts of satellites relative to the parent diagram lines increase with the principal quantum number of the transition electron and decrease with the principal quantum number of the spectator

vacancy. As a result, for L x-rays, the N x-ray satellites in most cases cannot be resolved from their parent diagram lines because their energy shifts are smaller than the natural line widths of the transitions and the N spectator holes lead only to broadenings or asymmetries of the diagram lines. In contrast to that, M satellites are generally well resolved. In the present project, the M satellites of the $L_3N_{4,5}$ transitions were observed for almost all studied elements, whereas those of the L_3N_1 transitions were not seen, their intensities being negligibly small. M satellites of the strong L_2M_4 transitions were also observed in the spectra of $_{73}$Ta, $_{74}$W, $_{75}$Re and $_{77}$Ir. Since L_1L_2M CK transitions are energetically forbidden for these elements, the weak M satellites are probably due to M-shell shake processes following the photo-induced production of the $2p_{1/2}$ core vacancy.

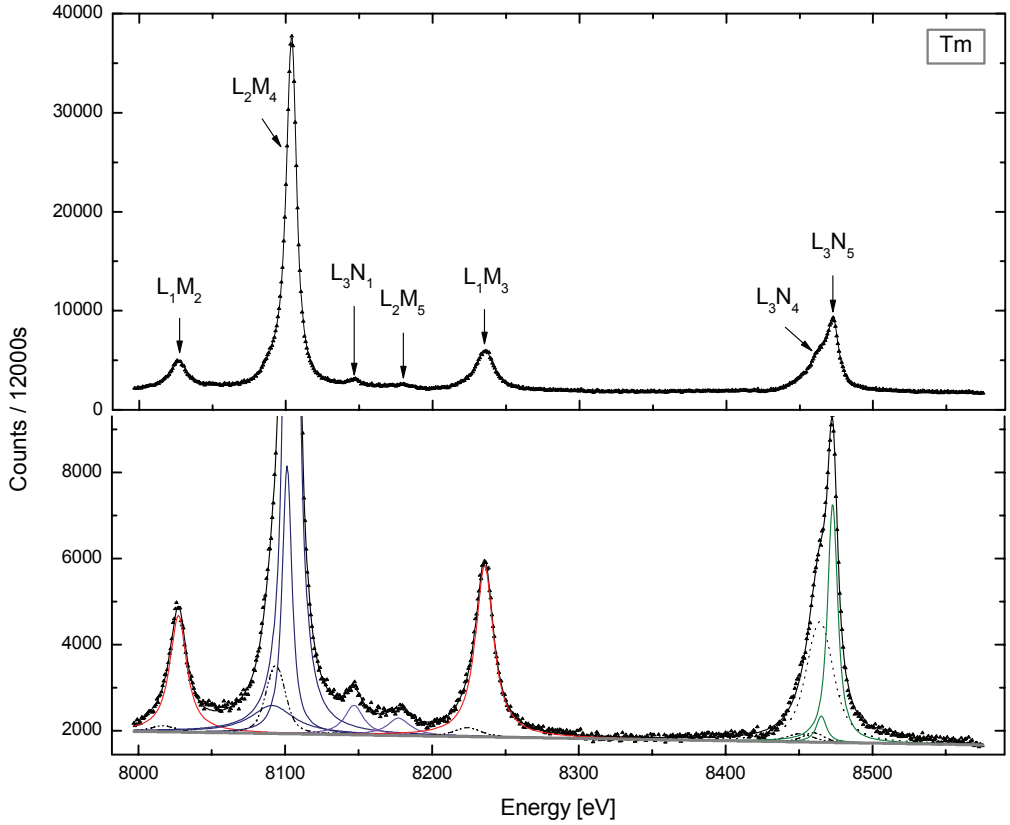

Fig. 7: High-resolution L x-ray spectrum of Tm measured with the von Hamos spectrometer. The top part of the Fig. presents the total fit of the spectrum, the bottom part shows details about the fitted components. The dotted lines represent the Voigtians used in the fit to account for the crystal asymmetry. The weak peak occurring at about 8512 eV corresponds to the M-satellite of the $L_3N_{4,5}$ transitions.

In $_{69}$Tm, $_{71}$Lu, $_{73}$Ta, $_{74}$W, $_{75}$Re and $_{77}$Ir, small asymmetries were observed on the low energy sides of the L_2M_4 transition. These asymmetries which result from the angular momentum coupling between the L_2 core vacancy and the partially filled outer shells was accounted for in the fits by adding one or two additional Voigt functions. For Yb ([Xe]$4f^{14}6s^2$), no asymmetry was observed since in the Yb crystal the two 6s electrons participate in the crystal bounding leaving the atom with a closed electronic shell configuration [24]. The same holds for Tl ([Hg]6p) and Bi ([Hg]$6p^3$) which are generally monovalent and trivalent, respectively.

For Ir (Fig. 13), the L_1M_2 and L_3N_1 transitions are strongly overlapping. Any attempt to let free in the fitting procedure the energy and linewidth of the L_3N_1 line was found to be unsuccessful so that these two parameters were kept fixed at the values taken respectively from Refs. [23] and [1].

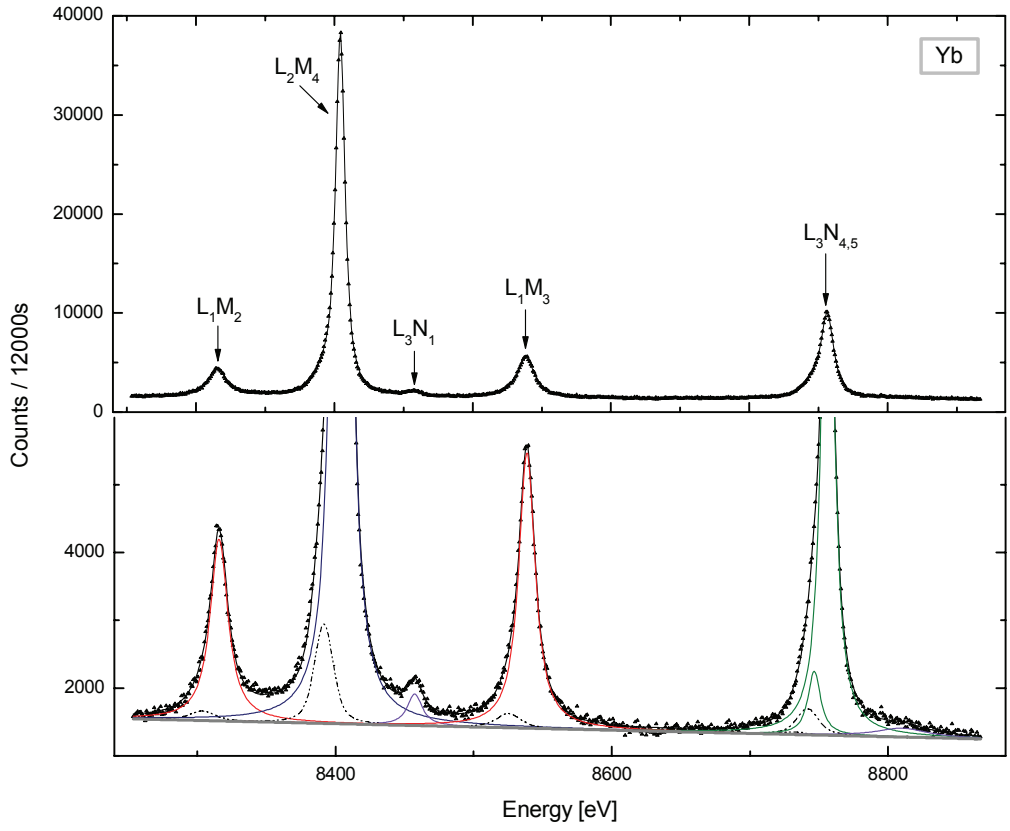

Fig. 8: Same as Fig. 7 but for Yb. The line observed at about 8810 eV corresponds to the M-satellite of the $L_3N_{4,5}$ transitions.

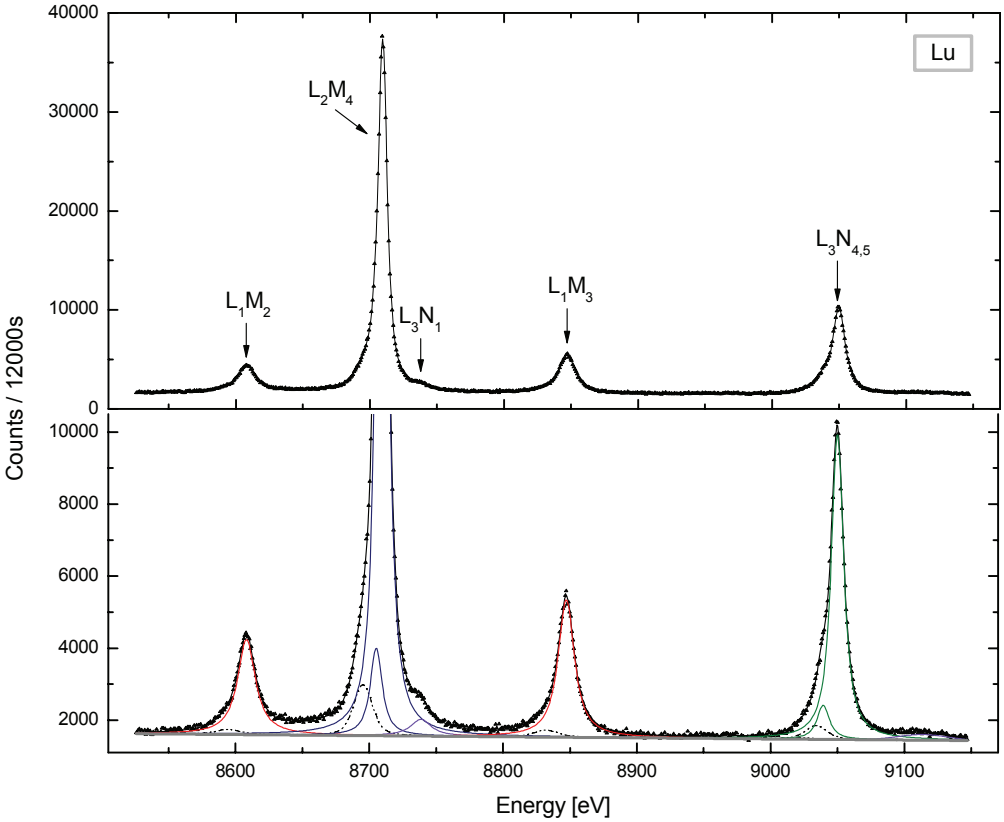

Fig. 9: Same as Fig. 7 but for Lu. The line observed at about 9114 eV corresponds to the M-satellite of the $L_3N_{4,5}$ transitions.

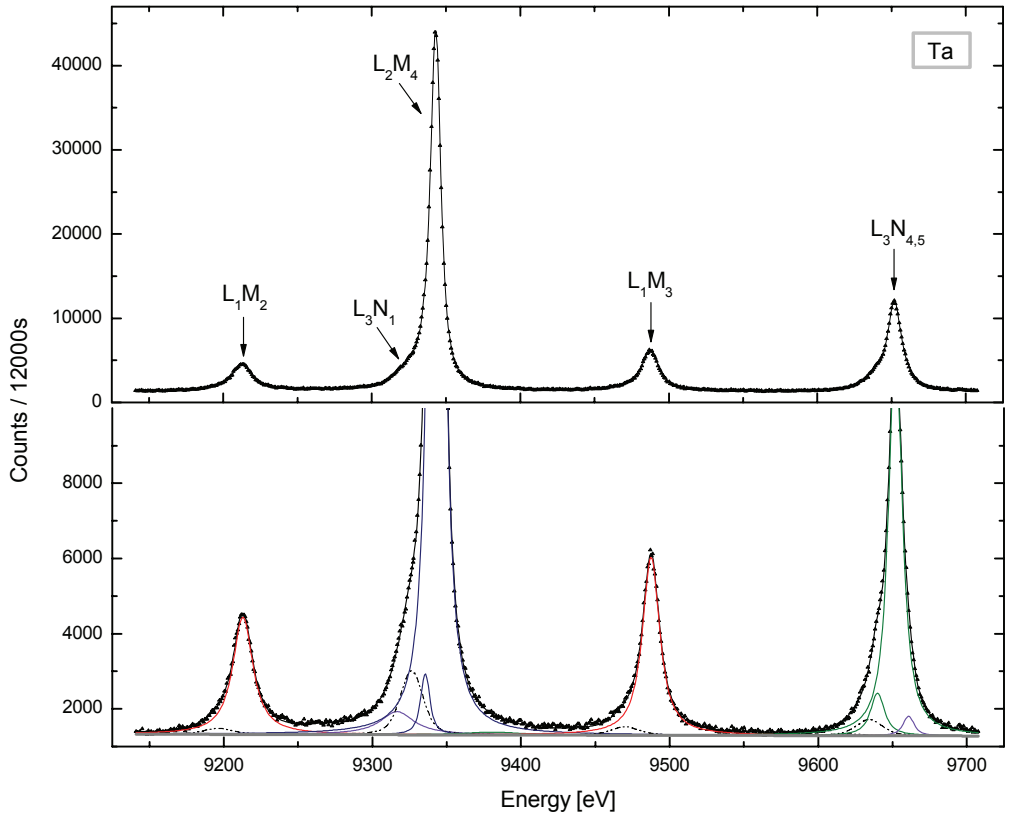

Fig. 10: Same as Fig. 7 but for Ta. The lines observed at about 9381 eV and 9661 eV correspond respectively to the M-satellite of the L_2M_4 transition and the N satellites of the $L_3N_{4,5}$ transitions.

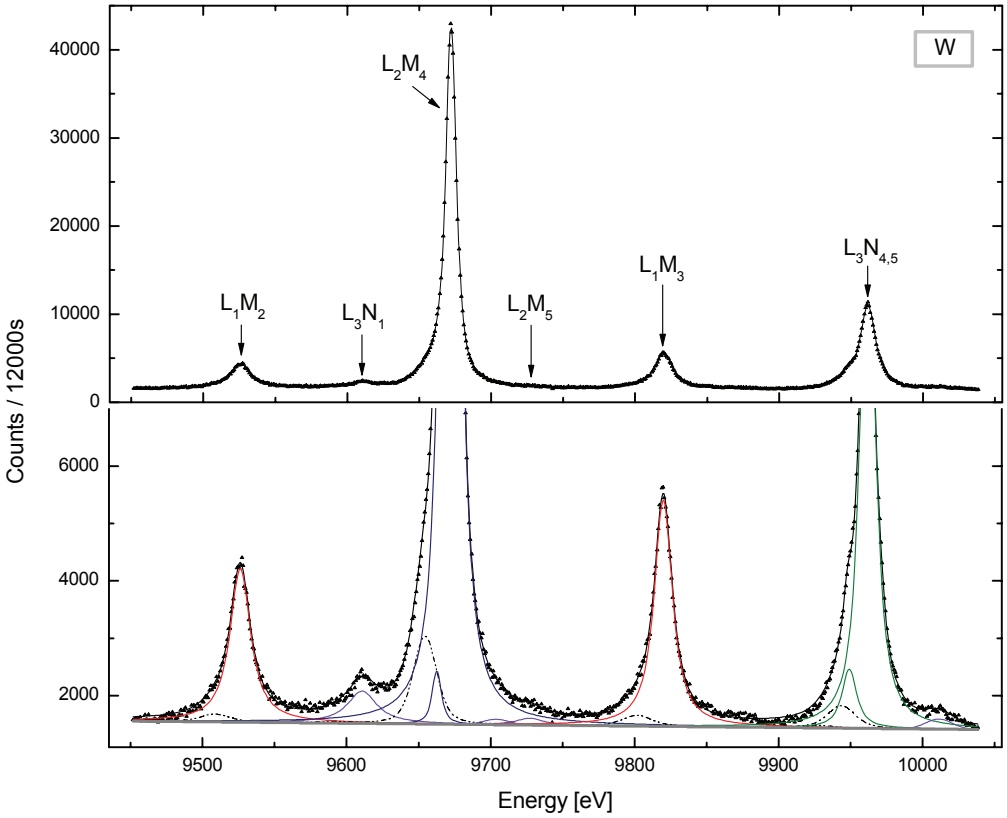

Fig. 11: Same as Fig. 7 but for W. The lines observed at about 9704 eV and 10011 eV correspond to the M-satellites of the L_2M_4 and $L_3N_{4,5}$ transitions, respectively.

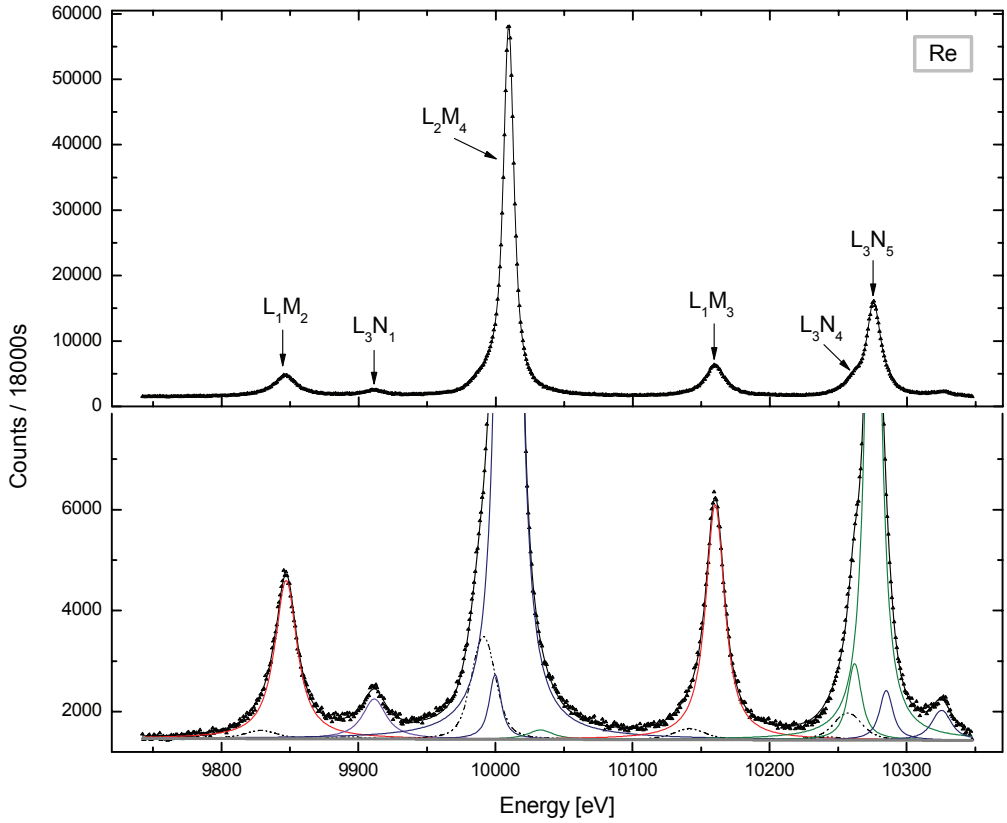

Fig. 12: Same as Fig. 7 but for Re. The line observed at 10033 eV corresponds to the M-satellite of the L_2M_4 transition and those observed at 10285 eV and 10326 eV to the M and N satellites, respectively, of the $L_3N_{4,5}$ transitions.

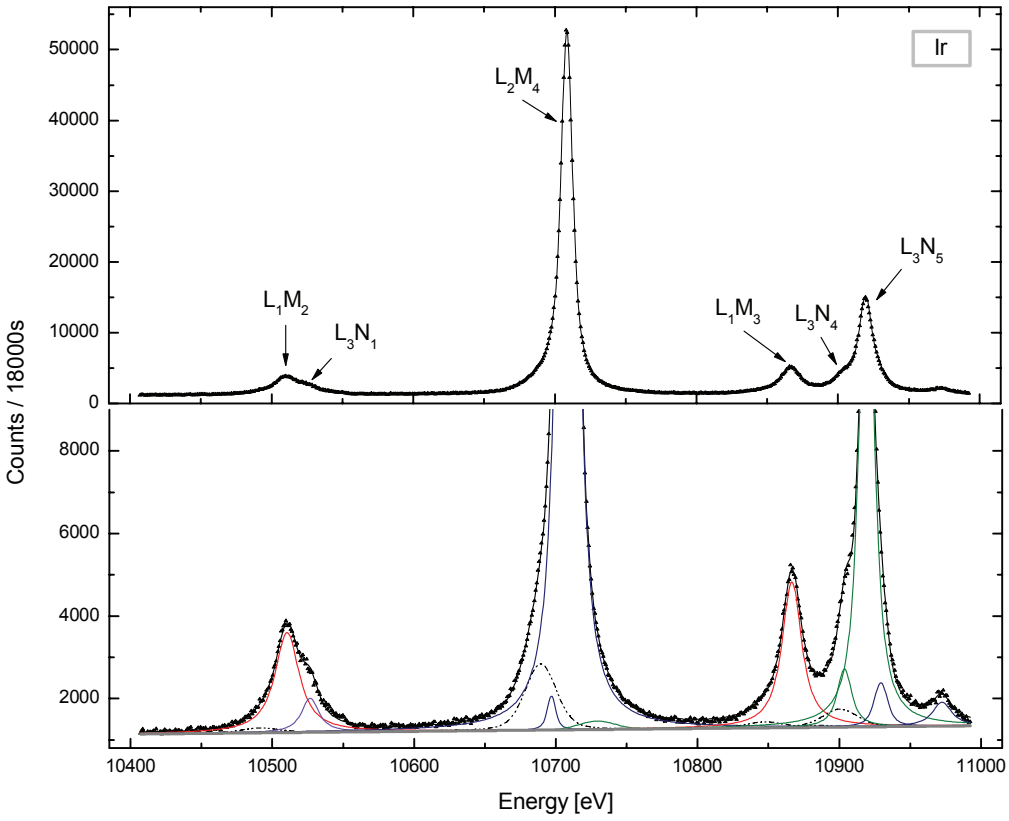

Fig. 13: Same as Fig. 7 but for Ir. The line observed at 10729 eV corresponds to the M-satellite of the L_2M_4 transition and those observed at 10929 eV and 10973 eV to the M and N satellites, respectively, of the $L_3N_{4,5}$ transitions.

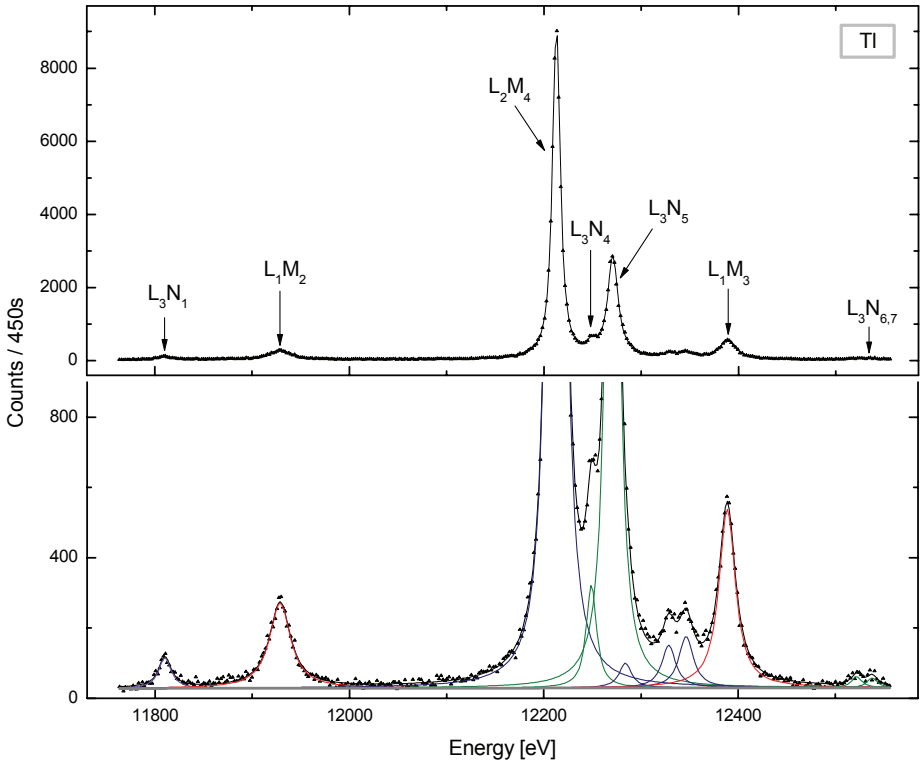

Fig. 14: High-resolution L x-ray spectrum of Tl measured with the Dumond spectrometer. The lines observed at 12329 eV and 12347 eV correspond to the M-satellites of the $L_3N_{4,5}$ transitions.

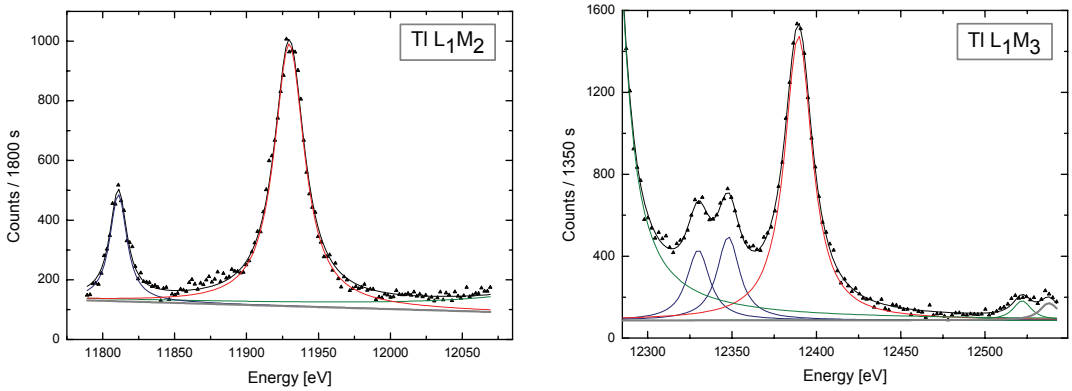

Fig. 15: L_1M_2 and L_1M_3 x-ray lines of Tl measured with longer acquisition times than the one used for the whole L spectrum represented in Fig. 14. In the analysis of the above partial spectra, only the parameters of the L_1M_2 and L_1M_3 transitions were let free, other fitting parameters (background, energies, widths and intensities of neighbouring lines) being kept fixed at the values obtained from the fit of the whole spectrum shown in Fig. 14 (for details, see text).

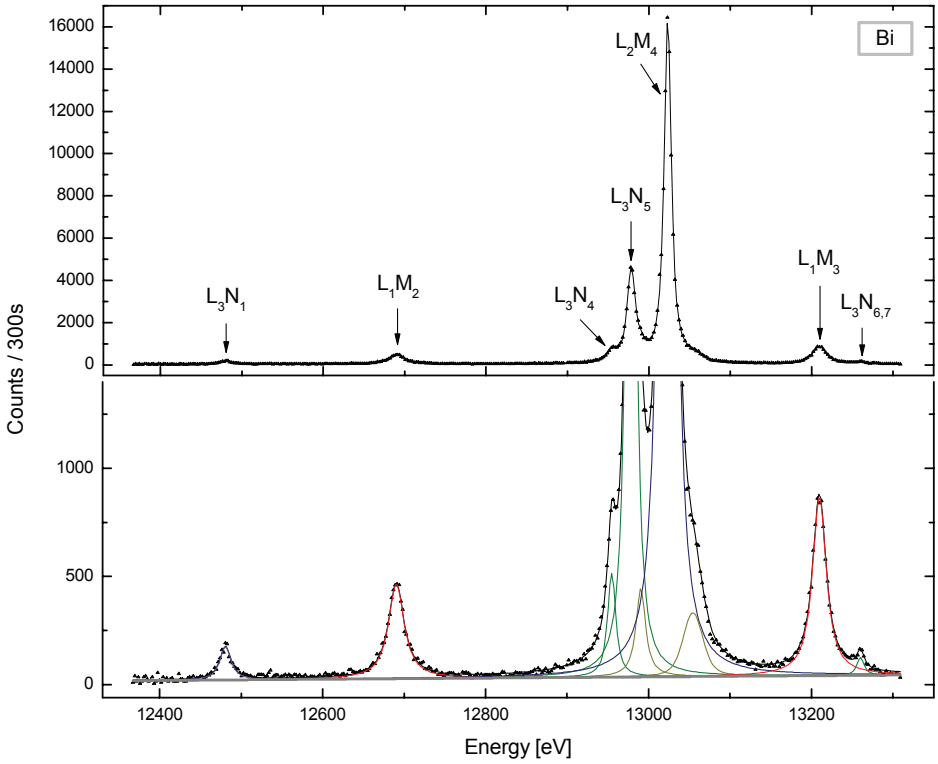

Fig. 16: Same as Fig. 14 but for Bi. The lines observed at 12990 eV and 13055 eV correspond respectively to the N and M satellites of the $L_3N_{4,5}$ transitions.

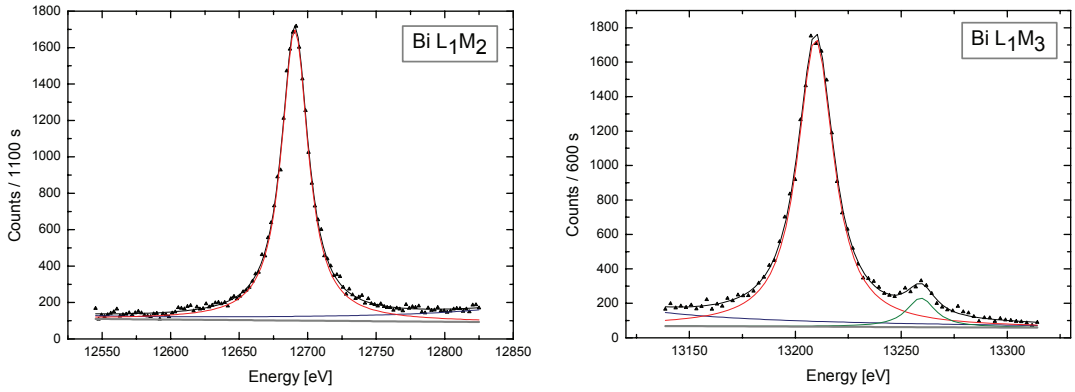

Fig. 17: Same as Fig. 15 but for Bi. The line observed at about 13260 eV corresponds to the $L_3N_{6,7}$ transitions.

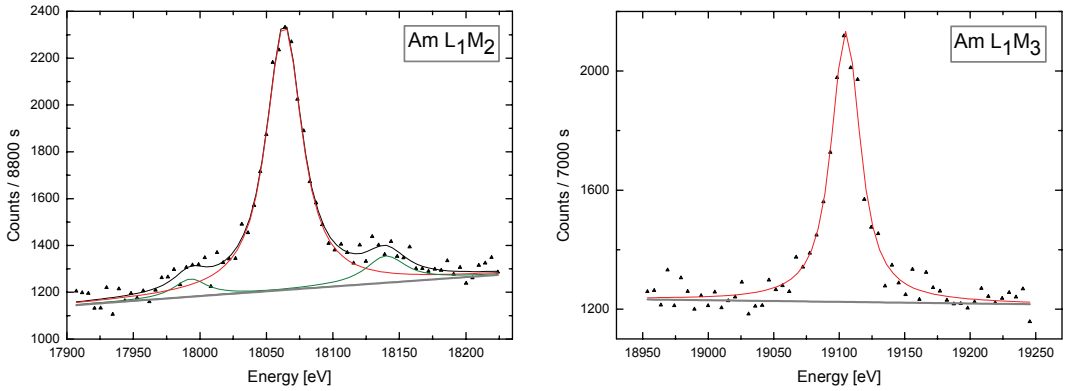

Fig. 18: Same as Fig. 15 but for $^{241}_{95}\mathrm{Am}$. The line observed at about 18140 eV corresponds to the L_3O_1 transition and the one at about 17990 eV to the L_1M_3 transition of $^{237}_{93}\mathrm{Np}$ which results from the α-decay of $^{241}_{95}\mathrm{Am}$. For this sample, due to the poor intensity of the fluorescence emission, we have renounced to measure the whole L x-ray spectrum.

Chapter 4

Results and discussion

4.1 $L_1M_{2,3}$ transition energies

The energies of the measured $L_1M_{2,3}$ transitions are given in Table 1 together with the experimental and theoretical values reported recently by Deslattes et al. [23].

	L_1M_2 transition energy [eV]			L_1M_3 transition energy [eV]		
	Experiment		Theory	Experiment		Theory
Element	Present	Ref. [23]	Ref. [23]	Present	Ref. [23]	Ref. [23]
$_{69}$Tm	8025.10(10/13)[1]	8025.8(1.5)	8026.1(2.6)	8233.75(11/13)[1]	8230.9(1.6)	8234.3(2.6)
$_{70}$Yb	8313.36(42/43)[1]	8313.26(25)	8313.6(2.7)	8536.17(42/43)[1]	8536.79(43)	8536.8(2.8)
$_{71}$Lu	8607.74(27/28)[1]	8606.54(44)	8606.3(2.7)	8846.73(28/29)[1]	8847.03(47)	8845.6(2.7)
$_{73}$Ta	9212.82(30/31)[1]	9212.47(30)	9212.6(2.7)	9487.50(23/23)[1]	9487.62(32)	9487.1(2.8)
$_{74}$W	9526.20(21/23)[1]	9525.23(54)	9526.0(2.8)	9819.95(12/13)[1]	9818.91(46)	9819.5(2.9)
$_{75}$Re	9847.05(11/14)[1]	9846.35(58)	9846.8(2.8)	10160.29(19/20)[1]	10159.90(62)	10160.4(2.9)
$_{77}$Ir	10510.42(3/11)[1]	10510.72(40)	10510.4(2.9)	10866.59(20/21)[1]	10866.54(42)	10867.5(3.0)
$_{81}$Tl	11929.68(4/14)[2]	11930.78(51)	11931.0(3.0)	12389.40(4/9)[2] 12390.33(25/70)[1]	12390.55(55)	12390.6(3.2)
$_{83}$Bi	12690.58(4/8)[2]	12691.40(77)	12690.9(3.1)	13209.57(4/9)[2]	13209.99(62)	13210.4(3.2)
$^{241}_{95}$Am	18063.35(6/34)[2]	18062.96(78)	18065.7(3.5)	19104.98(6/40)[2]	19106.24(87)	19107.4(3.7)

[1]von Hamos spectrometer [2]DuMond spectrometer

Table 1: Energies of the L_1M_2 and L_1M_3 transitions. Present results are compared to theoretical and experimental values reported by Deslattes et al. [23]. The notation 8025.10(10/13) eV means 8025.10 ± 0.13 eV with an included contribution of ± 0.10 eV to the total error from the uncertainty related to the energy calibration of the spectrometer.

As shown, present results are all consistent within the combined errors with the theoretical transition energies quoted in [23]. The uncertainties given for the latter are rather large (about 3 eV) so that the observed overall agreement is not really surprising. Nevertheless, we would like to point out that the average value of the differences between our results and these theoretical predictions is only 0.8 eV, i.e., about 4 times less than the theoretical errors. In

contrast to that, about 35% of the experimental values listed in [23] are not consistent with our results, the biggest deviation being observed for the L_1M_3 transition of Tm (difference of 2.8 eV significantly bigger than the quoted error of 1.6 eV). It should be noted, however, that for the considered elements all experimental values reported in [23] were taken from the prior tabulation of Bearden [25]. Although these old Bearden's data were re-adjusted in [23] to the new x-ray wavelength scale, they have to be regarded cautiously because several modern x-ray metrology measurements have shown that Bearden's values deviate sometimes from the new results by several standard deviations, especially for weak x-ray lines. For instance, for the above-mentioned L_1M_3 transition of Tm, the Bearden's value looks dubious since it is 3.4 eV smaller than the corresponding theoretical prediction, whereas for the L_1M_2 transition of the same element the difference with theory is only 0.3 eV.

For the measurements performed with the von Hamos spectrometer, the errors of present results originate mainly from the energy calibration procedure (see Table 1). In general, the energy uncertainty of transitions observed with the von Hamos spectrometer increases with the difference between the Bragg angles corresponding to the transition of interest and the transition employed as reference for the energy calibration. For instance, for Ir which was calibrated with the $K\alpha_1$ transition of As (E = 10543.2674 ± 0.0081 eV [23]), the energy calibration error of the L_1M_2 transition is only 0.03 eV because the Bragg angles corresponding to the two transitions differ by less than 0.09 deg., whereas for the L_1M_3 transition, due to the bigger difference in the Bragg angles (0.8 deg.), the calibration error is approximately seven times bigger (0.20 eV). A further contribution to the relative big energy calibration errors affecting the measurements performed with the von Hamos spectrometer originates from the uncertainties on the energies of the transitions used as references. For the L_1M_3 transition of W which was calibrated with the $K\alpha_1$ transition of Ge, the calibration error is 0.11 eV although the two Bragg angles are similar (difference smaller than 0.2 deg.) because the energy of the $K\alpha_1$ transition of Ge is only known with a poor precision (E = 9886.52 ± 0.11 eV [23]).

For the measurements performed with the DuMond spectrometer, quoted errors arise mainly from the fitting procedure, the uncertainty related to the energy calibration being small (0.04 to 0.06 eV). For Am, despite the long acquisition times used to measure the two transitions (about 170 h for the L_1M_2 transition and about 130 h for the L_1M_3), the errors given by the fits were rather large (0.33 eV and 0.4 eV, respectively). The poor statistics of these measurements resulted mainly from the tiny dimensions of the employed sample. The effective surface of the latter was indeed only about 0.5 mm^2 (75 mm^2 for other samples) and its thickness 1.35 μm.

The 3p spin-orbit splitting energies were derived from the energy differences between the L_1M_3 and L_1M_2 transitions. Results are presented in Table 2 where they are compared to theoretical predictions obtained from many body perturbation theory calculations (MBPT) [23] and relativistic Dirac-Fock calculations (DF) [26]. As shown, except for Ir, our results agree very well with predictions from MBPT calculations since an average deviation of only 0.3 eV is observed. For Ir the deviation is somewhat bigger (about 0.9 eV). On the contrary, DF calculations seem to overestimate systematically our values by approximately 1.5%.

The energy difference between the M_3 and M_2 levels can also be derived from the separation energy between the $K\beta_1$ and $K\beta_3$ x-ray lines. For tungsten, Kessler et al. [22] have reported for these transitions energies of 67245.45 eV and 66952.40 eV. The precision of the measurements was 16 ppm. From these values an energy difference of 293.05 ± 1.52 eV is found, which is also in good agreement with the result of 293.75 ± 0.26 eV obtained from our measurements.

Element	Present	MBPT [23]	DF [26]
$_{69}$Tm	208.65(18)	208.2	211.2
$_{70}$Yb	222.81(61)	223.2	226.6
$_{71}$Lu	238.99(40)	239.3	242.9
$_{73}$Ta	274.68(39)	274.5	278.4
$_{74}$W	293.75(26)	293.5	297.7
$_{75}$Re	313.24(24)	313.6	318.0
$_{77}$Ir	356.17(24)	357.1	362.2
$_{81}$Tl	459.72(17)	459.6	466.0
$_{83}$Bi	518.99(26)	519.5	526.6
$^{241}_{95}$Am	1041.63(52)	1041.7	1055.7

Table 2: Energy difference between the $3p_{3/2}$ and $3p_{1/2}$ atomic levels.

As shown in Fig. 18, the L_1M_3 transition of Np was observed in the L_1M_2 spectrum of Am because, due to the α-decay $^{241}_{95}\mathrm{Am} \rightarrow {}^{237}_{93}\mathrm{Np}$, the Am sample contained a significant amount of Np. An energy of 17993.9 eV was found for this transition. However, as the Np L_1M_3 line is still weaker than the L_1M_2 line of Am and partly overlapping with the latter, the error of ± 4.7 eV given by the fit was so large that we have renounced to include this transition in Table 1.

Finally, as mentioned in Chap. 2 the L_1M_3 transition of Tl was measured with both the DuMond and von Hamos spectrometers. As shown in Table 1, the obtained energies are nearly consistent, a difference of 0.93 eV being observed which is 30% bigger than the error of 0.70 eV given for the von Hamos measurement. Note that this error is much bigger than the one corresponding to the measurement performed with the DuMond spectrometer because of the poor statistics of the von Hamos measurement. The latter had indeed to be performed in 2nd order of reflection, which resulted in a significant loss of the crystal reflectivity. In addition, for this relatively high energy (12.4 keV), the CCD efficiency was smaller than for other lighter elements.

4.2 $L_1M_{2,3}$ transition widths

The L_1M_2 and L_1M_3 line widths obtained in the present work are presented in Table 3 and Table 4, respectively. For comparison, the corresponding recommended values of Campbell and Papp [1] and theoretical predictions by Perkins [11] are listed, too. These data and other earlier experimental values are also represented graphically in Figs. 19 and 20. As shown, except for Bi, present L_1M_2 transition widths are systematically bigger (10%-20%) than the values recommended by Campbell and Papp. For the L_1M_3 transition, the same trend is observed but only for the elements $Z \leq 75$.

	Experimental		Theoretical
Z	Present	Campbell [1]	Perkins [11]
$_{69}$Tm	13.28(5/28)[1]	11.8(1.7)	16.10
$_{70}$Yb	15.00(5/25)[1]	12.3(1.8)	18.36
$_{71}$Lu	15.44(5/23)[1]	12.7(1.8)	19.29
$_{73}$Ta	15.49(6/20)[1]	13.8(1.9)	21.49
$_{74}$W	16.23(7/29)[1]	14.4(1.9)	23.16
$_{75}$Re	18.43(7/26)[1]	15.1(2.0)	24.47
$_{77}$Ir	19.61(7/33)[1]	16.8(2.5)	25.40
$_{81}$Tl	24.93(4/48)[2]	21.2(2.8)	27.03
$_{83}$Bi	23.01(6/23)[2]	23.0(2.9)	27.54
$^{241}_{95}$Am	30.47(11/1.16)[2]	-	31.70

[1]von Hamos spectrometer [2]DuMond spectrometer

Table 3: Natural line widths in eV of the L_1M_2 x-ray transition. Our experimental results are compared to the recommended values of Campbell and Papp [1] and to theoretical predictions of Perkins [11]. The notation 13.28(5/28) eV means 13.28 ± 0.28 eV with an included contribution of ± 0.05 eV to the total error from the instrumental broadening uncertainty.

	Experimental		Theoretical
Z	Present	Campbell [1]	Perkins [11]
$_{69}$Tm	14.34(5/19)[1]	12.0(1.7)	16.22
$_{70}$Yb	13.66(5/16)[1]	11.9(1.7)	18.54
$_{71}$Lu	13.81(6/15)[1]	11.4(1.7)	19.55
$_{73}$Ta	12.94(8/14)[1]	11.7(1.7)	20.41
$_{74}$W	14.06(8/19)[1]	12.7(1.8)	27.74
$_{75}$Re	15.48(9/19)[1]	13.6(1.9)	23.07
$_{77}$Ir	15.25(12/24)[1]	15.9(2.4)	24.12
$_{81}$Tl	19.10(6/26)[2] 19.40(12/2.15)[1]	19.8(2.6)	24.23
$_{83}$Bi	19.77(8/29)[2]	20.9(2.6)	24.86
$^{241}_{95}$Am	24.59(13/1.37)[2]	-	27.72

[1]von Hamos spectrometer [2]DuMond spectrometer

Table 4: Same as Table 1 but for the L_1M_3 x-ray transition.

From the two tables, it can be seen that for both spectrometers total errors arise mainly from the statistical errors given by the fits, the contribution of the errors on the instrumental broadening being negligibly small in most cases. The widths of the L_1M_3 transitions of Tl measured with the DuMond and von Hamos spectrometers are in good agreement since they differ only by 0.3 eV, the error on the result obtained with the von Hamos spectrometer being seven times bigger (2.1 eV). As for the energy, this important error of 2.1 eV is due to the poor statistics of the measurement which was performed in second order of reflection.

Only three not too old data are available for comparison with the widths obtained in the present work. The first one concerns Ir for which a width of 15.1 ± 0.5 eV, in a fairly good agreement with our result of 15.25 ± 0.25 eV, is reported in [8] for the L_1M_3 transition. The two other available data concern the L_1M_2 and L_1M_3 widths of W for which values of 15.0 ± 0.5 eV and 12.7 ± 0.5 eV are quoted in [7]. The latter are both smaller than ours by 10% and 8%, respectively. A possible explanation for the slight discrepancy is that the instrumental broadening in [7] was somewhat overestimated. To extend the comparison to other elements, linear interpolations of the transition widths obtained for Ir and Tl, respectively Bi and Am, were done. From the interpolations values of 23.6(4) eV and 18.1(3) eV, 27.4(8) eV and 22.6(9) eV, and 28.6(9) eV and 23.4(1.1) eV were obtained for the widths of the L_1M_2 and L_1M_3 transitions of Hg, Th and U. Keeping in mind that above interpolations represent very crude approximations for the real transition widths, the obtained values can be considered to

be again in quite satisfactory agreement with the widths of 22.6(3) eV and 18.6(3) eV, 27.6(7) eV and 23.6(3) eV, and 31.1(3) and 23.7(4) eV reported for Hg [13], Th [10] and U [9].

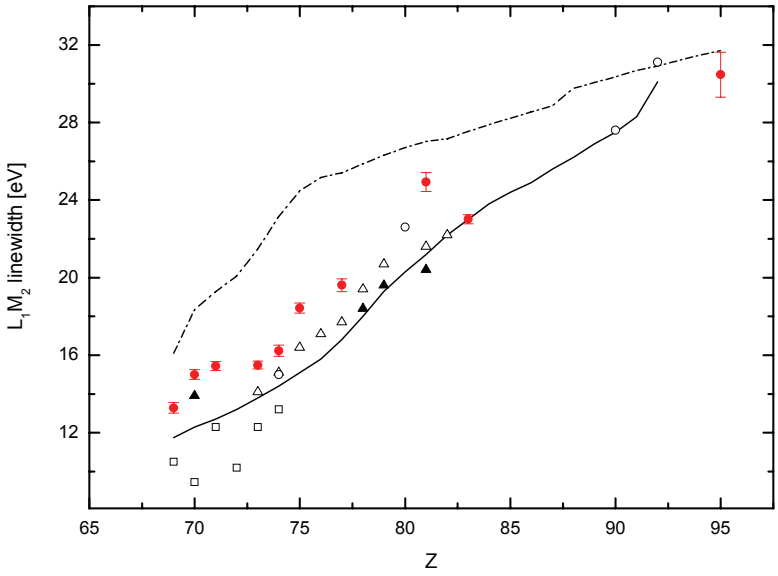

Fig. 19: Line width of the L_1M_2 transition versus atomic number. The symbol ● corresponds to the results obtained in the present work, the solid line represents the recommended values of Campbell and Papp [1] and the dashed dotted line the calculations of Perkins [11]. Other plotted experimental data were taken from: □ Ref. [2], Δ Ref. [3], ▲ Ref. [27], ○ Refs. [4, 7, 9, 10, 13].

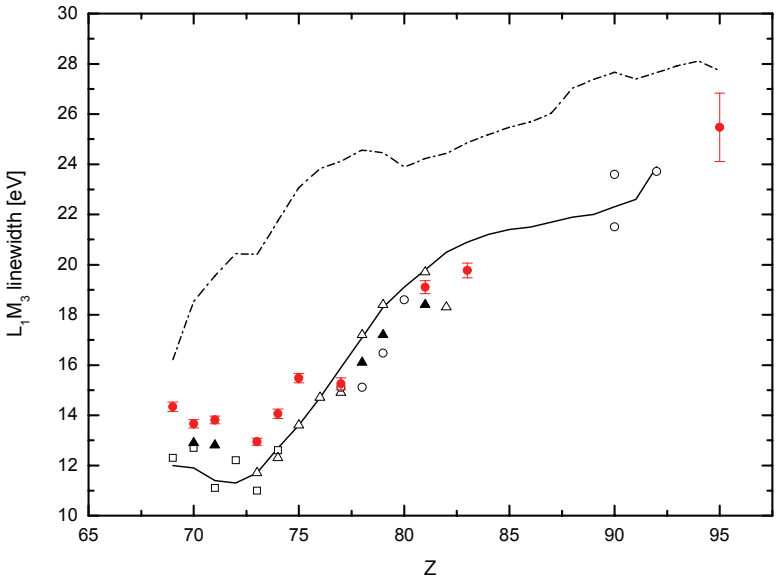

Fig. 20: Line width of the L_1M_3 transition versus atomic number. The same symbols as in Fig. 19 are used except for the experimental data represented by the symbol (○) which were taken from Refs. [7, 9, 10, 13, 6, 8].

4.3. $M_{2,3}$ atomic level widths

4.3.1 Theoretical $M_{2,3}$ atomic level widths

The energy width of an atomic level is related to the lifetime of the vacancy created in that level by the Heisenberg's uncertainty principle (see Sect. 1.2). The primary vacancy can be filled as a result of a radiative, Auger or Coster-Kronig (CK) transition. For M levels, the fluorescence yields are small (less than 5.5% for the Z region studied in this work [28, 29]). As a consequence, the total M level widths are almost entirely due to non-radiative decay processes. According to Coster and Kronig [30], the probability of an Auger transition is proportional to the overlap between the wave functions of the initial and final states of both the transition electron and the ejected electron. Therefore, when they are energetically allowed, CK and especially super CK transitions (i.e. CK transitions involving three subshells of the same major shell) are highly probable and the level widths are governed mainly by these transitions. For the Z region concerned by this study, super CK transitions are energetically forbidden but there are several allowed CK transitions and the $M_{2,3}$ level widths are mostly due to them. In $_{74}W$ for example, the calculations of Perkins [11] show that 77% of the M_2 vacancies and 70% of the M_3 vacancies are filled through CK transitions. Since the differences between the electron binding energies in the subshells vary with the atomic number Z, certain CK transitions do exist only for elements belonging to specific Z regions of the periodic table [18]. The first element for which a given CK transition becomes energetically allowed or forbidden is called the onset or cut-off element for the considered CK transition.

Auger and Coster-Kronig transition probabilities for the $M_{2,3}$ shells of elements with atomic numbers $22 \leq Z \leq 90$ were calculated by McGuire using a non relativistic Herman and Skillman potential and a semi-empirical estimation for the transition energies [31]. Chen et al. [28] reported relativistic calculations of non-radiative rates for the $M_{1,2,3}$ subshells of 10 elements with $67 \leq Z \leq 95$ based on a DHS potential. Using the results of Scofield's DHS calculations for the radiative rates [32], they computed also the total $M_{1,2,3}$ level widths. Their results were found to overestimate the experimental data but showed a significant improvement with respect to the non-relativistic calculations of McGuire. A much better agreement with experimental data was obtained by Ohno et al. [33] from MBPT calculations. However, these calculations were performed only for elements $36 \leq Z \leq 54$. An extension of both the DHS relativistic calculations of Chen [28] for the non-radiative rates and those of Scofield [32] for the radiative rates to all elements in the range $1 \leq Z \leq 100$ was reported later by Perkins et al. [11].

4.3.2. Experimental $M_{2,3}$ atomic level widths

In the present work, the natural widths of the M_2 and M_3 subshells were determined from the differences between the measured widths of the $L_1M_{2,3}$ transitions and the experimental widths of the L_1 subshell reported by Raboud et al. in [4]. Raboud's results were preferred to Campbell's recommended values because the latter have errors 3-5 times bigger than the ones of Raboud. For the elements that were not measured in [4], linear interpolations between the two next neighbouring elements with Z below and above the atomic number of the element of interest were employed. For Tm, the L_1 width was taken from the curve given by the authors of [4] for the lanthanide region (see Fig. 21). In this region, a broadening of the 2s level was indeed observed. The latter was explained by a splitting effect [34] of the L_1 subshell due to an exchange interaction between the spin of the 2s level and the total spin of the unfilled 4f level. For Am, the L_1 width was determined by a linear extrapolation of the values reported in [4] for Bi and in [10] for Th and U.

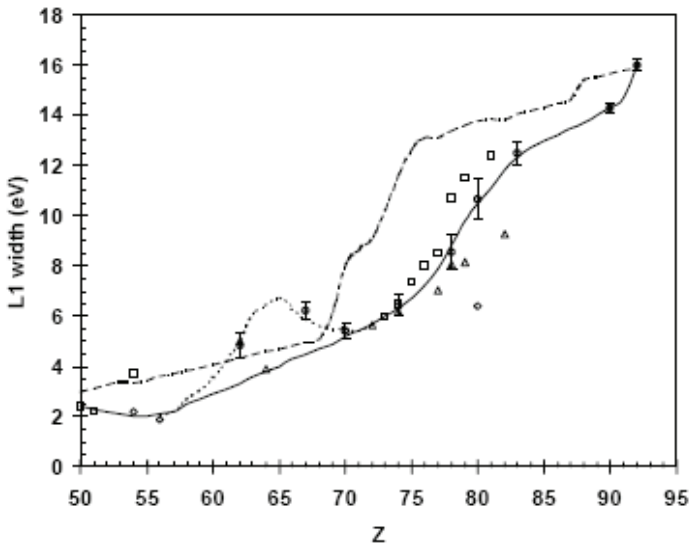

Fig. 21: (taken from Ref. [4]): L_1 level width versus atomic number Z. The solid line represents the recommended values of Campbell and Papp [1], the dashed line results of independent-particle model calculations of Perkins et al. [11], and the dotted line predictions of the splitting model developed in Ref. [4] for the rare-earth elements. Experimental data from different sources are also presented, using the following symbols: (◊) x-ray absorption edge results from Refs. [35, 36], (Δ) results derived from Coster-Kronig transition probabilities from Refs. [37, 38, 39], (□) XES results from Refs. [3, 40], (●) XES results for thorium and uranium from Refs. [9, 10], (○) XES results from Ref. [4].

4.3.2.1 M_3 level widths

The M_3 level widths obtained in this work are presented in Table 5 together with the recommended values of Campbell and Papp [1] and the theoretical predictions of Perkins [11]. Values of the L_1 widths from [4] and [1] are also listed. A graphical comparison between present results and other available experimental and theoretical data is given in Fig. 22.

Element	L_1 width [4] [eV]	L_1 width [1] [eV]	M_3 width [eV] Present	M_3 width [eV] Campbell [1]	M_3 width [eV] Perkins [11]
$_{69}$Tm	5.45(32)[1]	4.9(1.5)	8.89(37)	7.1(9)	10.06
$_{70}$Yb	5.40(30)	5.2(1.5)	8.26(34)	6.7(9)	10.50
$_{71}$Lu	5.65(33)[2]	5.4(1.5)	8.16(36)	6.0(8)	10.91
$_{73}$Ta	6.16(40)[2]	6.0(1.5)	6.78(42)	5.7(8)	10.19
$_{74}$W	6.41(43)	6.3(1.5)	7.65(47)	6.4(1.0)	10.12
$_{75}$Re	6.94(50)[2]	6.7(1.5)	8.54(53)	6.9(1.1)	10.40
$_{77}$Ir	8.02(63)[2]	7.9(2.0)	7.23(67)	8.0(1.4)	10.98
$_{81}$Tl	11.28(68)[2]	11.1(2.0)	7.82(73)	8.7(1.7)	10.33
$_{83}$Bi	12.50(45)	12.3(2.0)	7.27(54)	8.6(1.7)	10.82
$_{95}$Am	16.63(30)[2]	-	7.96(1.40)	-	11.49

[1]From the curve calculated in [4] for the lanthanide region (see text) [2]Interpolated value (see text)

Table 5: M_3 atomic level widths. Present results were deduced from the transition widths quoted in Table 4 and the L_1 level widths reported in [4] or interpolated from the latter. For comparison the L_1 and M_2 widths recommended by Campbell and Papp [1] and theoretical M_2 widths of Perkins are also indicated.

Perkins probabilities [11] of all allowed M_3 CK transitions for elements $65 \leq Z \leq 95$ are listed in Table 6. The broken curve in Fig. 22 corresponds to Perkins total M_3 level widths obtained by summing his computed radiative and non-radiative rates. The puzzling variations observed in this curve are fully accounted for by the changes in the probabilities of the CK transitions listed in Table 6. The drop around Z = 74 is due to the closing of the $M_3M_4N_3$ and $M_3M_5N_2$ CK channels while the drops occurring at Z = 80, 86, 91 and 95 are due respectively to the closing of the $M_3M_5N_3$, $M_3M_4N_{4,5}$ and $M_3M_5N_{4,5}$ channels. The solid curve in Fig. 22 corresponds to the M_3 level widths recommended by Campbell and Papp. The latter were obtained by subtracting their own recommended L_1 level widths from the L_1M_3 XES measurements of Salem [2] in the Z region $58 \leq Z \leq 72$, those of Cooper [3] in the Z region $73 \leq Z \leq 81$ and those performed previously by our group for ^{90}Th [10] and ^{92}U [9]. As noted by Campbell and Papp in Ref. [41], for the three elements $_{78}$Pt, $_{79}$Au and $_{81}$Tl, there are discrepancies between Cooper's data published in 1942 [27] (full triangles in Fig. 22) and those published in 1944 [3] (open triangles in Fig. 22). However, because there were no other

available data, they extracted their recommended M_3 level widths from the less old Cooper's data, i.e., those of 1944 [3].

Z Term	65	67	69	70	71	72	73
$M_3M_4N_2$	$1.39\ 10^{-2}$	$1.28\ 10^{-2}$	-	-	-	-	-
N_3	$6.68\ 10^{-2}$	$6\ 10^{-2}$	$5.48\ 10^{-2}$	$5.24\ 10^{-2}$	$5.14\ 10^{-2}$	$5.22\ 10^{-2}$	$2.77\ 10^{-2}$
N_4	$1.1\ 10^{-2}$	$1.03\ 10^{-2}$	$9.71\ 10^{-3}$	$9.4\ 10^{-3}$	$9.12\ 10^{-3}$	$8.89\ 10^{-3}$	$1.02\ 10^{-2}$
N_5	$9.79\ 10^{-3}$	$9.38\ 10^{-3}$	$9.11\ 10^{-3}$	$8.94\ 10^{-3}$	$8.74\ 10^{-3}$	$8.61\ 10^{-3}$	$9.94\ 10^{-3}$
$N_{6,7}$	$2.49\ 10^{-2}$	$2.77\ 10^{-2}$	$3.04\ 10^{-2}$	$3.1\ 10^{-2}$	$3.13\ 10^{-2}$	$3.14\ 10^{-2}$	$3.63\ 10^{-2}$
$O_{1,2,3}$	$1.02\ 10^{-3}$	$9.1\ 10^{-3}$	$8.27\ 10^{-3}$	$7.82\ 10^{-3}$	$7.84\ 10^{-3}$	$7.91\ 10^{-3}$	$9.36\ 10^{-3}$
$M_3M_5N_2$	$8.99\ 10^{-2}$	$8.26\ 10^{-2}$	$7.8\ 10^{-2}$	$7.6\ 10^{-2}$	$7.49\ 10^{-2}$	$7.28\ 10^{-2}$	-
N_3	$1.51\ 10^{-1}$	$1.36\ 10^{-1}$	$1.24\ 10^{-1}$	$1.18\ 10^{-1}$	$1.13\ 10^{-1}$	$1.09\ 10^{-1}$	$1.23\ 10^{-1}$
N_4	$4.85\ 10^{-2}$	$4.56\ 10^{-2}$	$4.34\ 10^{-2}$	$4.21\ 10^{-2}$	$4.08\ 10^{-2}$	$3.98\ 10^{-2}$	$4.57\ 10^{-2}$
N_5	$7.19\ 10^{-2}$	$6.64\ 10^{-2}$	$6.22\ 10^{-2}$	$6\ 10^{-2}$	$5.78\ 10^{-2}$	$5.61\ 10^{-2}$	$6.41\ 10^{-2}$
$N_{6,7}$	$2.14\ 10^{-1}$	$2.41\ 10^{-1}$	$2.68\ 10^{-1}$	$2.76\ 10^{-1}$	$2.79\ 10^{-1}$	$2.82\ 10^{-1}$	$3.29\ 10^{-1}$
$O_{1,2,3}$	$4.08\ 10^{-2}$	$3.62\ 10^{-2}$	$3.32\ 10^{-2}$	$3.15\ 10^{-2}$	$3.15\ 10^{-2}$	$3.18\ 10^{-2}$	$3.76\ 10^{-2}$

Z Term	74	75	76	77	78	79	80
$M_3M_4N_2$	-	-	-	-	-	-	-
N_3	-	-	-	-	-	-	-
N_4	$1.04\ 10^{-2}$	$1.03\ 10^{-2}$	$1.02\ 10^{-2}$	$9.93\ 10^{-3}$	$9.8\ 10^{-3}$	$1.04\ 10^{-2}$	$1.15\ 10^{-2}$
$M_3M_4N_5$	$1.02\ 10^{-2}$	$1.01\ 10^{-2}$	$1.01\ 10^{-2}$	$9.96\ 10^{-3}$	$9.88\ 10^{-3}$	$1.05\ 10^{-2}$	$1.15\ 10^{-2}$
$N_{6,7}$	$3.79\ 10^{-2}$	$3.78\ 10^{-2}$	$3.73\ 10^{-2}$	$3.71\ 10^{-2}$	$3.7\ 10^{-2}$	$3.88\ 10^{-2}$	$4.3\ 10^{-2}$
$O_{1,2,3}$	$9.84\ 10^{-3}$	$9.94\ 10^{-3}$	$1\ 10^{-2}$	$1.01\ 10^{-2}$	$1.03\ 10^{-2}$	$1.1\ 10^{-2}$	$1.25\ 10^{-2}$
$M_3M_5N_2$	-	-	-	-	-	-	-
N_3	$1.23\ 10^{-1}$	$1.19\ 10^{-1}$	$1.19\ 10^{-1}$	$1.16\ 10^{-1}$	$1.1\ 10^{-1}$	$7.34\ 10^{-2}$	-
N_4	$4.68\ 10^{-2}$	$4.59\ 10^{-2}$	$4.51\ 10^{-2}$	$4.44\ 10^{-2}$	$4.38\ 10^{-2}$	$4.63\ 10^{-2}$	$5.08\ 10^{-2}$
N_5	$6.53\ 10^{-2}$	$6.37\ 10^{-2}$	$6.25\ 10^{-2}$	$6.12\ 10^{-2}$	$6.03\ 10^{-2}$	$6.34\ 10^{-2}$	$6.94\ 10^{-2}$
$N_{6,7}$	$3.45\ 10^{-1}$	$3.46\ 10^{-1}$	$3.44\ 10^{-1}$	$3.46\ 10^{-1}$	$3.48\ 10^{-1}$	$3.68\ 10^{-1}$	$4.12\ 10^{-1}$
$O_{1,2,3}$	$3.97\ 10^{-2}$	$4.03\ 10^{-2}$	$4.07\ 10^{-2}$	$4.07\ 10^{-2}$	$4.14\ 10^{-2}$	$4.45\ 10^{-2}$	$5.05\ 10^{-2}$
$O_{4,5}$	$1.3\ 10^{-3}$	$3.09\ 10^{-3}$	$4\ 10^{-3}$	$3.19\ 10^{-3}$	$6.4\ 10^{-3}$	$7.96\ 10^{-3}$	$9.84\ 10^{-3}$

Z Term	81	82	83	84	85	86	87
$M_3M_4N_2$	-	-	-	-	-	-	-
N_3	-	-	-	-	-	-	-
N_4	$1.14\ 10^{-2}$	$1.12\ 10^{-2}$	$1.09\ 10^{-2}$	$6.19\ 10^{-3}$	-	-	-
N_5	$1.16\ 10^{-2}$	$1.14\ 10^{-2}$	$1.15\ 10^{-2}$	$1.23\ 10^{-2}$	$1.19\ 10^{-2}$	-	-
$N_{6,7}$	$4.25\ 10^{-2}$	$4.2\ 10^{-2}$	$4.13\ 10^{-2}$	$4.1\ 10^{-2}$	$4.08\ 10^{-2}$	$4.08\ 10^{-2}$	$4.04\ 10^{-2}$
$O_{1,2,3}$	$1.27\ 10^{-2}$	$1.29\ 10^{-2}$	$1.31\ 10^{-2}$	$1.34\ 10^{-2}$	$1.37\ 10^{-2}$	$1.43\ 10^{-2}$	$1.45\ 10^{-2}$
$O_{4,5}$	$2.07\ 10^{-3}$	$2.25\ 10^{-3}$	$2.41\ 10^{-3}$	$2.6\ 10^{-3}$	$2.79\ 10^{-3}$	$3\ 10^{-3}$	$3.15\ 10^{-3}$
$M_3M_5N_2$	-	-	-	-	-	-	-
N_3	-	-	-	-	-	-	-
N_4	$5.02\ 10^{-2}$	$4.93\ 10^{-2}$	$4.84\ 10^{-2}$	$4.84\ 10^{-2}$	$4.88\ 10^{-2}$	$4.97\ 10^{-2}$	$4.91\ 10^{-2}$
N_5	$6.86\ 10^{-2}$	$6.73\ 10^{-2}$	$6.58\ 10^{-2}$	$6.57\ 10^{-2}$	$6.52\ 10^{-2}$	$6.61\ 10^{-2}$	$6.51\ 10^{-2}$
$N_{6,7}$	$4.1\ 10^{-1}$	$4.09\ 10^{-1}$	$4.2\ 10^{-1}$	$4.1\ 10^{-1}$	$4.15\ 10^{-1}$	$4.2\ 10^{-1}$	$4.22\ 10^{-1}$
$O_{1,2,3}$	$5.16\ 10^{-2}$	$5.22\ 10^{-2}$	$5.28\ 10^{-2}$	$5.42\ 10^{-2}$	$5.56\ 10^{-2}$	$5.77\ 10^{-2}$	$5.86\ 10^{-2}$
$O_{4,5}$	$1.09\ 10^{-2}$	$1.17\ 10^{-2}$	$1.25\ 10^{-2}$	$1.33\ 10^{-3}$	$1.42\ 10^{-2}$	$1.51\ 10^{-2}$	$1.58\ 10^{-2}$

Z Term	88	89	90	91	92	94	95
$M_3M_4N_2$	-	-	-	-	-	-	-
N_3	-	-	-	-	-	-	-
N_4	-	-	-	-	-	-	-
N_5	-	-	-	-	-	-	-
$N_{6,7}$	$3.98\ 10^{-2}$	$3.91\ 10^{-2}$	$3.88\ 10^{-2}$	$4.07\ 10^{-2}$	$4.02\ 10^{-2}$	$3.93\ 10^{-2}$	$4.11\ 10^{-2}$
$O_{1,2,3}$	$1.47\ 10^{-2}$	$1.5\ 10^{-2}$	$1.53\ 10^{-2}$	$1.66\ 10^{-2}$	$1.68\ 10^{-2}$	$1.76\ 10^{-2}$	$1.92\ 10^{-2}$
$O_{4,5}$	$3.28\ 10^{-3}$	$3.44\ 10^{-3}$	$3.6\ 10^{-3}$	$3.93\ 10^{-3}$	$4.02\ 10^{-3}$	$4.29\ 10^{-3}$	$4.71\ 10^{-2}$
$M_3M_5N_2$	-	-	-	-	-	-	-
N_3	-	-	-	-	-	-	-
N_4	$4.83\ 10^{-2}$	$4.89\ 10^{-2}$	$4.4\ 10^{-2}$	-	-	-	-
N_5	$6.46\ 10^{-2}$	$6.43\ 10^{-2}$	$6.36\ 10^{-2}$	$6.86\ 10^{-2}$	$6.54\ 10^{-2}$	$6.14\ 10^{-2}$	-
$N_{6,7}$	$4.23\ 10^{-1}$	$4.23\ 10^{-1}$	$4.28\ 10^{-1}$	$4.57\ 10^{-1}$	$4.61\ 10^{-1}$	$4.76\ 10^{-1}$	$5.16\ 10^{-1}$
$O_{1,2,3}$	$5.94\ 10^{-2}$	$6.05\ 10^{-2}$	$6.18\ 10^{-2}$	$6.7\ 10^{-2}$	$6.79\ 10^{-2}$	$7.13\ 10^{-2}$	$7.76\ 10^{-2}$
$O_{4,5}$	$1.64\ 10^{-2}$	$1.7\ 10^{-2}$	$1.76\ 10^{-2}$	$1.91\ 10^{-2}$	$1.94\ 10^{-2}$	$2.03\ 10^{-2}$	$2.21\ 10^{-2}$

Table 6: Results of independent-particle model calculations of M_3 CK transition rates for elements with atomic numbers $65 \leq Z \leq 95$ (taken from Ref. [11]).

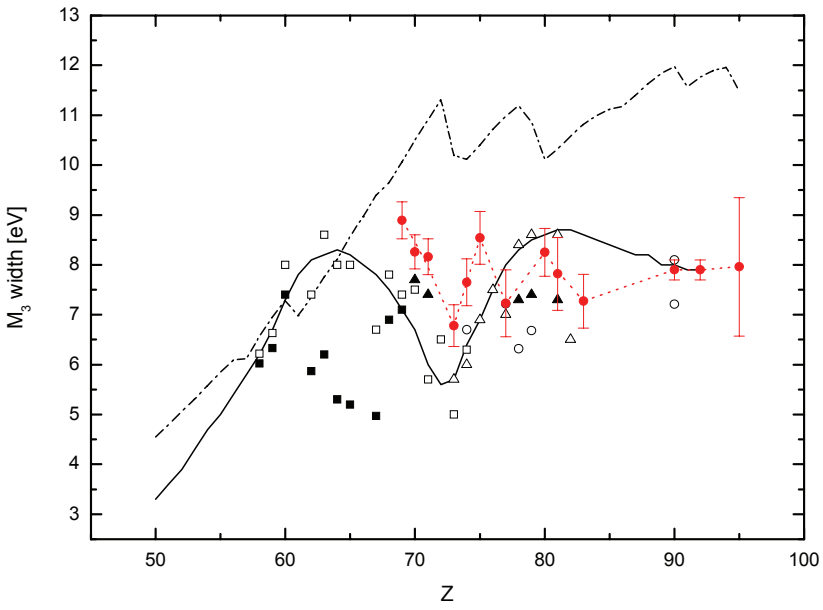

Fig. 22: M_3 level width versus atomic number. The dashed dotted line represents the independent particle model calculations of Perkins et al [11], the solid line the recommended values of Campbell and Papp [1]. Experimental data are results derived from L_1M_3 XES measurements using the following symbols: ○ Ref. [6, 7, 8], Δ Ref. [3], ▲ Ref. [28], ● Refs. [9, 10, 13] and present work, ■ and □ Ref. [2] assuming the L_1 widths from [4] and [1], respectively. The dotted line serves to guide the eye.

As shown in Fig. 22, in the Z region $69 \leq Z \leq 74$, our results (red circles) exceed those of Salem and Lee [2], suggesting the possibility that the M_3 level widths extracted from L_1M_3 line width measurements of Salem and Lee for lower atomic numbers ($58 \leq Z \leq 68$) might be also too low. Our data lie also systematically above those of Cooper [27]. However, as already reported in [42], Cooper's data were probably overcorrected for the instrumental response. Furthermore, it can be seen in Fig. 22 that all experimental data lie significantly lower than the Perkins theoretical predictions [11]. Actually, Perkins himself mentioned that his computed CK transition rates may overestimate the true values by a factor up to two due to the small binding energies differences. This was also pointed out by Campbell and Papp [1, 41] who observed that Perkins calculations exceed largely the experimental widths for all levels dominated by CK decay, while they provide a fairly good approximation for other levels.

	Z+1 rule	Perkins [11]	This work
$M_3M_5N_2$	71	73	72 or 73
$M_3M_4N_3$	72	74	72 or 73
$M_3M_5N_3$	77	80	76 or 77
$M_3M_4N_4$	83	85	82 or 83
$M_3M_4N_5$	84	86	82 or 83
$M_3M_5N_4$	89	91	-
$M_3M_5N_5$	91	95	-

Table 7: Cut-off atomic numbers of the $M_3M_4N_{3,4,5}$ and $M_3M_5N_{2,3,4,5}$ CK transitions.

Finally, it can be noted that our experimental values reveal the same puzzling variations as those observed in Perkins's curve. However, they do not peak at the same atomic numbers indicating that the CK cut-off atomic numbers derived from the present measurements do not correspond to those predicted by Perkins's calculations. Table 7 presents the cut-off atomic numbers deduced from our measurements, those predicted by Perkins and the Z+1 rule using the experimental binding energies tabulated by Storm and Israel [43]. The Z+1 rule appears to provide cut-off atomic numbers that are in better agreement with our experimental data than those deduced from Perkins calculations which yield systematically higher values. This may indicate that Perkins calculations overestimate the CK transition energies. Similar observations were done by Campbell for the $M_4M_5N_{4,5}$ CK transitions. For the latter Perkins predicts indeed the onset at Z = 49, while Martensson [44] measured a maximum rate for $_{44}$Ru and $_{45}$Rh and the cut-off at Z=47. Similarly, for the $L_2L_3M_5$ and $L_2L_3M_4$ CK transitions, the onsets are predicted by Perkins at Z = 88 and Z = 91, respectively, whereas measurements of L_2L_3 CK transition probabilities yield to onsets at Z = 92 and Z = 94. Note that for these three CK

transitions, the Z+1 approach provides a good agreement with experiment (Z = 47 for the cut-off of the $M_4M_5N_{4,5}$ transition and Z= 91 and 93, respectively, for the onsets of the $L_2L_3M_5$ and $L_2L_3M_4$ transitions).

The drop in the M_3 level width corresponding to the closing of the $M_3M_4N_{4,5}$ CK channels is much more pronounced in our experimental data indicating that Perkins's predictions underestimate probably the rates of these CK transitions. Concerning the closing of the $M_3M_5N_{4,5}$ CK channel, no clear conclusion could be deduced from Fig. 22, the error on the M_3 level width of Am obtained in this work being too large.

4.3.2.2 M_2 level widths

Present results for the M_2 level widths are presented in Table 8 and in Fig. 23 where they are compared to other existing experimental and theoretical data. In general, similar conclusions as those given for the M_3 level widths can be drawn. Except for Bi, present results are indeed bigger by about 30% than the values recommended by Campbell and Papp and smaller than Perkins theoretical predictions.

Element	L_1 width [4] [eV]	L_1 width [1] [eV]	M_2 width [eV] Present	M_2 width [eV] Campbell [1]	M_2 width [eV] Perkins [11]
$_{69}$Tm	5.45(32)[1]	4.9(1.5)	7.83(43)	6.85(86)	9.94
$_{70}$Yb	5.40(30)	5.2(1.5)	9.60(39)	7.1(9)	10.32
$_{71}$Lu	5.65(33)[2]	5.4(1.5)	9.79(40)	7.3(1.0)	10.65
$_{73}$Ta	6.16(40)[2]	6.0(1.5)	9.33(45)	7.8(1.1)	10.27
$_{74}$W	6.41(43)	6.3(1.5)	9.82(52)	8.1(1.2)	11.54
$_{75}$Re	6.94(50)[2]	6.7(1.5)	11.49(56)	8.4(1.3)	11.8
$_{77}$Ir	8.02(63)[2]	7.9(2.0)	11.59(71)	8.9(1.5)	12.26
$_{81}$Tl	11.28(68)[2]	11.1(2.0)	13.65(83)	10.1(1.9)	13.13
$_{83}$Bi	12.50(45)	12.3(2.0)	10.51(51)	10.7(2.2)	13.5
$_{95}$Am	16.63(30)[2]	-	13.84(1.20)	-	15.47

[1] From the curve calculated in [4] for the lanthanide region (see text). [2]Interpolated value (see text).

Table 8: Same as Table 5 but for the M_2 atomic level widths.

In Fig. 23, Campbell's recommended values are again almost entirely based on Salem's and Cooper's XES measurements. We have re-calculated the M_2 level widths in the region $58 \leq Z \leq 66$ using the L_1M_2 line widths of Salem and Lee and the L_1 level widths of Raboud and we have compared the obtained results to the values extracted from the present L_1M_2 XES measurements and other previous L_1M_2 XES measurements of the Fribourg group concerning

$_{67}$Ho [4], $_{80}$Hg [13], $_{90}$Th [10] and $_{92}$U [10]. From the comparison, one sees that in the region $67 \leq Z \leq 74$, Salem's data lie clearly below the Fribourg values and this may indicate, as it was the case for the M_3 level width, that the whole set of M_2 level widths obtained from Salem's measurements lies too low. In addition Salem's data reveals a drop around Z = 63 which is not predicted by Perkins's calculations nor by the Z+1 approach.

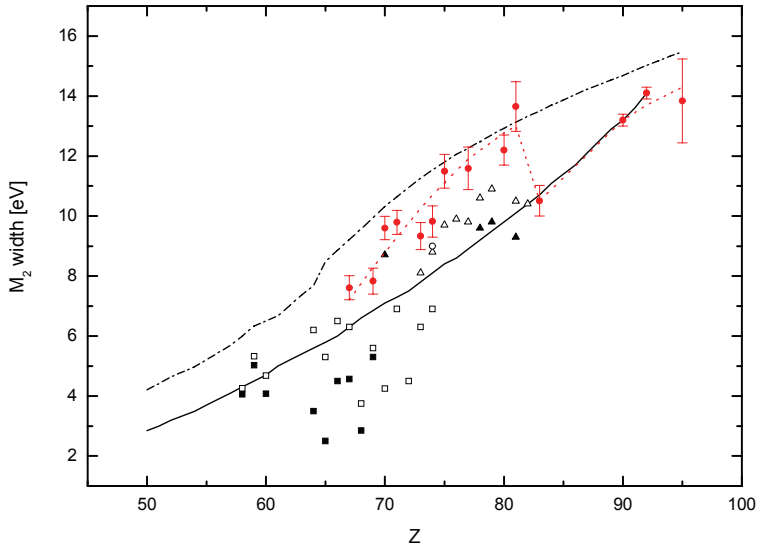

Fig. 23: M_2 level width versus atomic number. The dashed dotted line represents the theoretical results of Perkins et al [11], the solid line the recommended values of Campbell and Papp [1]. Experimental data were derived from L_1M_2 XES measurements (see text for explanation) using the following symbols: ○ Ref. [7] Δ Ref. [3], ▲ Ref. [27], ● Refs. [4, 9, 10, 13] and present work, ■ and □ Ref. [2] assuming the L_1 widths from [4] and [1], respectively. The dotted line serves to guide the eye.

According to the Z+1 approach, the $M_2M_4N_1$ CK transition becomes forbidden at Z = 86, so may be the closing of this CK channel explains the abrupt drop in our data at Z = 83. Perkins calculations, however, do not predict this drop and show, on the contrary, that the $M_2M_4N_1$ CK transitions are allowed for all elements with atomic numbers $21 \leq Z \leq 100$. On the other hand, Perkins's calculations predict, in contrast to the Z+1 rule, that the $M_2M_5N_4$ CK transition becomes forbidden at Z = 74 and then allowed again from Z = 79. This may explain the drop observed in our data at Z = 73 and the almost linear increase occuring between Z = 77 and Z = 81.

Chapter 5

Concluding remarks

High-resolution measurements of the photo-induced L_1M_2 and L_1M_3 x-ray emission lines of $_{69}$Tm, $_{70}$Yb, $_{71}$Lu, $_{74}$W, $_{75}$Re, $_{77}$Ir, $_{81}$Tl, $_{83}$Bi and $_{95}$Am were performed. The fluorescence x-ray spectra were produced by irradiating the targets with the bremsstrahlung of x-ray tubes. Elements up to $_{77}$Ir were measured with a Bragg-type von Hamos crystal spectrometer. As this instrument cannot be used efficiently for photon energies above about 11 keV, elements with higher atomic numbers were measured with a Laue-type Dumond crystal spectrometer.

From the fits of the measured high-resolution x-ray spectra, accurate sets of values for the energies and widths of the $L_1M_{2,3}$ transitions were obtained. Assuming for the L_1 levels the widths reported recently by Raboud et al. [4], the widths of the M_2 and M_3 atomic levels could be determined. Except for Am for which the fluorescence x-ray emission was very weak due to the tiny dimensions of the sample, present results are in general 3-5 times more accurate that former existing data.

The transition energies were compared to the values compiled recently by Deslattes et al. [22]. In general, a satisfactory agreement was observed, except for some few elements for which the values quoted in [22] are obviously wrong. Note that for the elements investigated in the present work all values reported in [22] correspond to old measurements performed by Bearden in the late sixties. One would like to emphasize that a very good agreement was found, however, with the theoretical MBPT transition energies that are also quoted in [22].

The results obtained from the transition widths and atomic level widths were compared to the values tabulated recently by Campbell and Papp [1] and to theoretical predictions of Perkins [11] based on the independent-particle model. In general, our results are significantly bigger than the values quoted in [1] and smaller than the theoretical predictions of Perkins. The sudden drops and enhancements observed in the plots of the $M_{2,3}$ level widths versus atomic number Z could be explained satisfactorily by the cut-offs and onsets of the $M_2M_4N_1$, respectively $M_3M_4N_{3,4,5}$ and $M_3M_5N_{2,3}$ CK transitions. In particular it was found that the values of Z at which abrupt steps were observed in the plots could be well reproduced in most

cases using the Z+1 semi-empirical rule for the calculation of the CK cut-off and onset energies.

Bibliography

[1] J.L. Campbell and T. Papp:
''Widths of the atomic K-N_7 levels.''
At. Data Nucl. Data Tables **77** (2001) 1.

[2] S.I. Salem and P.L. Lee:
''Widths of the L x-ray lines of the rare-earth elements.''
Phys. Rev. A **10** (1974) 2033.

[3] J.N. Cooper:
''Auger transitions and widths of x-ray energy levels.''
Phys. Rev. **65** (1944) 155.

[4] P.A. Raboud, M. Berset, J.-Cl. Dousse and Y-P. Maillard:
''L_1 atomic-level width of elements $62 \leq Z \leq 83$.''
Phys. Rev. A **65** (2002) 022512.

[5] U. Werner and W. Jitschin:
''L-vacancy decay in heavy elements ($72 \leq Z \leq 82$) by the synchrotron photoionization method.''
Phys. Rev. A **38** (1988) 4009.

[6] J. Wigger:
Dissertation (1985), University of Muenster (unpublished): results taken from Ref. [1].

[7] A.M Vlaicu et al. :
''Investigation of the $_{74}$W L emission spectra and satellites.''
Phys. Rev. A **58** (1998) 3544.

[8] P. Amorim, L. Salgueiro, F. Parente and J.G. Ferreira:
''Widths of some L x-ray lines of iridium, platinum, gold, thorium and uranium.''
J. Phys. B. **21** (1988) 3851.

[9] J. Hoszowska, J.-Cl Dousse and Ch. Rhême:
'Linewidths of photoinduced L x rays of uranium.''
Phys. Rev. A **50** (1994) 123.

[10] P.-A. Raboud, J.-Cl Dousse, J. Hoszowska and I. Savoy:
'' L1 to N5 atomic level widths of thorium and uranium as inferred from measurements of L and M x-ray spectra.''
Phys. Rev. A **61** (1999) 012507.

[11] S. T Perkins, D. E Cullen, M.H Chen, J. H Hubbell, J. Rathkopf and J. Scofield:
''Tables and Graphs of Atomic Subshell Relaxation Data derived from the LLNL Evaluated Atomic Data Library (EADL), Z=1-100.''
Lawrence Livermore National Laboratory Report UCRL-50400, Vol. **30** (1991).

[12] J. L. Campbell, private communication.

[13] Y.-P Maillard, J.-Cl Dousse, J. Hoszowska, M. Berset, P.-A Raboud:
''Energies and widths of atomic core-levels in liquid mercury.''
(In preparation.)

[14] J. C. Fuggle and S. F. Alvarado:
''Core-level lifetimes as determined by x-ray photoelectron spectroscopy measurements.''
Phys. Rev. A **22** (1980) 1615.

[15] A. Messiah:
''Quantum Mechanics.''
North-Holland, Amsterdam (1961), p:401.

[16] V. Weisskopf and E. Wigner:
Z. Phys. **100** (1930) 74.

[17] E. Arnous and W. Heitler:
Proc. Roy. Soc. (London) A **220**, 290.

[18] W. Bambynek, B. Crasemann, R. W. Fink, H.-U. Freund, H. Mark, C. D. Swift, R. E. Price and P. Venugopala Rao:
''X-ray fluorescence yields, Auger, and Coster-Kronig transition probabilities.''
Rev. Mod. Phys. **44** (1972) 716.

[19] J-Cl. Dousse and J. Hoszowska:
''L- and M-shell-electron shake processes following 1s photoionization in argon and krypton.''
Phys. Rev. A **56** (1997) 4517.

[20] J. Hoszowska, J.-Cl. Dousse, J. Kern and Ch. Rhême:
'' High resolution von Hamos crystal x-ray spectrometer.''
Nucl. Instrum. Methods Phys. Res. A **376** (1996) 129.

[21] R. D. Deslattes, and E. G. Kessler:
Atomic Inner-Shell Physics, edited by B. Crasemann (Plenum, New York) pp. 181 (1985).

[22] E. G. Kessler, Jr., R. D. Deslattes, D. Girard, W. Schwitz, L. Jacobs, and O. Renner:
''Mid-to-high-Z precision x-ray measurements.''
Phys. Rev. A **26** (1982) 2696.

[23] D. R. Deslattes, G. E. Kessler, P. Indelicato, L. de Billy, E. Lindroth, J. Anton:
''X-ray transition energies: new approach to a comprehensive evaluation.''
Rev. Mod. Phys **75** (2003) 35.

[24] O. Mauron, J.-Cl. Dousse, S. Baechler, M. Berset, Y.P. Maillard, P.A. Raboud and J. Hoszowska:
''Revisited L3 and M1 atomic-level widths of elements 54≤Z≤77.''
Phys. Rev. A **67** (2003) 032506.

[25] J. A. Bearden:
''X-Ray Wavelengths.''
Rev. Mod. Phys. **39** (1967) 78.

[26] J. P. Desclaux:
''Relativistic Dirac-Fock expectation values for atoms with Z = 1 to Z = 120.''
At. Data and Nucl. Data Tables **12** (1973) 311.

[27] J.N Cooper:
''The Auger effect in relative intensities and widths of x-ray lines.''
Phys. Rev. **61** (1942) 234.

[28] M. H. Chen, B. Crasemann, and H. Mark:
''Radiationless transitions to atomic M1,2,3 shells: Results of relativistic theory.''
Phys. Rev. A **27** (1983) 2989.

[29] M. H. Chen, B. Crasemann, and H. Mark:
''Relativistic M-*shell radiationless transitions.''*
Phys. Rev. A **21** (1980) 449.

[30] D. Coster and R. DeL. Kronig:
Physica **2** (1935) 14.

[31] E. J. McGuire:
''Atomic M-Shell Coster-Kronig, Auger, and Radiative Rates, and Fluorescence Yields for Ca-Th.''
Phys. Rev. A **5** (1972) 1043.

[32] J. H. Scofield:
''Exchange corrections of K *x-ray emission rates.''*
Phys. Rev. A **9** (1974) 1041.

[33] M. Ohno:
*''Theoretical studies of the 3*s *and 3*p *linewidths of the elements Kr to Xe.''*
Phys. Rev. B **29** (1984) 3127.

[34] R.L. Cohen, G.K. Werthein, A. Rosencwaig, and H.J. Guggenhein:
*''Multiplet Splitting of the 4*s *and 5*s *Electrons of the Rare Earths.''*
Phys. Rev. B **5** (1972) 1037.

[35] I. Arcon, A. Kodre, M. Štuhec, D. Glavic-Cindro, and W. Drube:
''Multielectron excitations in the L-subshell photoabsorption of xenon.''
Phys. Rev. A **51** (1995) 147.

[36] O. Keski-Rahkonen, G. Materlik, B. Sonntag, and J. Tulkki:
''The L level x-ray absorption spectra of atomic barium and mercury.''
J. Phys. B: At. Mol. Phys. (1984) L121.

[37] R. Stötzel, U. Werner, M. Sarkar, and W. Jitschin:
''Unexpectedly small intrashell L_1-L_3 vacancy transition rate in $_{62}$Sm.''
J. Phys. A **45** (1992) 2093.

[38] T. Papp, J. L. Campbell, and S. Raman:
''Fluorescence and Coster-Kronig yields of the L_1 shell in gadolinium.''
Phys. Rev. A **58** (1998) 3537.

[39] U. Werner and W. Jitschin:
''*L-vacancy decay in heavy elements (72≤Z≤82) by the synchrotron photoionization method.''*
Phys. Rev. A **38** (1988) 4009.

[40] M. Ohno and R. E. LaVilla:
''Xenon L emission spectra and many-electron effects in core levels.''
Phys. Rev. A **45** (1992) 4713.

[41] J. L. Campbell and T. Papp:
''Atomic level widths for x-ray spectrometry.''
X-ray Spectrometry **24** (1995) 307.

[42] S. A. Salem and P. L. Lee:
''Experimental widths of K and L x-ray lines.''
At. Data and Nucl. Data Tables **18** (1976) 234.

[43] E. Storm and H.I. Israel:
''Photon cross sections from 1 keV to 100 MeV for elements Z=1 to Z=100.''
Nucl. Data Tables **7** (1970) 565.

[44] N. Mårtensson and R. Nyholm:
''*Electron spectroscopic determinations of M and N core-hole lifetimes for the elements Nb—Te (Z=41-52).*''
Phys. Rev. B **24** (1981) 7121.

Part II:

Double K-shell ionization of Al induced by photon and electron impact

Chapter 1

Introduction

1.1 Motivation

The investigation of the excitation dynamics and decay processes in multiply ionized atoms is a particularly important tool to explore the details of the atomic structure. In order to gain a deeper understanding of the latter and to better test and improve theoretical models, there is an increasing interest in studying exotic atomic systems where unusual excitations and rare decay modes can be probed. Hollow atoms, i.e., atoms where the innermost shell is empty while the outer shells are occupied are examples of such exotic systems. Hollow atoms can be created either by producing a double K-shell ionization of neutral atoms or via multiple electron capture by fully stripped ions in interaction with metallic surfaces. The radiative de-excitation of hollow atoms leads to the emission of so-called K x-ray hypersatellites ($K\alpha^h$, $K\beta^h$,…). The intensity ratio of $K\alpha_1^h$ ($[1s^{-2}] \rightarrow [1s^{-1}2p_{3/2}^{-1}]$) to $K\alpha_2^h$ ($[1s^{-2}] \rightarrow [1s^{-1}2p_{1/2}^{-1}]$) hypersatellite lines is a very effective tool to study the variation of the coupling scheme with the atomic number Z. Precise measurements of the hypersatellite transition energies can also be used to learn more about the Breit interaction and relativistic effects. Furthermore, because of the strong correlations between the two 1s vacancies, hollow atoms provide a good opportunity to investigate the effects of electron correlations in atoms. This aspect is particularly important since the concept of electron correlations is central in various areas of physics [1]. Correlation effects are strongly reflected in hollow atoms resulting from double K-shell ionization of neutral atoms by photons or light ion impact since in this case they represent almost the single mechanism by which the double K-shell ionization is produced.

The ratio of double to single K-shell photo-ionization cross sections was first observed in helium by Carlson in 1967 [2]. In the same year Byron et al. [3] published the first calculations of this ratio, and since then, several experimental and theoretical studies have been done. Synchrotron radiation sources, allowing the production of monochromatic highly collimated and extremely intense photon beams at any energy have revolutionized the experimental research on multiple photo-ionization. The first Kα hypersatellite spectrum produced by means of synchrotron radiation was observed in 1999 by Kanter et al. [4] for Mo. Few similar

measurements were performed for Ca, Ti and V [5], V, Cr, Mn, Fe, Co, Ni, Cu and Zn [6, 7, 8], Ne [9] and Ag [10]. These experiments as well as those performed using charged particle impact, in addition to (hν,2e) and (e,3e) kinematics experiments [11, 12], have provided further insights to atomic physicists in their efforts to better understand multi-ionization mechanisms.

In the present work which is a continuation of these efforts, we report on measurements of the Al Kα hypersatellite spectra. The latter were obtained by bombarding metallic aluminium foils with mono-energetic beams of photons and electrons at different energies. To our knowledge, our measurements with synchrotron radiation represent the first observation of photo-induced K hypersatellites in the case of Al. Actually; this work has been done within a wider project concerning the study of the double K-shell ionization in light atoms by means of high resolution spectroscopy. The purpose was to overcome the lack of experimental data in these elements and to better probe the Z-dependence of the double K-shell ionization cross section.

Besides the precise determination of the energy and line width of the Al $K\alpha^h$ hypersatellite x-ray line, the aim of the present work was also to determine with high accuracy the energy dependence of both photon- and electron-induced double K-shell ionization cross section from threshold to the expected broad maximum, to probe the current theoretical models describing this dependence, and particularly to compare photon- and electron-induced double K-shell ionization cross sections in order to better understand the mechanisms by which the double 1s vacancy production is achieved in each case.

1.2 Methods to produce double 1s vacancy states

They are two ways to produce a double ionization of neutral atoms, direct processes where the two electrons are ejected without any internal rearrangement of the other bound electrons, and indirect processes in which the ejection of a single inner-shell electron is followed by Auger decay. The double K-shell ionization can only result from direct processes since the $1s^{-2}$ configuration cannot be obtained as an Auger final state. For charged particles, as many inner-shell electrons can feel the Coulomb potential of the projectile, several of them can be ionized quasi-simultaneously as a result of the charged projectile impact. This process named Direct Coulomb ionization (DCI) is the main process in heavy-ion induced multi-ionization of neutral atoms (see, e.g., [13]). For photons, direct processes include two different mechanisms: the shake-off (SO) and knock-out (KO) processes. For electrons a further direct process is possible, namely the above mentioned DCI excitation channel which is specifically named

two-step-two process (TS2) for light charged particles. The shake-off process is a one-step mechanism in which one of the target electrons is removed by photo-ionization or by impact with a charged particle, and then because of the abrupt change in the atomic potential resulting from the first ionization, a second electron is ejected during the relaxation process of the remaining ion. The KO process is a two-step mechanism in which the first ionized electron hits a second bound electron which is then kicked out. This mechanism is alternatively referred to as a two-step-one (TS1) process. The TS2 process is also a two-step mechanism; here the two electrons are emitted by two subsequent interactions between the incident charged projectile and two target electrons. SO and KO processes are sometimes referred to as final state correlations (FSC) since they correspond to electron-electron interactions following the projectile-target collision, while GSC denotes the electron-electron interactions in the ground state occurring before the collision with the projectile. The term SO denotes usually the SO process plus the GSC.

Depending on the excitation mode, specific processes are responsible for the production of double K-shell vacancy states. In photo-absorption, the TS2 process is not possible since the incident photon is annihilated during the interaction so that the multi-ionization can proceeds only through e-e correlations. These correlations were long thought to be due mainly to ground states correlations (GSC) and shake-off processes (SO). Using the many-body perturbation theory (MBPT), Carter and Kelly [14] and Ishirara, Hino and McGuire [15] demonstrated that a large contribution in double photo-absorption probability originates from the knock-out process (KO). This dynamical scattering picture was confirmed by Samson et al. [16] who pointed out that experimental data of double to single photo-ionization cross sections of neutral atoms are proportional to electron impact ionization cross sections of singly charged ions. Recently, with the advent of synchrotron facilities, it has become possible to probe the double K-shell ionization at high x-ray energies. Using such a facility, Levin et al. [17] measured the ratio of double to single photo-ionization cross sections in He at several photons energies from 2 to 12 keV. In a comment on this experiment, Samson et al. [18] stated that at these high energies, the probability of Compton scattering is no more negligible and could be even higher than the photo-absorption probability. In Compton scattering the incident photon is not annihilated, but the probability that it can make two successive Compton scattering at two electrons of the same atom is negligible [19] and then here again electron-electron correlations are the single mechanism by which double K-shell ionization can be produced.

The first experimental studies of hollow atoms have been made using radioactive samples [20, 21, 22]. In this case, the double K-shell ionization is also due to correlation effects. Valuable data were extracted from these studies. However the disadvantage of this excitation

mode is that radioactive sources with long enough lifetimes are needed. In addition only those elements for which natural radioactive isotopes are available can be studied this way. As a consequence, only a limited number of elements could be investigated. As mentioned before, for atomic collisions with light charged particles, in addition to the SO and TS1 processes, double ionization can also occur via the TS2 channel. The latter is expected to dominate for projectile velocities v (in atomic units) and charges q such that $q/v > 0.2$ [23]. For heavier charged projectiles, multi-ionization of atoms can also result from charge transfer processes in which one or more target electrons are captured into an empty shell of the projectile. This process is possible when the binding energy of the projectile state in which the electron is captured is bigger than the binding energy of the target atom state from which the electron is removed. Charge transfer becomes important when heavy bare ions are used as projectiles. The electron capture can occur with the simultaneous emission of a photon (Radiative Electron Capture REC) or without (Electron Capture EC). REC prevails when the heavy-ion velocity is bigger than about twenty times the Bohr velocity $v_0 = \alpha \cdot Z \cdot c$, where α is the fine structure constant. In case of high collision velocities, the captured electron(s) leave the target with the speed of the projectile and then the SO process of additional bound target electron(s) is possible, leading to the production of additional vacancies. Indeed, due to the SO process, significantly higher double K-shell ionization cross sections were observed in He atoms bombarded by fast fully stripped heavy ions, that could not be explained by the DCI and EC processes [24]. However, it should be noted that, in general, hypersatellite data are rather difficult to extract in a reliable way from heavy-ion induced x-ray spectra because the latter are complex, due to the presence of numerous and mostly overlapping satellite lines (see, e.g., [25]).

1.3 Experimental methods to detect double 1s vacancy states

Experimental data for double K-shell ionization cross sections are commonly extracted from the measurements of the ratio of double to single K-shell ionization cross sections which are much easier to perform than measurements of absolute cross sections. The simplest case of double K-shell ionization is the one of the He atom. In this case the ionized ions are extracted from the collision region by a weak electric field, and then they are separated according to their mass-to-charge ratio by a time of flight spectrometer. The ratio of double to single K ionization cross sections is then obtained directly from the time of flight spectra. For atoms beyond He, double K-shell ionization cannot be detected with this ion counting technique. Another method is employed which consists to measure the decay of the 1s vacancies. Actually double K-shell ionization can be identified either by recording the K hypersatallite

transitions in Auger electron spectra (KK-KLL; KK-KLM; …) or in x-ray fluorescence spectra (KK-KL; KK-KM; ...). The ratio of double to single K-shell ionization cross sections is then determined from the intensity ratio of the hypersatellite line to its parent diagram line. The most probable K hypersatellite transitions are those for which one of the two K vacancies is filled by a L-electron, namely KK-KL hypersatellites in x-ray fluorescence spectra and KK-KLX (X =L, M, …) hypersatellites in Auger electron spectra.

Auger spectroscopy is usually used for light atoms because the fluorescence yields of the latter are low. However, this method is limited to gaseous targets or very thin solid samples, due to the strong absorption of low-energy electrons in matter. In addition the analysis of the measured hypersatellite Auger spectra is not easy because multiple Auger final states are possible. For elements with Z>20, x-ray spectroscopy is more appropriate. In this case the K hypersatellite lines can be either observed directly with high resolution crystal spectrometers or detected by measuring in coincidence the emitted hypersatellite (KK-KL) and subsequent satellite (KL-LL) x-rays, using two semiconductors detectors. The coincidence technique, as demonstrated recently by Kanter et al. [10], is preferable to high resolution x-ray spectroscopy in case of heavy elements for which the $K\alpha^h$ hypersatellites lie on the high-energy tails of the ~ 10^5 stronger parent Kα diagram lines. The disadvantage of the coincidence method is that, due to the poor resolution of the semiconductor detectors, only the ratio of double to single K-shell ionization cross sections can be extracted accurately and not the energy of the hypersatellite transitions, nor their natural width.

Hollow atoms may also decay by the emission of a single photon resulting from the simultaneous filling of the two 1s vacancies by a 2s and a 2p electron. In the literature this one-step radiative decay ($1s^{-2} \rightarrow 2s^{-1}2p^{-1}_{1/2,3/2}$) is denoted $K\alpha^h_{1,2}\alpha_3$ and named correlated hypersatellite (CHS) or two-electrons-one-photon transition (TEOP). The probability of this radiative decay mode is, however, much smaller than that of hypersatellite transitions. According to Aberg et al. [26], the branching ratio $I(K\alpha^h_{1,2}\alpha_3)$ / $I(K\alpha^h_{1,2})$ is approximately given by $[K\alpha^h_{1,2}\alpha_3)/E(K\alpha^h_{1,2})]^3 \cdot (0.187/Z)^2$ which corresponds for Al to a ratio of 1.4 10^{-3}. TEOP transitions were observed only in a few metallic samples (Al [27], Fe [28], Ni [29]) bombarded by heavy ions. In general, experimental results were found to be in good agreement with Aberg's theoretical predictions, except in an experiment performed with 3d elements bombarded by electrons for which TEOP yields as strong as those of hypersatellites were obtained [30, 31]. These results, however, could never be reproduced by other groups and seem therefore to be not reliable.

1.4. Hypersatellite x-ray lines

1.4.1 Selection rules

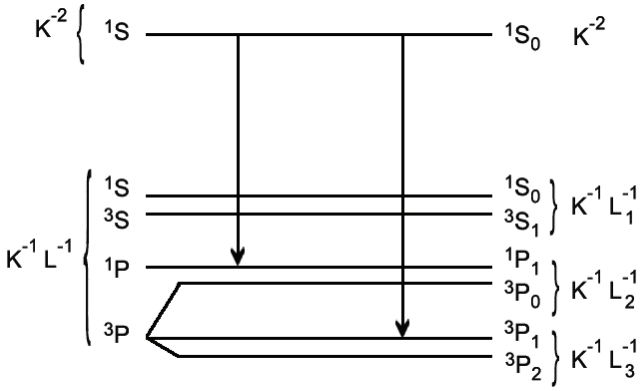

Fig. 1: $K\alpha_1$ and $K\alpha_2$ hypersatellite transitions.

Both $K\alpha_1$ ($1s^{-1} \rightarrow 2p^{-1}_{3/2}$) and $K\alpha_2$ ($1s^{-1} \rightarrow 2p^{-1}_{1/2}$) are electric dipolar transitions allowed in the LS, intermediate and jj coupling schemes, which hold, respectively, for low-Z, mid-Z and high-Z elements, and the intensity ratio of the $K\alpha_1$ to $K\alpha_2$ diagram lines is almost a factor two throughout the periodic table. In the presence of a 1s spectator vacancy, the hypersatellite transition $K\alpha_1^h$ ($1s^{-2} \rightarrow 1s^{-1}2p^{-1}_{3/2}$) and $K\alpha_2^h$ ($1s^{-2} \rightarrow 1s^{-1}2p^{-1}_{1/2}$) depicted in Fig. 1 are electric dipolar transitions allowed in the jj coupling scheme, and the hypersatellite intensity ratio $I(K\alpha_1^h)/I(K\alpha_2^h)$ is again close to the factor two (not exactly two because of the importance of relativistic effects in heavy elements). The $K\alpha_1^h$ ($^1S_0 \rightarrow {}^3P_1$) transition is, however, forbidden in the LS coupling scheme because $\Delta S \neq 0$ and the transition is therefore not observed in light elements. Within the intermediate coupling scheme which prevails for mid-heavy elements, the $K\alpha_1^h$ transition is no more strictly forbidden and its intensity increases with Z. Actually, theoretical calculations of Chen et al. [32] have shown that the $I(K\alpha_1^h)/I(K\alpha_2^h)$ intensity ratio increases rapidly in the region $20<Z<56$ from the LS coupling limit of zero to the jj coupling limit of two. An overview of the experimental intensity ratios $I(K\alpha_1^h)/I(K\alpha_2^h)$ reported in the literature for elements ranging from Ti (Z=22) to Pb (Z=82) is given in Fig. 2.

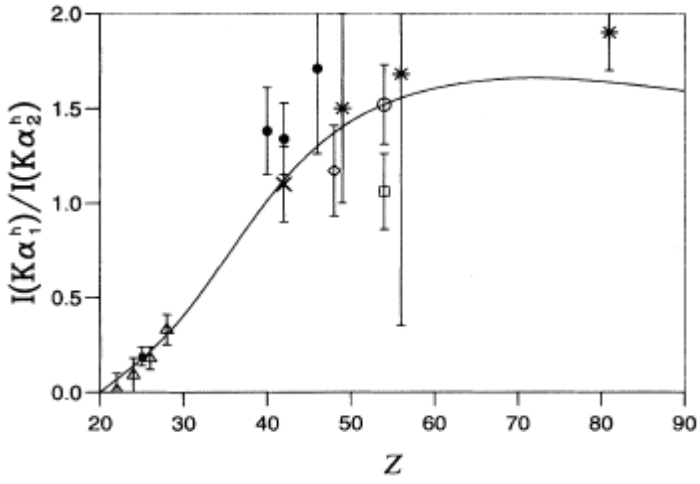

Fig. 2 (taken from Ref. [33]): $K\alpha_1^h$ to $K\alpha_2^h$ intensity ratios as a function of the atomic number Z. The solid line represents the results of DHS calculations by Chen et al. [32]. The symbols correspond to experimental values: Δ Ref. [34], □ Ref. [35], ○ Ref. [36], ■ Ref. [37], ◊ Ref. [38], × Ref. [39], * Ref. [20, 40], ● Ref. [33].

1.4.2 Energies

Relative to singly ionized atoms, the nuclear charge screening is reduced in doubly ionized atoms leading to an increase of the binding energy of the remaining electrons. Therefore the x-rays emitted by such states are shifted up in energy relative to the parent diagram lines. In general, the energy shift increases with the principal quantum number characterizing the electron undergoing the transition and decreases with the principal quantum number of the spectator vacancy. Therefore the most pronounced energy shift is that corresponding to K hypersatellite lines which result from the radiative decay of atoms doubly ionized in the 1s orbital.

1.4.3 Natural widths

The natural width of an x-ray transition is theoretically equal to the sum of the total widths of the initial and final atomic states. Assuming that the fluorescence yield for doubly ionized atoms is the same as for singly ionized atoms, Mossé et al. [41] suggested that the width of the initial state (K^{-2}) can be estimated to be $2\Gamma_K$ and that of the final state ($K^{-1}L^{-1}$), $\Gamma_K + \Gamma_L$. Therefore the linewidth of the $K\alpha^h$ (K^{-2} - $K^{-1}L^{-1}$) hypersatellite transition can be assumed to be $3\Gamma_K + \Gamma_L$, provided the fluorescence yields ω_K and ω_{KK} of the singly and doubly ionized atoms, respectively, are about the same.

1.4.4 Relative intensities

The intensity of the $K\alpha^h$ hypersatellite line depends on both the $K\alpha^h$ transition probability and double K-shell ionization cross section. As far as the $K\alpha^h$ is allowed, the $K\alpha^h$ transition probability is higher than that of the corresponding diagram line, since the de-excitation probability of the $1s^{-2}$ state is higher than that of the $1s^{-1}$ state. In case of collisions with heavy ions, where the cross sections to produce double K-shell ionization is large the intensity of the $K\alpha^h$ line is indeed high and can even be higher than that of the parent diagram line. In contrast to that, in photo-ionization, where the probability to produce double 1s vacancies is weak, the intensity of the $K\alpha^h$ hypersatellite is two orders of magnitude lower than that of the corresponding diagram line in the case of He, and becomes even weaker for heavier elements since the shake probability decreases with Z^{-2} [42].

1.5 Content of the present work

The present study reports on Al hypersatellite measurements performed by means of high-resolution, using synchrotron radiation and electrons for the production of the double 1s vacancies. In both series of measurements, the hypersatellites were observed at different beam energies ranging from the threshold energy for the double 1s ionization (about 3.1 keV) up to 5.5 keV for synchrotron radiation and 20 keV for electrons. The measurements performed with synchrotron radiation are presented in Chap. 2, those performed with the electrons in Chap. 3. In both chapters, first a brief description of the experimental setup is given, then the methods employed to correct and analyse the measured data are explained, and finally the results obtained for the energy and line width of the $K\alpha^h$ hypersatellite as well as for the ratio of the double to single K-shell ionization cross sections are presented. In Chap. IV, the $K\alpha^h$ energies and line widths obtained in the synchrotron radiation and electron measurements, respectively, are compared with the few values reported in the literature and a detailed comparison between the ratios of the double to single K-shell ionization cross sections in photon and electron impactis prensented. Concluding remarks and further perspectives are presented in Chap. 5.

Chapter 2

Measurements with synchrotron radiation

2.1. Experiment

2.1.1 Beam line setup

In order to study the evolution of the Al photo-excited Kα hypersatellite spectrum as a function of the incoming photon energy, monochromatic synchrotron radiation beams with energies ranging between 3122 eV and 5451 eV were employed. The experiment was performed at the x-ray microscopy beam line ID21 at the European Synchrotron Radiation Facility (ESRF), in Grenoble, France. The von Hamos crystal spectrometer of Fribourg was installed in the main experimental hutch of ID21, downstream to the scanning transmission x-ray microscope (STXM) chamber to which it was connected through a 180 cm long evacuated pipe (Fig. 3). On the spectrometer side the pipe was closed with a 25 μm thick Kapton^{TM} window in order to permit an access to the spectrometer chamber without degrading the high vacuum in the beam line. The white x-ray beam provided by an undulator was monochromatized with a double Ni/B4C multilayer. By using a pinhole installed in the STXM chamber, a beam spot of about 1 mm in diameter was obtained on the target. The number of photons impinging on the target was typically 1-2· 10^{12} photons/sec. Rejection of upper harmonics was realized using a Si-based Ni coated mirror. The energy calibration of the monochromator was done by measuring with a photodiode the K absorption edges of V, Ti, Ca and S.

2.1.2 Von Hamos setup

The spectra were observed with the high resolution reflection-type von Hamos crystal spectrometer described in the first part of this thesis. The target consisted in a 99.1% pure metallic aluminium foil. In order to minimize the self-absorption of the hypersatellite x-rays in the sample, a target thickness of 1 μm was chosen. The target was tilted to 30° relative to the direction of the incident photon beam. A slit width of 0.2 mm was used as the best

compromise between an acceptable energy resolution and high enough luminosity, two key parameters for the measurements of the Al Kα hypersatellites. The emitted fluorescence x rays were reflected in first order by an ADP (Ammonium dihydrogen phosphate) (101) crystal (2d = 10.648 Å) and then detected by a 26.8 mm long x 8 mm high back-illuminated CCD (charge coupled device), having a pixel size of 20 x 20 μm^2. The CCD was cooled down thermoelectrically to –50°C.

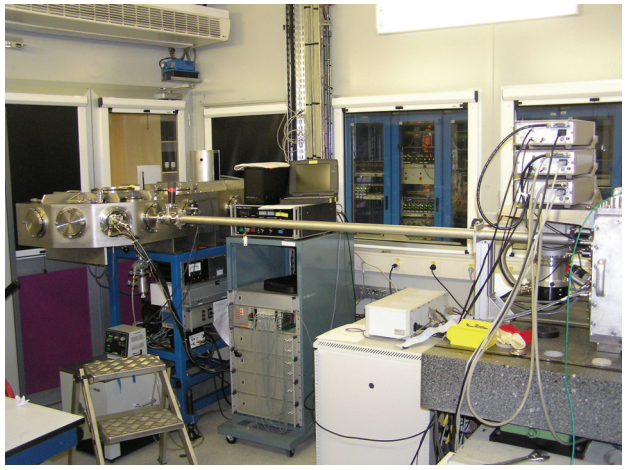

Fig. 3: Photograph of the von Hamos spectrometer as installed at the ID21 beam line.

2.1.3 Method of data acquisition

The diagram and hypersatellite x-ray spectra were observed at twelve different photon energies, namely at 3122 eV, 3186 eV, 3235 eV, 3318 eV, 3400 eV, 3507 eV, 3742 eV, 3972 eV, 4380 eV, 4786 eV, 5120 eV and 5451 eV. For the measurements of the $K\alpha_{1,2}$ diagram transitions, an acquisition time of 1 sec. per image was used. To avoid multiple hit events on the CCD camera, the beam intensity was attenuated by inserting a 10 μm thick Al absorber in the beam upstream to the target. As the double 1s photo-ionization cross section is weak and because, in addition, for aluminium the Kα hypersatellite transitions lie above the K-edge, which results in an increased self-absorption of the $K\alpha^h$ in the target, longer acquisition times of 10 sec. per image were chosen for the measurements of the hypersatellite spectra. In order to check the reproducibility of the measurements and the stability of the experimental setup, for each beam energy the hypersatellite spectra were observed in several short successive measurements of typically 200 images. Before each new short measurement the beam intensity was determined with a photodiode and the $K\alpha_{1,2}$ diagram lines measured with the crystal spectrometer. This procedure permitted us to survey the stability of the beam intensity and

beam spot profile on the target. If necessary, the hypersatellite spectra were then corrected off-line for the observed fluctuations of the beam intensity and beam spot profile.

2.2. Data analysis

2.2.1 Beam profile correction

In the modified von Hamos slit-geometry employed in these measurements, the target is viewed by the crystal through a narrow slit placed between the target and the crystal. As mentioned before, a slit width of 0.2 mm was used, whereas the size of the beam spot on the target was about 1 mm. As a consequence, if the beam intensity is inhomogeneous along the direction parallel to the dispersion axis of the spectrometer, the shapes of the measured spectra may be affected by the intensity profile of the incident photon beam.

During the experiment, the intensity of the synchrotron radiation beam and the position of the latter on the target were found to be quite stable. However, the intensity profile was somewhat unsteady, especially when tuning the monochromator to a new beam energy. For this reason, after each new monochromator setup the profile of the beam intensity was measured. Profile measurements were also performed whenever a change of the intensity was observed in the periodically performed Kα measurements.

To determine the beam intensity profile, we simply measured the Kα diagram line for different positions of the target along an axis parallel to the synchrotron radiation beam direction. As the crystal and the CCD positions were kept fixed in these measurements, the variation of the Kα diagram line intensity as a function of the target position reflects the horizontal distribution of the beam intensity on the target. An example of such a beam profile

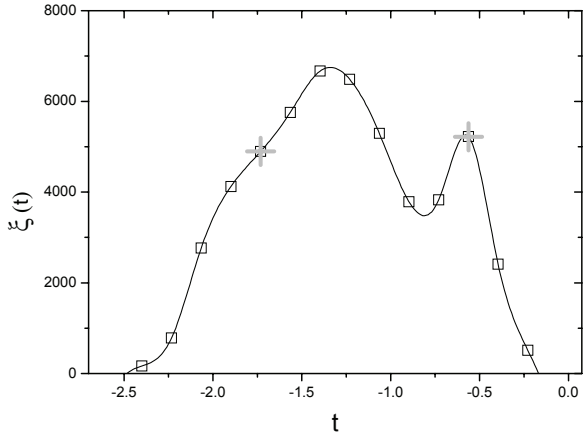

Fig. 4: Example of a beam intensity profile. The positions t are given in mm. The symbols + indicate the extreme positions on the target seen by the crystal through the slit.

is shown in Fig. 4. The variable t corresponds to the position along the target width, the origin t = 0 being defined by the middle of the target. In the example depicted in Fig. 4, one sees that the profile is not rectangular, i.e., the beam intensity is not homogeneous in the transverse direction. One sees also that, for this particular measurement, the beam position was shifted to the left of the target by about 1 mm. For each profile, the measured points were fitted with an interpolation function $\xi(t)$ which computes a cubic polynomial between each three successive points so that the first and second derivatives of the function are continuous across each point.

A dedicated program was written to compute the beam profile correction factor for each CCD column. The Kα hypersatellite spectrum measured at a beam energy of 4380 eV and the corresponding spectrum corrected for the beam profile represented in Fig. 4 are shown for illustration in Fig. 5. Generally, for all measured spectra we have found that the beam profile corrections were about 7% for the $K\alpha^h$ intensities and about 2% for the $K\alpha^h$ line widths.

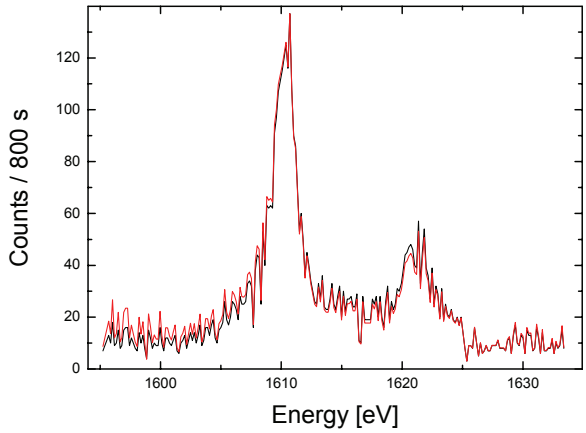

Fig. 5: Al $K\alpha^h$ spectrum measured at a beam energy of 4380 eV (black line) and the corresponding corrected spectrum (red line).

2.2.2 Intensity normalisation

Since the intensity measured with the photodiode inserted into the beam corresponds to the total number of photons impinging on the target and not to the number of photons producing the fluorescence x rays measured with the spectrometer operated in the slit geometry, for each measured spectrum, the intensity of the latter was corrected according to the following normalized number of photons N:

$$N = N_{ph} \frac{Ix}{Itot} \qquad (1)$$

Where N_{Ph} represents the number of photons measured with the photodiode, *Itot* the integral of the function $\xi(t)$ over the interval of t for which a non-vanishing intensity was observed, and *Ix* the integral of the function $\xi(t)$ over the interval corresponding to the extreme positions on the target seen by the crystal through the slit (see Fig. 4).

2.2.3 Self absorption correction

To account for the self absorption in the target, the measured Kα and Kα^h spectra were corrected by multiplying the fitted intensities with the following correction factor:

$$F_{corr,K\alpha,k\alpha h} = \frac{h(\mu_{Ebeam}/cos(\varphi) + \mu_{E(K\alpha),E(K\alpha h)}/sin(\varphi+\theta))}{1-exp(-h(\mu_{Ebeam}/cos(\varphi) + \mu_{E(K\alpha),E(K\alpha h)}/sin(\varphi+\theta)))} \qquad (2)$$

In (2), μ_{Ebeam} and $\mu_{E(K\alpha),E(K\alpha h)}$ represent the absorption coefficients of Al for the incident photons (energy E_{Beam}), respectively for the diagram and hypersatellite fluorescence x-rays (energies $E_{K\alpha}$ and $E_{K\alpha h}$), h stands for the target thickness, θ is the Bragg angle and φ the angle between the normal to the target and the beam direction.

The obtained correction factors are given in Table 1. They are bigger for the hypersatellite transition because the latter (E=1610 eV) lies above the K-absorption edge of Al (1560 eV). Note that the important quantity is the hypersatellite to diagram line intensity ratio for which the correction factor is given by $F_{corr,K\alpha h}$: $F_{corr,K\alpha}$. At the lowest beam energy the correction factor for the hypersatellite to diagram line intensity ratio amounts to 1.90:1.27=1.50, a value which is still reasonable, mainly because of the small thickness (1 μm) chosen for the employed target. For a 10 μm thick target, the correction factor for the intensity ratio would have been 14.2:5.04=2.81, i.e. significantly bigger.

Beam energy [eV]	$F_{corr,K\alpha}$	$F_{corr,K\alpha h}$
3122	1.27	1.90
3186	1.25	1.89
3235	1.24	1.88
3318	1.23	1.86
3400	1.22	1.85
3507	1.21	1.83
3742	1.18	1.80
3972	1.16	1.77
4380	1.14	1.74
4786	1.12	1.72
5120	1.11	1.70
5451	1.10	1.69

Table 1 : Kα and Kα^h self absorption correction factors for the photon beam energies used in the present experiment.

2.2.4 Energy calibration and spectrometer resolution

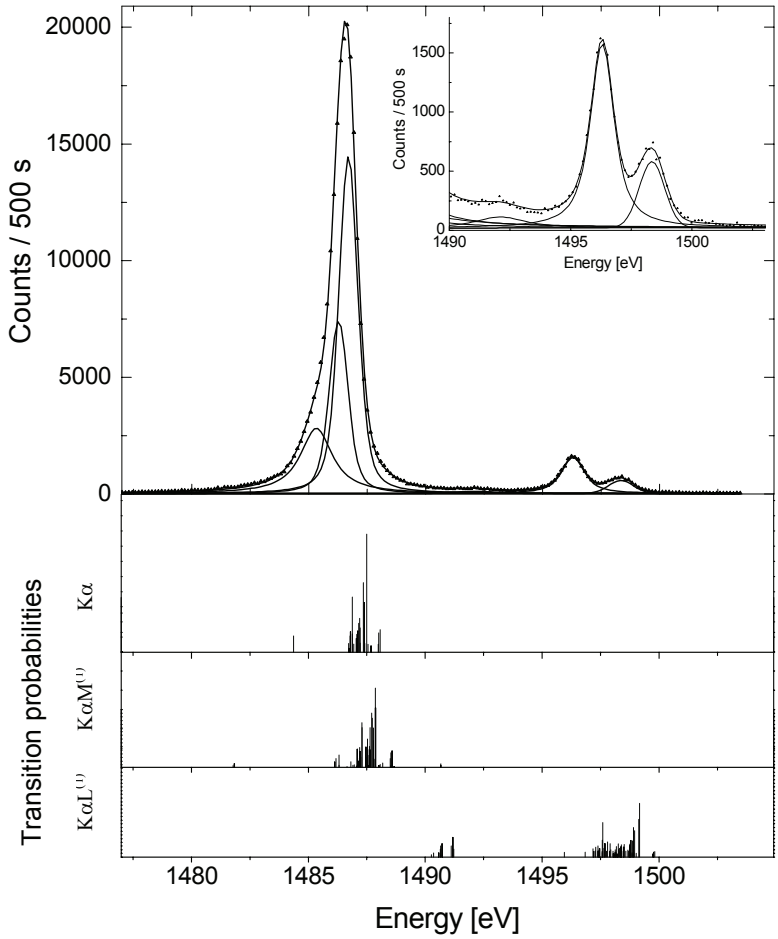

Fig. 6: Aluminium $K\alpha_{1,2}$ spectrum recorded at 4786 eV and the corresponding MCDF calculations taken from ref [44]. The KαL satellite structure is shown enlarged in the inset. The dots correspond to the experimental data, and the solid line to the least squares fit.

The energy calibration of the spectra was performed by measuring the $K\alpha_{1,2}$ diagram lines of Al and Si and by assigning to these measured lines the corresponding transition energies taken from Ref. [43]. For illustration, a typical Al $K\alpha_{1,2}$ spectrum and the corresponding MCDF calculations based on the GRASP code [44] are shown in Fig. 6. The first group of lines corresponds principally to the $K\alpha_1$ and $K\alpha_2$ diagram lines. The shoulder appearing around 1484 eV is due to the open valence subshell in the ground state, and the structure around 1497 eV, shown enlarged in the inset, corresponds to the KαL satellites lines. The spectrum was fitted by means of a least squares fitting program, employing Voigt functions for all observed transitions. Voigt functions were used because they correspond to the convolution

of the Lorentzian and Gaussian functions which represent the natural line shape of the transitions and the instrumental response of the spectrometer, respectively. The energy difference $E(K\alpha_1)$-$E(K\alpha_2)$ and the Lorentzian widths were kept fixed at the values quoted in Refs. [43] and [45], respectively. From the fit, a Gaussian width of 0.32 eV, which corresponds to the spectrometer resolution for the energy of the Al Kα line (1487 eV), was found.

In the von Hamos geometry, the experimental resolution is a function of the x-ray energy. The $L\beta_1$ transition of silver appears in second order of reflection at about the same Bragg angle as the Al $K\alpha^h$ transition. However, since the natural width of this transition is only known with a precision of about 10% [45], we have renounced to use it to determine the instrumental broadening corresponding to the Al Kα hypersatellite. The latter was preferably determined by interpolation using the fitted Gaussian widths of the Al and Si $K\alpha_{1,2}$ diagram lines, whereas the Ag $L\beta_1$ transition was only used to cross-check the energy calibration of the spectrometer and probe the error on it. It was found that the difference between the Al $K\alpha^h$ hypersatellite energies obtained from the Al+Si $K\alpha_{1,2}$ calibration and the Ag $L\beta_1$ calibration were fully consistent, the difference being smaller than the uncertainties given by the fits for the two Al $K\alpha^h$ hypersatellite energies.

2.2.5 Overlap with the $K\beta L^{(2)}$ spectra

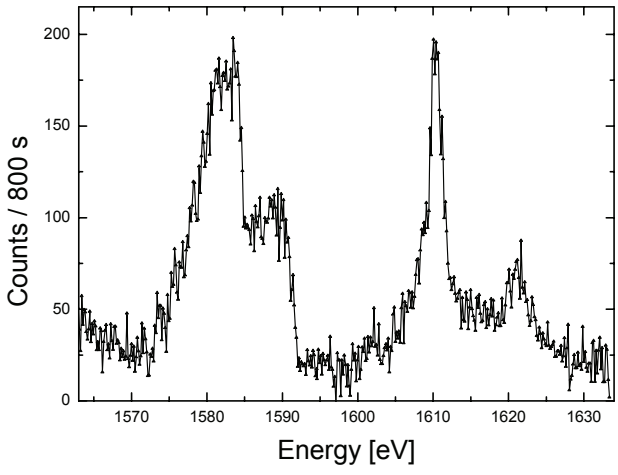

Fig. 7: Al $K\beta L^{(1)}$, $K\beta L^{(2)}$ and $K\alpha^h$ transitions measured at 4786 eV.

High-resolution was crucial for these measurements since the Al Kα hypersatellite is very close in energy to the $K\beta L^{(1)}$ satellite and completely overlapping with the $K\beta L^{(2)}$ satellite. Figure 7 shows the whole spectrum measured at a beam energy of 4786 eV. The first doublet corresponds to the components of the $K\beta L^{(1)}$ satellite structure, the third peak at about 1610

eV consists of the overlapping $K\beta L^{(2)}$ satellite and $K\alpha^h$ hypersatellite while the fourth one corresponds to the $K\alpha^h L^{(1)}$ transition, i.e., to the L satellite of the Kα hypersatellite.

In order to study the dependence on the beam energy of the Al Kα hypersatellite intensity, the shape and relative intensity of the overlapping $K\beta L^{(2)}$ satellite had first to be determined accurately. The measurement of the $K\beta L^{(2)}$ structure was performed at a beam energy of 3122 eV which is smaller than the threshold energy for the double K-shell ionization. The obtained spectrum is shown in Fig. 8. The $K\beta L^{(2)}$ spectrum has a complex shape, since the L spectator vacancies can be located in different subshells and different couplings are possible between the three holes in the initial and final excited states. Keski-Rahkonen et al. [46] reported that four $K\beta L^{(2)}$ satellites transitions are allowed in the LS coupling scheme. In our case, only three components were needed to fit the measured spectrum (see Fig. 8). The experimental energies obtained for the three components are compared to the corresponding theoretical predictions of Keski-Rahkonen in Table 2.

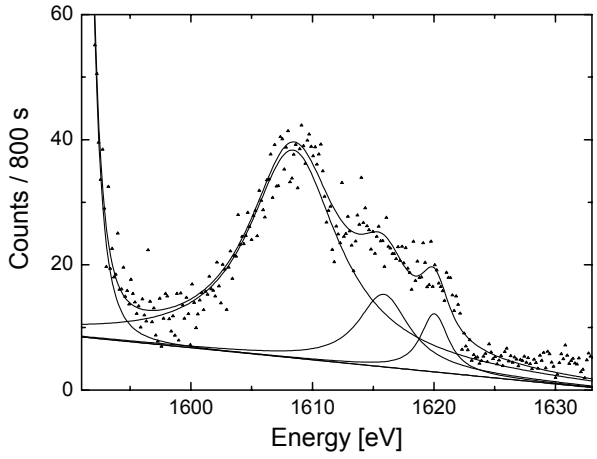

Fig. 8: Experimental (points) and fitted (lines) Al $K\beta L^{(2)}$ spectrum measured at 3122 eV.

		Energy [eV]	
Transition	Designation	Present	Ref. [46]
$K^{-1}L^{-2} \rightarrow L^{-2}M^{-1}$	$K\beta^{VII}$	1608.40(15)	1609.27(61)
	$K\beta^{VIII'}$	1615.86(29)	1613.47(61)
	$K\beta^{VIII'}$	—	1614.17(61)
	$K\beta^{VIII}$	1620.04(20)	1620.37(61)

Table. 2: $K\beta L^{(2)}$ transition energies. The values quoted in [46] by Keski- Rahkonen et al. are energy shifts relative to the parent diagram line. To be compared with present results, these energy shifts were added to the energy of the Kβ diagram line reported by Deslattes et al. [43].

2.2.6 Analysis of the Kα hypersatellite spectra

The beam energy of 3122 eV was the lowest one used in the present experiment. According to GRASP calculations, the threshold energy for producing three $K^{-1}L^{-2}$ vacancy states in Al is about 1834 eV, i.e., significantly lower than the beam energy employed to measure the shape of the pure $K\beta L^{(2)}$ satellite. It can thus be expected that the shape of the $K\beta L^{(2)}$ satellite remains the same at higher beam energies. A similar conclusion was drawn by Deutsch and coworkers [47] for the $K\alpha_{3,4}$ satellite spectrum of Cu. They found indeed that the shape of the spectrum was varying with the incident photon energy within an energy range of about 50 eV above the threshold, and then remained unchanged for higher incident photon energies. They explained the change of the satellite spectrum shape near the threshold region by the variation of the relative intensities of the individual satellite components whose threshold energies are slightly different.

As the $K\beta L^{(2)}$ to Kβ intensity ratio should be constant for beam energies far above the threshold and the absolute intensity of the Kβ transition is proportional to the cross section σ_K for a single 1s ionization, the intensity of the $K\beta L^{(2)}$ satellite measured at higher beam energies can be determined by multiplying the satellite intensity measured at 3122 eV by the cross section ratio $\sigma_K(E_{Beam})/\sigma_K(3122\ eV)$. The fitted $K\alpha^h$ spectrum recorded at 4786 eV is shown in Fig. 10. The $K\beta L^{(2)}$ structure was reproduced by three Voigtian functions, whose centers and line widths were kept fixed at the values obtained from the fit of the spectrum measured at 3122 eV. The intensities of the three Voigtians were also kept fixed at the values obtained at 3122 eV multiplied by the intensity ratio $I[K\alpha(E_{Beam}=4786\ eV)]: I[K\alpha(E_{Beam}=3122\ eV)]$. The latter ratio which is equal to the 1s photo-ionization cross sections ratio was preferably chosen because it presents the advantage to have been determined with the same experimental conditions as the intensity of the $K\beta L^{(2)}$ satellite. To probe the goodness of this method, the fitted Kα diagram line intensities corresponding to the different beam energies used in this project are plotted in Fig. 9 together with the K-shell photoionization cross sections derived from the NIST Tables [48]. For the purpose of comparison, the cross sections were normalized beforehand to the measured x-ray yields, using for all energies the same normalization constant. As shown, a quite fair agreement is observed. To reproduce the $K\alpha^h$ hypersatellite and its L satellite, two additional Voigtians were included in the fit. Except the Gaussian widths which were fixed at the values corresponding to the instrumental resolution of the spectrometer, all other fitting parameters were let free. Due to the asymmetries on their low-energy sides, the two components of the $K\beta L^{(1)}$ satellite were found to be better reproduced by using Pearson functions. Actually, since these two transitions do not evince Lorentzian tails on their high-energy side, they should have only a tiny influence on the fit of the $K\alpha^h$

hypersatellite. To check this assumption, the Kα hypersatellite region above 1595 eV was re-analysed, without considering the $K\beta L^{(1)}$ transitions. The results given by the second fit were found to be fully consistent with those obtained from the fit of the whole spectrum, differences of 3.24 10^{-3} eV and 0.11 eV being observed between the two fits for the $K\alpha^h$ energy and natural line width, respectively. For this reason, for all other beam energies, only the region of the Kα hypersatellite was analysed.

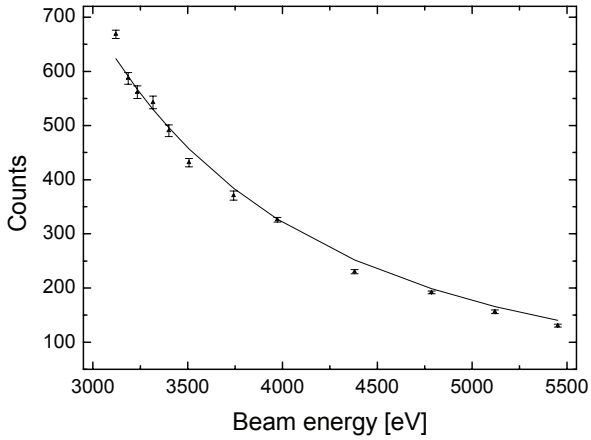

Fig. 9: Comparison between the Al $K\alpha_{1,2}$ intensities and the normalized single K-shell photo-ionization cross sections σ_K [48] for the photon beam energies used in the present project.

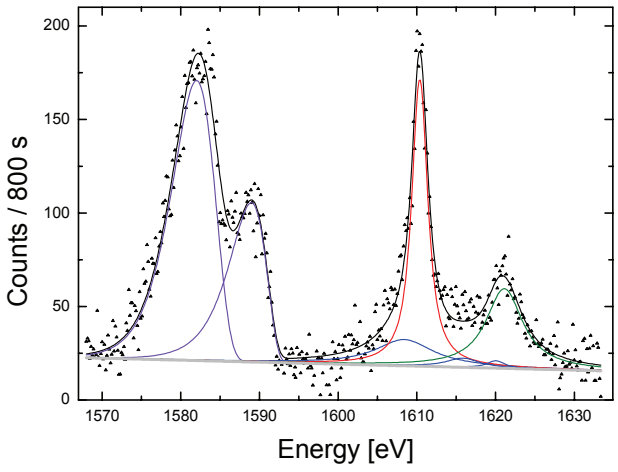

Fig. 10: Fit of the $K\beta L^{(1,2)}$ + $K\alpha^h$ x-ray spectrum of Al measured at a beam energy of 4786 eV. The triangles correspond to the measurement, the solid lines to the fitted components: $K\beta L^{(1)}$ (violet lines), $K\beta L^{(2)}$ (blue lines), $K\alpha^h$ (red line) and $K\alpha^h L^{(1)}$ (green line).

2.3 Results

In this Sect. only the main results and brief comments are presented. A more detailed discussion and a comparison with existing experimental and theoretical data as well as with the results obtained with electron beams will be given in Chap. 4. Furthermore, it can be reminded here that the obtained results concern only the $K\alpha_2^h$ hypersatellite ($^1S_0 \rightarrow {}^1P_1$ transition). The $K\alpha_1^h$ hypersatellite ($^1S_0 \rightarrow {}^3P_1$ transition), which is forbidden by the E1 selection rules in the LS coupling scheme, could not indeed be observed, even for beam energies far above the threshold energy for the double 1s photo-ionization.

In Figs. 11 and 12 we have plotted the $K\alpha_2$ hypersatellite energies and line widths obtained from the fits of the measured spectra. Results are given only for the nine highest beam energies since for the beam energies just above the threshold the hypersatellite yields were so small that the energy and line width of the hypersatellite had to be kept fixed in the analysis to fit its intensity. As shown, no dependence on the energy of the synchrotron radiation is observed for the hypersatellite energy nor for its line width.

For the energy of the $K\alpha_2^h$ hypersatellite, an average value of 1610.38 eV with a standard deviation of 0.05 eV was found. The $K\alpha_2^h$ energy shift relative to the parent $K\alpha_2$ diagram line (E=1486.29 eV [43]) amounts thus to 124.09 eV. This energy separation is about 14 times bigger than the one of the $K\alpha L^{(1)}$ satellite (about 9 eV, see Fig. 6).

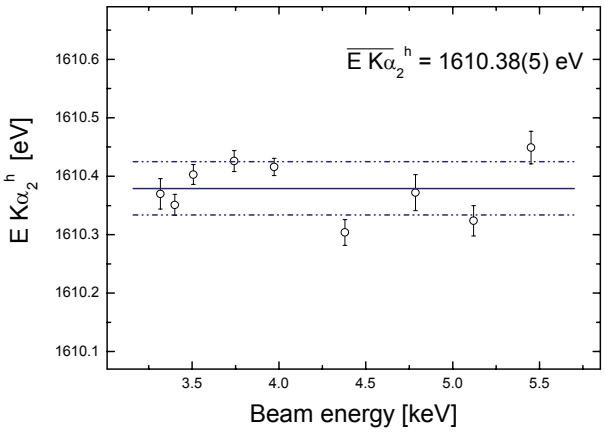

Fig. 11: $K\alpha_2^h$ hypersatellite energies as a function of the used photon beam energies. Indicated error corresponds to the standard deviation of the average value.

The average value found for the natural line width of the $K\alpha_2^h$ hypersatellite transition is 1.88 eV with a standard deviation of 0.17 eV. This value is about 4 times bigger than the

natural width of the Kα diagram transition ($\Gamma_{K\alpha}$=0.41 eV [45]), indicating that, as expected, the lifetime of double 1s vacancy states is much shorter than the one of single 1 s vacancy states.

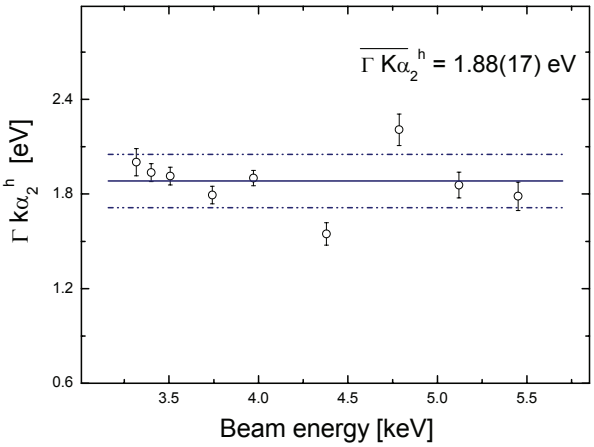

Fig. 12: $K\alpha_2^h$ hypersatellite line width as a function of the used photon beam energies. Indicated error corresponds to the standard deviation of the average value.

The obtained hypersatellite to diagram line intensity ratios $I(K\alpha^h)/I(K\alpha)$ and double 1s photo-ionization cross sections σ_{KK} are listed in Table 3 as a function of the photon beam energy. The cross sections σ_{KK} were computed from the measured intensity ratios $I(K\alpha^h)/I(K\alpha)$ and single K-shell photo-ionization cross sections σ_K deduced from the NIST Tables [48], using the following relation:

$$\sigma_{KK} = \frac{I(K\alpha^h)}{I(K\alpha)} \cdot \frac{\omega_K}{\omega_{KK}} \cdot \sigma_K \,. \qquad (3)$$

The fluorescence yields ω_K and ω_{KK} of the $1s^{-1}$ singly ionized and $1s^{-2}$ doubly ionized Al atoms were taken from the Ref. [49] .

Beam energy [keV]	$I(K\alpha^h)/(I(K\alpha)$	σ_{KK} [barn]
3.12	$7.54(3.26)\ 10^{-6}$	0.17
3.19	$3.60(46)\ 10^{-5}$	0.77
3.23	$3.41(43)\ 10^{-5}$	0.70
3.32	$4.62(13)\ 10^{-4}$	8.85
3.40	$7.46(19)\ 10^{-4}$	13.38
3.51	$9.79(22)\ 10^{-3}$	16.16
3.74	$1.15(3)\ 10^{-3}$	15.95
3.97	$1.42(3)\ 10^{-3}$	16.73
4.38[1]	-	-
4.79	$2.06(5)\ 10^{-3}$	14.83
5.12[1]	-	-
5.45	$2.22(7)\ 10^{-3}$	11.25

[1]For these energies the beam intensity monitoring system was not working properly so that the ratios $I(K\alpha^h)/I(K\alpha)$ and cross sections σ_{KK} could not be determined.

Table 3: Measured $I(K\alpha^h)/I(K\alpha)$ intensity ratios and double 1s photo-ionization cross sections σ_{KK} as a function of the incident photon energy.

Chapter 3

Measurements with electrons

3.1. Experiment

3.1.1 Experimental setup

The measurements of the Al Kα hypersatellites induced by electron impact were performed at the University of Fribourg. The setup of the von Hamos spectrometer was exactly the same as the one used for the synchrotron radiation measurements. A thermo-ionic electron gun (*Kimball Physics, gun type*) equipped with electrostatic focusing and deflection electrodes and a tantalum disc cathode allowing beam intensities up to 1 mA was employed. With this cathode, the electron gun can be operated safely at a pressure of about 10^{-6} mbar which corresponds quite well to the vacuum in the spectrometer chamber for standard operation. Accelerating voltage can be varied from 50 eV to 20 keV with a precision of 1 eV and an energy spread less than 0.4 eV. The beam current is independently adjustable from 1 μA to 1 mA and the spot size on the sample can be tuned from 1.5 mm to 25 mm. The power supply system offers a feedback stabilized emission current control option (ECC) to maintain a beam current stability of 0.1% per hour. The electron gun was mounted on the same beam port of the spectrometer chamber as the one used at the ESRF (Fig. 13). For all measurements, the Al target surface was perpendicular to the electron beam.

To reduce the background, a cylindrical collimator was installed between the electron gun and the target and the spectrometer slit was covered with a 25 μm thick Be foil (Fig. 14). Preliminary measurements performed without the collimator nor Be foil showed that the background was so high that it was completely hopeless to extract from it the weak hypersatellite signal. Another technical problem encountered at the beginning of the experiment was the accumulation of negative charges on the target, collimator and shielding around the target chamber. This charge accumulation resulted in a loss of intensity of the electron beam on the sample, loss which was increasing rapidly with time so that the fluorescence signal disappeared already a couple of minutes after having started the data acquisition. This problem could be solved by grounding properly the target, collimator and shielding.

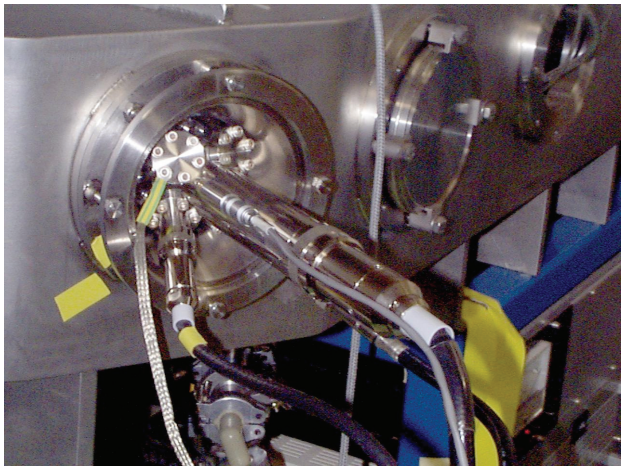

Fig. 13: The electron gun as mounted on one of the beam ports of the vacuum chamber of the von Hamos spectrometer.

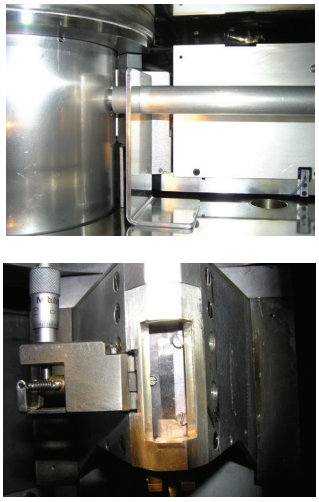

Fig. 14: Upper part: the cylindrical collimator. Lower part: the Be foil glued on the spectrometer slit.

Because electron-induced excitation of x-rays is not very efficient, large amounts of heat were produced in the target. First we tried to use an Al foil having the same thickness (1 μm) as the one employed for the synchrotron radiation measurements. It was found, however, that after a few minutes of irradiation, using a beam current of few hundreds of μA, the target part hit by the beam was completely melt (Fig. 15). Furthermore, as for electron energies above 5.4 keV, the penetration depth in Al is larger than 1 μm, some enhancement of the target x-ray fluorescence could be expected for all electron beam energies higher than 5.4 keV by using a target thickness bigger than 1 μm. For these reasons we have opted for a thicker Al foil of 10 μm. The latter was found to resist quite well to the heat load of the electron bombardment, even in the case of long term irradiation. On the other hand, as it was already mentioned by Mauron et al. [44], chemical reactions were observed in the target as a result of the electron irradiation. After a few hours of irradiation, a black dot coinciding in position and shape with the beam spot usually appeared on the surface of the target (Fig. 16). An electron microprobe analysis of this black dot showed that the latter consisted of carbon and oxygen originating probably from chemical reactions between the heated Al foil and some residual oil vapour in the spectrometer chamber. It was found that the intensity of the target x-ray emission decreases with time due to this burning effect. For that reason, a short measurement of the Kβ diagram line was performed periodically, and a new Al foil was installed whenever a change in the Kβ intensity was detected.

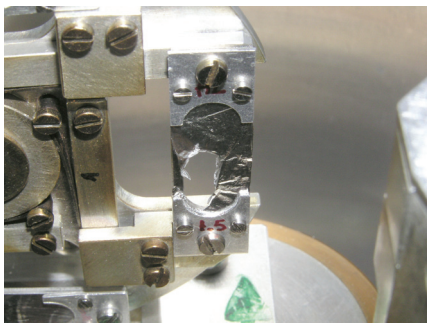

Fig. 15: The 1 μm Al target ''melted'' due to electron bombardment.

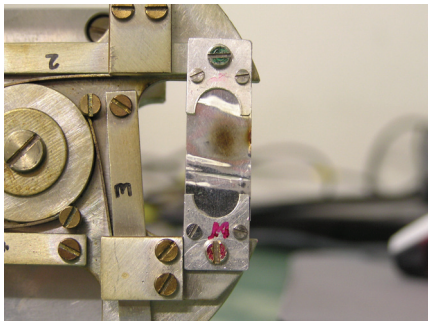

Fig. 16: A black dot usually appeared on the Al target surface after few hours of electron bombardment.

To illustrate the large amount of background produced when using electrons as projectiles, background which made the measurements of the weak Al Kα hypersatellites with electrons much more difficult than with photons, we have plotted in Fig. 17 the Al $K\alpha^h$ spectra induced by electrons and synchrotron radiation at the energy corresponding for each projectile type to the maximum of the double 1s ionization cross section. One sees that for electrons the hypersatellite transition is much weaker and the background about 20 times higher.

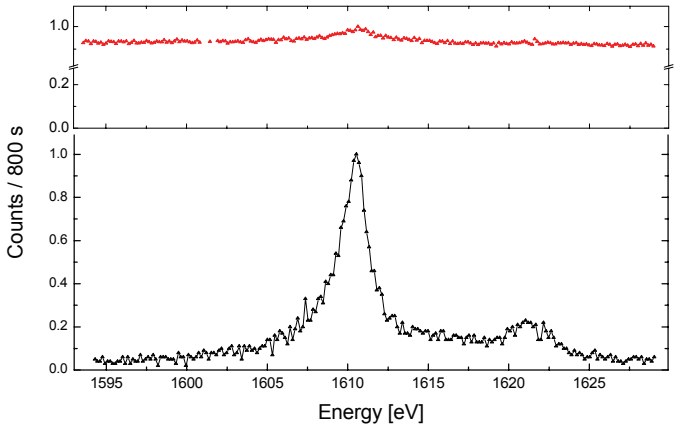

Fig. 17: Aluminium Kα hypersatellites produced by 3.97 keV photons (black line) and 15 keV electrons (red line).

3.1.2 Method of data acquisition

The Al spectra were measured with thirteen different incident electron beam energies (4, 5, 6, 7, 8, 9, 10, 11, 13, 15, 17, 18 and 20 keV). As for the synchrotron radiation measurements, the hypersatellite lines were measured with an exposure time of 10 sec., while the Kα diagram

lines were measured with an exposure time of 1 sec. For each beam energy, the hypersatellite data were collected in several successive measurements of typically 500 images. Before each new measurement, the beam profile was determined and a short measurement of the parent Kβ line was performed to check the stability of the electron beam intensity and reproducibility of the experimental setup. Depending on the electron energy, beam currents ranging between 140 and 600 μA were used. The beam current was chosen so that the power deposed in the target did not exceed 4 W. Actually, test measurements showed that the 10 μm thick Al foil started to melt for powers higher than 4 W. Furthermore, as the shape of the beam profile on the target was found to vary somewhat with the beam current, for each beam energy, the $K\alpha_{1,2}$ spectrum was measured with the same current as the one used for the corresponding $K\alpha^h$ spectrum. This resulted, however, in too big intensities on the CCD for the measurements of the intense $K\alpha_{1,2}$ diagram lines with the consequence of increasing strongly the number of multiple hit events. The problem was solved by installing an absorber (125μm Be + 10 μm Al) between the sample and the crystal that diminished the $K\alpha_{1,2}$ intensity by a factor of about 4700. As for the synchrotron radiation experiment, the spectrometer energy calibration was determined from measurements of the $K\alpha_{1,2}$ lines of Al and Si.

3.2. Data analysis

3.2.1 Beam profile correction and data normalisation

A home made beam position monitoring system was used to align the electron gun and to set the proper X and Y deflection parameters. The beam position monitoring system (Fig. 18) consists of three superimposed copper plates located in the front plane of the monitor with a 5 mm in diameter hole bored in the center of the middle plate. In the rear plane of the device, a fourth copper electrode with a smaller hole can be inserted. Depending on the beam spot diameter which has to be obtained, rear electrodes with different hole diameters down to 0.4 mm can be used. All electrodes are electrically isolated and connected to four independent current amplifiers. The beam position and beam spot size can then be adjusted, using the deflection and focusing electrodes of the electron gun, by observing the variation of the four currents. These beam optimizations were performed by installing the beam monitor at the same positions as the target positions at which the measurements of the x rays of interest were then performed. For this project, beams with rather large spot sizes (2-3 mm in diameter) were employed in order to keep the beam profile corrections at values as small as possible. Actually, it was found that, using beams with broad profiles, the corrections on the $K\alpha^h$ intensities were smaller than 4%, those on the $K\alpha^h$ line widths smaller than 1%. A typical

example of the employed beam profiles is depicted in Fig. 19. The measured x-ray intensities were normalized, using equation (1) in which the number of incident photons *Nph* was replaced by the number of incident electrons $N_e = I/e$, where I stands for the beam emission current. The background was subtracted from the spectra before correcting them for the beam profile.

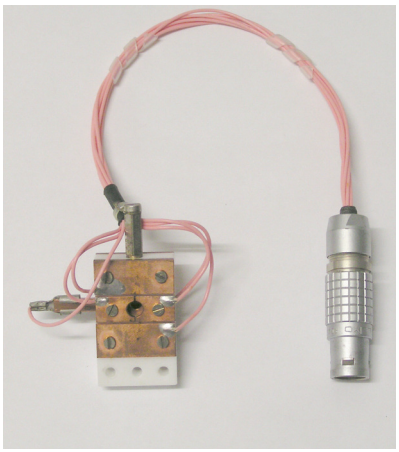

Fig. 18: The electron beam position monitoring device.

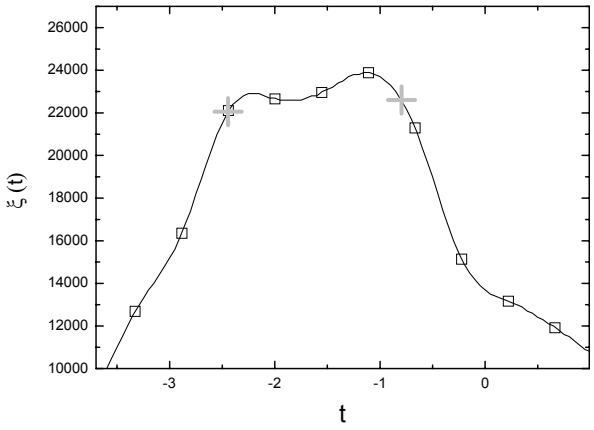

Fig. 19: Typical example of the electron beam profiles used in the present experiment. The zero position on the t-axis corresponds to the middle of the target. The + symbols indicate the extreme positions on the target seen by the crystal through the slit.

3.2.2 Average energy calculations

The intensity of a collimated photon beam decreases when the photons are travelling through matter, the photon energy remaining, however, unchanged. In contrast to that, electrons, as a result of multiple inelastic scattering processes with atomic electrons and nuclei, loose part of their energy but the intensity of the beam remains the same, at least as long as the target thickness is smaller than the maximum penetration range of the electrons. As in our experiment, thick targets (~2.7 mg/cm^2) were used, the observed x-ray yields should be related to the average energy of the electrons which is given by the following formula [44]:

$$\overline{E}_{K,KK} = \frac{\int_0^{h_{K,KK}} E(x)\cdot\sigma_{K,KK}[E(x)]\cdot exp\left[-\mu\frac{x}{sin(\theta)}\right]dx}{\int_0^{h_{K,KK}} \sigma_{K,KK}[E(x)]\cdot exp\left[-\mu\frac{x}{sin(\theta)}\right]dx}, \qquad (4)$$

where $\overline{E}_K$ and $\overline{E}_{KK}$ represent the average energies of the electrons that produce in the target single and double K vacancies, respectively, σ_K and σ_{KK} the corresponding cross sections, μ

and θ the mass attenuation coefficient and Bragg angle for the considered x-ray transition, and x the projectile penetration depth projected on the axis perpendicular to the target surface. The coefficients μ were taken from Ref. [50]. The stopping power of the electrons in the target is defined by:

$$\frac{dE}{dx} = -c \cdot E^{-\nu} \Rightarrow E^{\nu} dE = -c \cdot dx \,. \qquad (5)$$

The coefficients c and ν were derived from the stopping power values quoted in Ref. [51]. The function $E(x)$ was found from the integration of Eq. (5):

$$E(x) = \left[E_e^{\nu+1} - (\nu+1) \cdot c \cdot x\right]^{1/(\nu+1)}, \qquad (6)$$

where E_e stands for the energy of the incoming electrons. The distances h_K and h_{KK} occurring in Eq. (4) represent the penetration depths at which the electron energy is equal to the threshold energy $E_{thr,K}$ for a single 1s ionization, respectively the threshold energy $E_{thr,KK}$ for a double 1s ionization. These distances can be deduced from Eq. (6):

$$h_{K,KK} = \frac{E_e^{\nu+1} - E_{thr,K,KK}^{\nu+1}}{(\nu+1) \cdot c} \,. \qquad (7)$$

3.2.3 Analysis of the Kα hypersatellite spectra

A thin oxide layer is formed on the surface of pure aluminium foils when the latter are exposed to air. Depending on the surface treatment of the foils, the oxide layer thickness ranges from a few nm to a few hundreds of nm. For the lowest beam energy used in this experiment (E_e = 4 keV), a penetration depth h_{KK} = 0.08 μm is found from (7). Therefore these low-energy electrons interact almost exclusively with the molecules of the aluminium oxide layer and not with the Al atoms. The x-ray spectrum measured at 4 keV (Fig. 20) corresponds

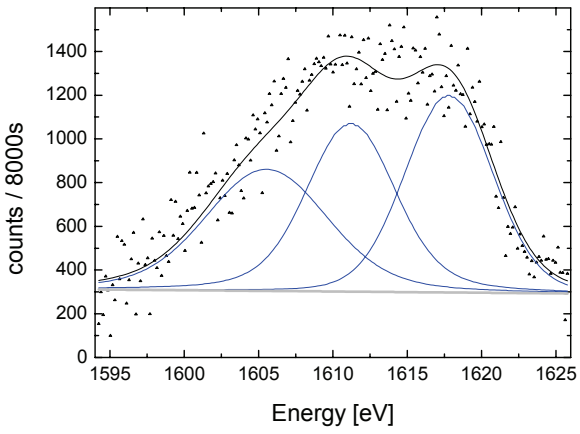

Fig. 20: Aluminium oxide spectrum measured with 4 keV electrons.

therefore to transitions in the aluminium oxide layer. The spectrum was fitted with three Voigt functions. All parameters were let free in the fit.

When the beam energy increases, the electrons can penetrate more deeply in the target. X rays of pure Al become then more and more intense and start to prevail over those of Al oxide. Fig. 21a shows the Kα hypersatellite spectrum measured at E_e = 6 keV. The latter was analysed in the following way: three Voigt functions were used to fit the Al oxide structure. Except the intensities of these three Voigtians and the linear background, all other fitting parameters were set at the same values as the ones obtained from the fit of the Al oxide spectrum measured at E_e = 4 keV, the intensity ratios of the three Voigtians included. Three Voigt functions were added to fit the $K\beta L^{(2)}$ structure. The energies and widths of the three peaks and the relative intensities of the two weakest peaks relative to the strongest one at 1608.4 eV were kept fixed in the fit at the values found for the photo-induced $K\beta L^{(2)}$ spectrum measured with the 3122 eV photon beam. One additional Voigtian was used for the $K\alpha^h$ hypersatellite. The Gaussian width of the latter was fixed at the known instrumental response (0.325 eV), whereas all other fitting parameters were let free.

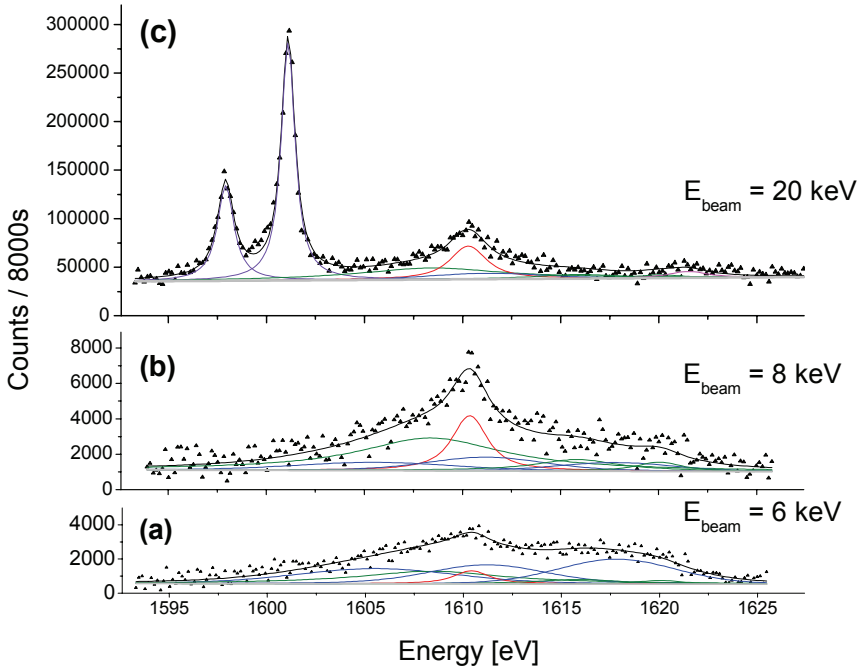

Fig. 21: Al $K\alpha^h$ spectra for three different electron beam energies. The triangles correspond to the experimental points, the solid lines to the fits: sum spectra (black lines), Al oxide transitions (blue lines), $K\beta L^{(2)}$ satellites (green lines), $K\alpha^h$ hypersatellites (red lines) and linear backgrounds (grey lines). The two strong lines occurring in the spectrum acquired at 20 keV correspond to the $K\alpha_{1,2}$ transitions of Fe (for details, see text).

The same fitting procedure was adopted to fit the Kα hypersatellite spectra recorded at higher electron energies except that from 11 keV and above an additional Voigtian had to be introduced in the fits for the $K\alpha^h L^{(1)}$ line. Spectra recorded at 8 keV and 20 keV are shown in Fig. 21b and 21c, respectively. The two peaks seen respectively at 1598 eV and 1601 eV correspond to the fourth order reflection of the $K\alpha_2$ (E = 6391 eV) and $K\alpha_1$ (E = 6404 eV) x-ray lines of iron. The latter originate from trace impurities of this metal in the Al target. The purity of the 10 μm Al foils used in the electron project was 99.0%, i.e., about the same as the one of the 1 μm foil (99.1%) employed in the measurements with synchrotron radiation. In the latter, the Fe K x rays were, however, not observed because the highest energy (5451 eV) of the employed photon beams was still below the K edge of iron (7112 eV). According to the data sheet of the Al foils, the iron impurities should be smaller than 7000 ppm. It is thus somewhat surprising that these Fe K x-ray lines reflected in the fourth order of reflection (4^{th} order reflections are much weaker than 1st order ones) have an intensity significantly higher than that of the Al $K\alpha^h$ hypersatellite! This shows that our high-resolution measurements of the electron-induced Al hypersatellites represented a real experimental challenge.

The Al Kα diagram and hypersatellite lines were corrected for the self-absorption in the target by dividing the fitted intensities by the following correction factors:

$$F_{corr,K,KK} = \frac{\int_0^{h_{K,KK}} \sigma_{K,KK}[E(x)] exp(-\mu \cdot \frac{x}{\sin\theta}) dx}{\int_0^{h_{K,KK}} \sigma_{K,KK}[E(x)] dx}. \qquad (8)$$

To compute the two integrals appearing in both formulas (4) and (8), we need to know the functions $\sigma_K(E)$ and $\sigma_{KK}(E)$. The function $\sigma_K(E)$ was determined by fitting the experimental cross sections reported in [52]. Fortunately these experimental data cover the whole range of electron energies used in our study. The so-determined function $\sigma_K(E)$ (Fig. 22) allowed us to compute the average energies $\overline{E}_K$ and the self absorption factor $F_{corr,K}$. The obtained values are listed in Table 4.

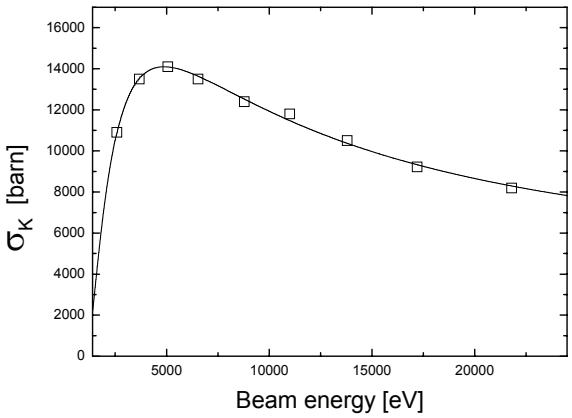

Fig. 22: Electron-induced single K-shell ionization cross section σ_K as a function of the electron energy.

The average energies $\overline{E}_{KK}$ and correction factors $F_{corr,KK}$ were computed iteratively, using in the first iteration the approximations $\overline{E}^{(1)}_{KK\,i} \cong \overline{E}^{(1)}_{K_i}$ and $F^{(1)}_{corr,KK_i} \cong F^{(1)}_{corr,K_i}$. The cross section $\sigma^{(n)}_{KK_i}$ corresponding to the *n*th iteration was obtained as follows:

$$\sigma^{(n)}_{KK_i} = \frac{X_i(K\alpha^h)}{X_i(K\alpha)} \frac{\omega_K}{\omega_{KK}} \sigma_{K_i}(\overline{E}^{(n-1)}_{KK_i}), \qquad (9)$$

where $X_i(K\alpha^h)$ stands for the Kα hypersatellite intensity measured at the beam energy E_{e_i} and corrected with the self absorption coefficient $F^{(n-1)}_{corr,KK_i}$, $X_i(K\alpha)$ for the diagram line intensity corresponding to the average energy $\overline{E}^{(n-1)}_{KK_i}$ and corrected with the self absorption coefficient $F_{corr,Ki}$. The variation of the intensity of the Kα line corrected for the self absorption as a function of the average energy $\overline{E}_K$ could be well fitted using an exponential function (see Fig. 23). The x-ray yield $X_i(K\alpha)$ corresponding to the energy $\overline{E}^{(n-1)}_{KK_i}$ was computed using this exponential function.

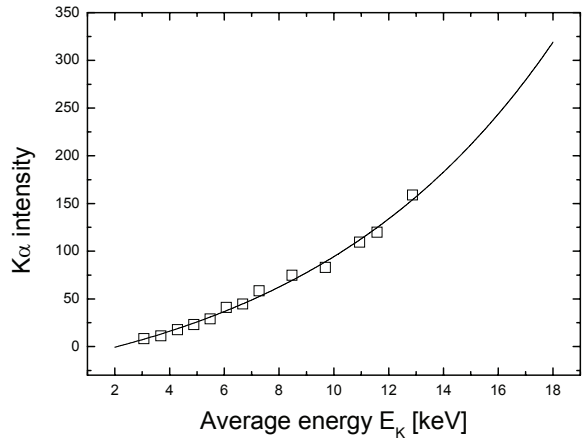

Fig. 23: Variation of the Al Kα intensity corrected for the self absorption in the target as a function of the electron average energy. The solid line represents a least-squares fit to the data using an exponential function.

The values obtained from Eq. (9) for the $\sigma_{KK_i}^{(n)}$ were fitted with an appropriate function $\sigma_{KK}^{(n)}(E)$ which permitted us to compute the energies $\overline{E}_{KK_i}^{(n)}$ and correction factors $F_{corr,KK_i}^{(n)}$, using Eqs. (4) and (8). The new values $\overline{E}_{KK_i}^{(n)}$ and $F_{corr,KK_i}^{(n)}$ were then introduced in Eq. (9) to obtain the $\sigma_{KK_i}^{(n+1)}$, from which the function $\sigma_{KK}^{(n+1)}(E)$ was determined leading to new $\overline{E}_{KK_i}^{(n+1)}$ and $F_{corr,KK_i}^{(n+1)}$, and so forth. The method was found to be self-consistent, i.e., after un certain number of iterations (12 in most cases) the average energies $\overline{E}_{KK_i}$, the correction factors F_{corr,KK_i} and so the double K-shell ionization cross sections σ_{KK_i} were found to remain unchanged. The final values of these parameters are listed in Table 4, whereas the evolution of the function $\sigma_{KK}^{(n)}(E)$ with the iteration number *n* is shown in Fig. 24.

HV [kV]	$\overline{E}_K$ [keV]	$\overline{E}_{KK}$ [keV]	$F_{corr,K}$	$F_{corr,KK}$	$\sigma_K(\overline{E}_{KK})$ [barn]	$\sigma_{KK}(\overline{E}_{KK})$ [barn]	$X(K\alpha^h) / X(K\alpha)$
4	3.07	3.76	0.99	0.96	1.36E+04	0.008	7.42E-07
5	3.68	4.57	0.98	0.92	1.41E+04	0.047	4.18E-06
6	4.29	5.38	0.97	0.87	1.40E+04	0.294	2.59E-05
7	4.89	6.18	0.96	0.81	1.38E+04	0.600	5.39 E-05
8	5.48	6.95	0.94	0.75	1.35E+04	0.654	6.03 E-05
9	6.08	7.71	0.93	0.67	1.31E+04	0.859	8.15 E-05
10	6.67	8.48	0.92	0.60	1.27E+04	0.955	9.34 E-05
11	7.27	9.29	0.90	0.53	1.23E+04	0.961	9.70 E-05
13	8.47	11.01	0.87	0.42	1.15E+04	1.039	1.12 E-04
15	9.69	12.86	0.83	0.32	1.07E+04	1.048	1.21 E-04
17	10.40	14.80	0.79	0.25	1.00E+04	0.956	1.18 E-04
18	11.57	15.79	0.78	0.22	9.72E+03	0.991	1.26 E-04
20	12.87	17.79	0.74	0.17	9.17E+03	0.893	1.21 E-04

Table 4: High voltage of the electron gun, average energies $\overline{E}_K$ and $\overline{E}_{KK}$ of the electrons producing a single, respectively double, K-shell ionization, self absorption correction factors for the measured Kα and $K\alpha^h$ lines, single and double K-shell ionization cross sections, and corrected $K\alpha^h$ to Kα intensity ratios.

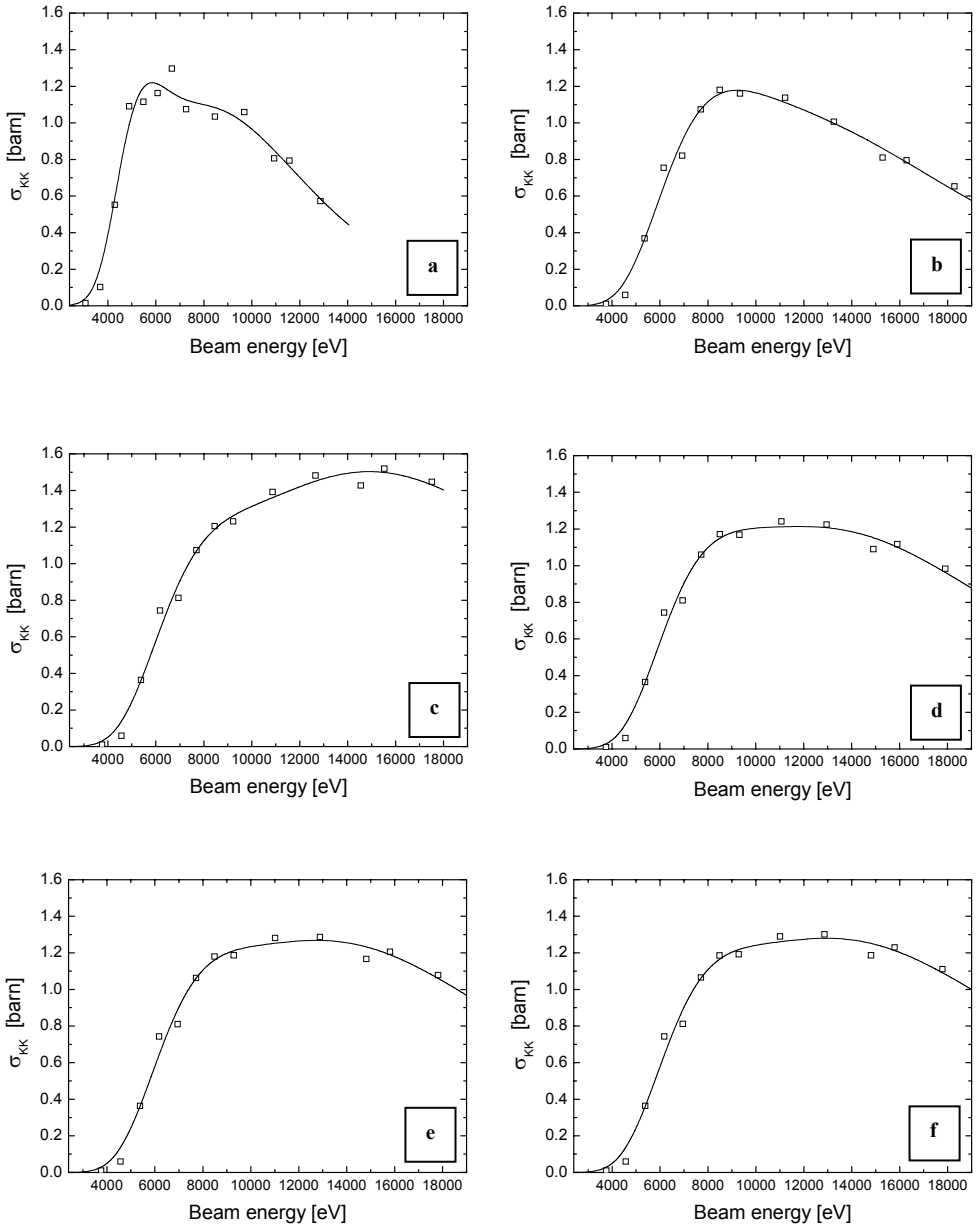

Fig. 24: Evolution of the function $\sigma_{KK}^{(n)}(E)$ with the iteration number n: (a) n = 1, (b) n = 3, (c) n = 4, (d) n = 5, (e) n = 7 and (e) n = 12 (final iteration). One can see that from n = 5 the function remains nearly the same.

3.3 Results

From these electron measurements we were able to determine the variation of the double K-shell ionization cross section as a function of the incoming electron energy (Fig. 24f), the energy and natural line width of the Al $K\alpha_2^h$ hypersatellite (Fig. 25 and Fig. 26) as well as the $K\alpha_2^h$ to $K\alpha$ intensity ratio for thirteen electron energies (Table 4 and Fig. 27). A discussion of these results and a comparison with the photon results and other available experimental and theoretical data is presented in the next chapter.

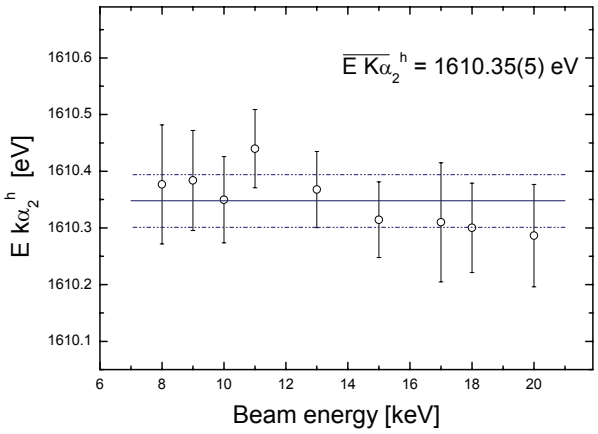

Fig. 25: $K\alpha_2^h$ hypersatellite energy for the used electron beam energies. Indicated error corresponds to the standard deviation of the average value.

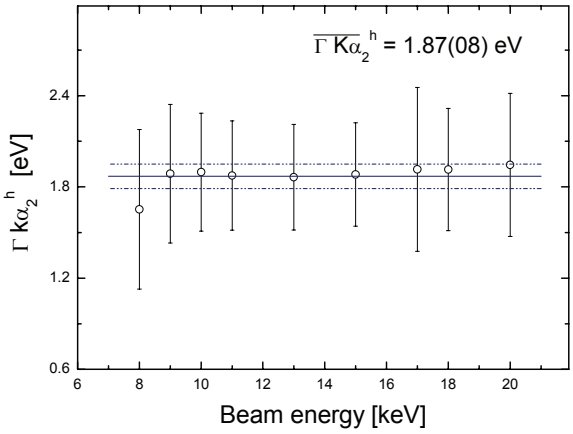

Fig. 26: $K\alpha_2^h$ hypersatellite line width for the used electron beam energies. The indicated error corresponds to the standard deviation of the average value.

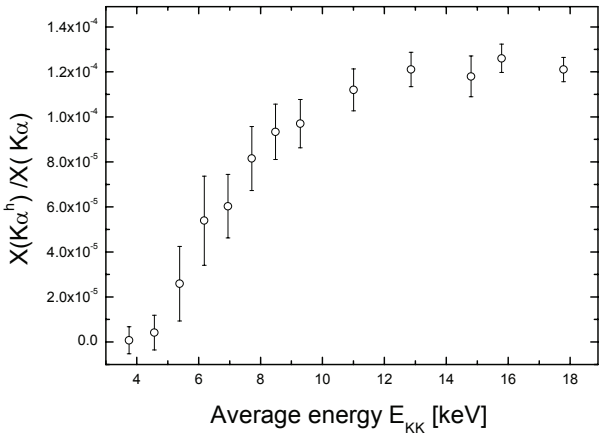

Fig. 27: Variation of the Al $K\alpha^h/K\alpha$ intensity ratio as a function of the electron average energy E_{KK}.

Chapter 4

Discussion

4.1. Results from synchrotron radiation measurements

4.1.1 $K\alpha_2^h$ Energy

The average energy of the photo-induced Al $K\alpha_2^h$ hypersatellite transition obtained from the fits of the line measured at different beam energies was found to be 1610.38 eV. Except for the measurements taken just above the threshold for which the hypersatellite statistics was poor, typical errors provided by the fits for the hypersatellite energy were ± 0.02 eV. However, if one considers the uncertainty related to the energy calibration of the spectrometer, a total error of about 0.04 eV is obtained. The standard deviation of the nine values considered for the calculation of the average energy (see Fig. 11) is similar, namely 0.05 eV. The single experimental value reported in the literature is the one measured by Keski-Rahkonen et al. [46]. In this study, an energy shift of the $K\alpha_2^h$ hypersatellite relative to the parent diagram line of 124.7 eV was found, in excellent agreement with their Dirac-Fock calculations. Using the $K\alpha_2$ transition energy of Deslattes et al. [43], this shift gives for the $K\alpha_2^h$ transition an energy of 1610.99(20), somewhat higher than our value. The discrepancy, although small, might be significant since the difference between the two experimental values amounts to 0.61 eV, bigger than the combined error of 0.21 eV. In their recent calculations, Costa et al. [53] computed an energy shift of 124.32 eV relative to the $K\alpha_{1,2}$ diagram lines, which corresponds, using once more the tabulated energies of Deslattes et al. [43], to a value of 1610.82 eV for the $K\alpha_2^h$ energy. This value is 0.44 eV higher than our result but consistent with it within the combined error if one assumes an uncertainty of 0.6 eV (0.5% of the calculated energy shift) for the theoretical value. Other available older theoretical predictions are 1608 eV [54] and 1627 eV [55].

Concerning the $K\alpha_1^h$ transition which is forbidden within the LS coupling scheme, Costa et al. [53] predict an energy of 1615.75 eV and a relative intensity with respect to the $K\alpha_2^h$ transition of only 0.0087. It is thus not surprising that the $K\alpha_1^h$ transition could not be detected in our measurements.

4.1.2 $K\alpha_2^h$ line width

For the line width of the $K\alpha_2^h$ hypersatellite transition, an average value of 1.88 eV with a standard deviation of 0.17 eV was obtained. Individual fit errors were typically ± 0.08 eV. Including the error of the instrumental broadening of the spectrometer (~ 0.06 eV), the total error for each measured line width is about 0.07 eV. No result is reported in the literature for this line width. We have thus compared our value with the approximation $3\Gamma_K+\Gamma_L$ suggested by Mossé et al. [41]. Using the values recommended by Campbell and Papp [45] for the level widths Γ_K and Γ_L of Al, Mossé's approximation gives a value of 1.15 eV, a width significantly smaller than our experimental result. Similar findings have been already reported by other groups for Cu, Si and Na targets [6, 56, 57].

Using MCDF calculations, Chen has shown that in light atoms (Z<25), the K-shell fluorescence yields for double K hole states are higher than those for single K holes states [49]. Therefore, as it was pointed out by Diamant et al. [6] and Hoszowska et al. [58], the line width of the $K\alpha^h$ transition is rather given by $\Gamma_{KK}+(\Gamma_K+\Gamma_L)$ where Γ_{KK} denotes the width of the initial $1s^{-2}$ vacancy state. Using the recommended Γ_K and Γ_L level widths of Campbell et al. [45] and the Γ_{KK} value extracted from the MCDF calculations of Chen [49], we obtain for the line width of the Al $K\alpha_2^h$ transition a value of 1.55 eV which is in better agreement with our experimental result.

4.1.3 $K\alpha_2^h L$ satellite

The hypersatellite spectra measured at photon beam energies of 3186 eV, 3318 eV and 3972 eV, respectively, are plotted in Fig. 28. In the 3972 eV spectrum, the peak located around 1621 eV corresponds to the L satellite line of the $K\alpha_2^h$ hypersatellite, i.e., to a transition with three vacancies in the initial and final sates. This peak appears in our measured spectra from a beam energy of 3742 eV and above. The energy given by the fit for the $K\alpha_2^h L$ satellite is 1621.36(11) eV, a value in satisfactory agreement with the result of 1621 eV reported by Keski-Rahkonen et al. in [46].

In first approximation, one could expect the intensity ratios I(KαL):I(Kα) and $I(K\alpha_2^h L):I(K\alpha_2^h)$ to be the same. This assumption, however, is not confirmed by our measurements since a value of 0.28(1) is obtained for the ratio $I(K\alpha_2^h L):I(K\alpha_2^h)$, which is four times bigger than the value of 0.074(1) reported by Mauron et al. for the ratio I(KαL):I(Kα) [44]. The same observation was done by Keski-Rahkonen et al. [46] who have reported ratios $I(K\alpha_2^h L):I(K\alpha_2^h)$ = 0.42(10) and I(KαL):I(Kα) = 0.098(5). It seems that this somewhat surprising result can be explained by theory. In a paper concerning measurements of

the Auger hypersatellites of Ne [59], the authors report indeed that, according to shake off calculations by C. Froese Fisher [60], the probabilities for observing L satellites in the diagram and hypersatellite K Auger spectra of neon are 16.7% and 46%, respectively.

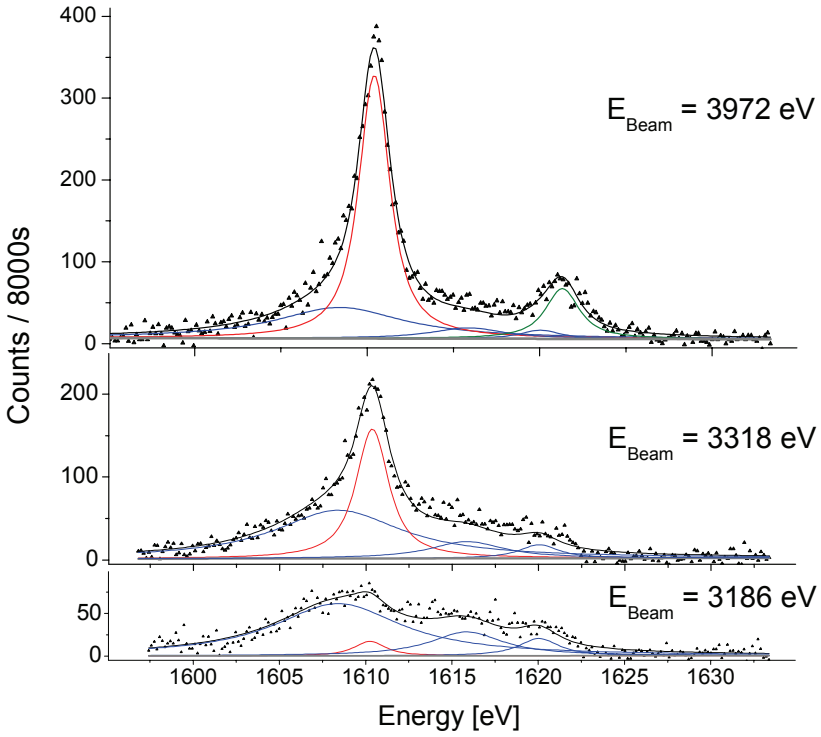

Fig. 28: Photo-induced $K\alpha^h$ hypersatellite spectra of Al at the indicated beam energies. The blue lines correspond to the $K\beta L^{(2)}$ satellite, the red line to the $K\alpha_2^h$ hypersatellite and the green line to the $K\alpha_2^h L$ hypersatellite satellite.

4.2 Results from electron measurements

The fits of the electron-induced $K\alpha^h$ spectra provided almost the same results for the energy and line width of the $K\alpha_2^h$ hypersatellite and the $K\alpha^h L/K\alpha^h$ yield ratio as those obtained from the photo-induced spectra. The corresponding values are quoted in Table 5. For the energies and line widths, indicated errors are total errors resulting from the energy calibration and instrumental broadening uncertainties (± 0.04 eV and ± 0.06 eV, respectively) and averaged fitting errors. For the latter, the square root divided by 9 of the sum of the nine squared individual fitting errors was taken. Except for the line widths in the electron measurements, the average fitting error was found to be small as compared to the calibration errors. For the ratios, quoted errors are those given by the fits. For the electron-induced $K\alpha^h$ spectra taken at 6

and 7 keV, in which the contribution of the x-rays arising from the Al oxide is considerable, the fitting errors were much higher so that the results corresponding to these two energies are not presented in Figs. 25 and 26 nor considered in the calculations of the average values of the hypersatellite energy and line width given in Table 5.

	Photon impact	Electron impact
$K\alpha_2^h$ energy	1610.38(4)	1610.35(7)
$K\alpha_2^h$ linewidth	1.88(7)	1.87(16)
$I(K\alpha_2^h L)/I(K\alpha^h)$	0.28(1)	0.20(4)

Table. 5: Comparison between the energies and linewidths of the $K\alpha_2^h$ hypersatellite and the $I(K\alpha_2^h L)/I(K\alpha_2^h)$ intensity ratios obtained with the photon and electron beams.

4.3 Double K-shell photo-ionization probabilities

The ratios of double to single K-shell photo-ionization cross sections (referred to in the literature as P_{KK}) were determined by means of Eq. (3). The obtained values are plotted in Fig. 29 as a function of the photon beam energy. As mentioned before, for the three measurements taken respectively at 3122 eV, 3186 eV and 3235 eV, no $K\alpha^h$ structure could be seen in the experimental spectra. Attempts to fit the invisible $K\alpha^h$ hypersatellite in these spectra by keeping fixed the energy and line width at the average values obtained from the fits of the spectra taken at higher energies resulted in fitted intensities that were consistent with zero within the fitting errors. Thus we conclude that the threshold energy to produce a double K-shell photo-ionization in Al should be higher than 3235 eV and below 3318 eV, the next higher beam energy for which the hypersatellite was observed. This is in agreement with GRASP calculations which predict a value of 3294 eV for the double 1s photo-ionization threshold.

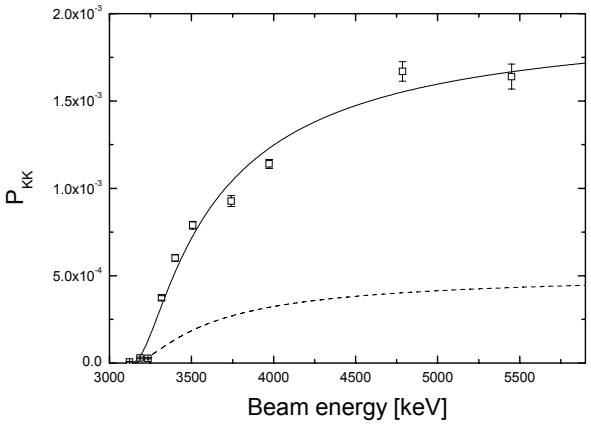

Fig. 29: Ratio of double to single K-shell photo-ionization cross sections as a function of the photon beam energy. The solid line represents the fit to the present experimental data using the Thomas model. The dashed line stands for predictions from the Thomas model using for $P_{KK}(\infty)$ a value corresponding to the asymptotic limit (see text for explanations).

It is well known that due to the combined influence of the knock-out (KO) and shake-off (SO) processes, the ratio of the double to single photo-ionization cross sections increases rapidly with excitation energy, levels off at a maximum value (broad maximum region), and then drops slowly with growing energy to reach an asymptotic value which corresponds to the photo-absorption shake probability. According to Kornberg's scaling law [61], the region of the broad maximum is reached at an excitation energy given approximately by 0.01 x Z^2 [keV] above the threshold energy. Assuming for the threshold energy the value calculated with the GRASP code, this corresponds for Al to a photon beam energy of 4984 eV. This estimation seems to be confirmed by our measurements since, as shown in Fig. 29, approximately the same experimental ratio P_{KK} was obtained at 4786 eV and 5451 eV.

Recently, Kanter et al. [10] assembled existing experimental ratios of double to single K–shell ionization cross sections of elements in the range $2 \leq Z \leq 47$ measured with photon impact and electron capture in both the broad maximum and asymptotic regions. They found that the Z dependence of the asymptotic ratio scales as Z^{-2} as suggested earlier by Forrey et al. [62] for He-like ions, while the broad maximum ratio scales as $Z^{-1.61}$. Extracting the corresponding Al values from their Fig. 10 reproduced below (Fig. 30), we have obtained a ratio for the broad maximum (named *Peak* in Fig. 30) of 1.85 10^{-3}, a value which agrees very well with our results (see Fig. 29), and an asymptotic ratio of 5.2 10^{-4}. The excitation energy required to reach the photo-absorption asymptotic limit is not yet well known. Previous measurements in He showed that the asymptotic limit is reached at a photon beam energy of about 3 keV [63], which is about 40 times the threshold energy for a double ionization of He. No similar photo-absorption measurements in the asymptotic region are available for higher Z elements but the shake probability of the second K electron can be directly measured in the double K-shell ionization following the nuclear EC decay since in this case one of the 1s electrons is absorbed in the nucleus and the second one is released through a shake process [10].

The Thomas model [64] has been used extensively in previous studies to interpret the double photo-ionization probability. Based on a time-dependent perturbation theory, the energy dependence of the double to single K shell photo-ionization is described in this model by the following simple formula:

$$P_{KK}(E) = P_{KK}(\infty) exp(-\frac{r^2 E_s^2}{15.32(E - E_{thr})}), \qquad (10)$$

where E_{thr} represents the double K-shell ionization threshold energy, E_s the shake energy, i.e., the energy needed to remove via a shake process the second electron, P_{KK} (∞) the shake

probability and r a typical distance travelled by the K photoelectron during the atomic potential change. In (10), the energies should be entered in eV and r in Å. As shown in [65], the distance r can be interpreted as the radius r_{max} (i.e., the radius at which the radial probability density peaks) of the shaken electron orbital in the ionic atom, i.e., in our case, as the radius r_{max} of the 1s orbital in Al^+.

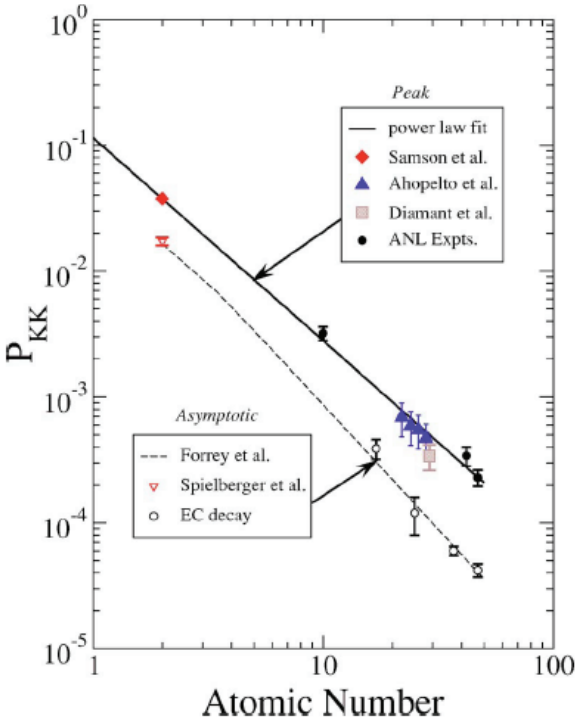

Fig. 30 (taken from Ref. [10]): Ratio of double to single K-shell photo-ionization as a function of the atomic number. The solid symbols are used for experiments carried out in the region of the predicted peak in the double photo-ionization cross section (◆ Ref. [16], ▲ Ref. [34], ■ Ref. [6]). The open symbols are used for measurements of the ratio in the asymptotic limit (▽ Ref. [66] and ○ Ref. [67, 68, 69, 70]), and the corresponding theoretical prediction of Forrey et al. [62] is shown as a dashed curve. The ● symbols are the experimental values of Kanter et al. [4, 9, 10] and the solid line is their $1/Z^{1.61}$ power-law fit [4].

Fig. 29 displays the fit of our measured data with the Thomas model. All parameters were let free in the fitting procedure except the shake energy that was fixed to the value of 1839 eV obtained using the (Z+1) approximation. The fit reproduces fairly well the data near the threshold and broad maximum regions and yields a value of 0.0446 Å for the 1s radius of Al^+, which is in satisfactory agreement with the MCDF prediction of 0.039 Å. In contrast to that, the fitted threshold energy was found to be 3074 eV, which is clearly lower than the estimation deduced from our measurements (3235 eV) and the value of 3294 eV given by the GRASP

code. This is, however, not really surprising because similar discrepancies for the threshold energy derived from the Thomas model were also observed by other groups [5, 7]. Furthermore, the Thomas model gives an asymptotic value of $2.1 \cdot 10^{-3}$ which is not only ~4 times higher than the asymptotic limit of $5.2\ 10^{-4}$ obtained using the Z^{-2} scaling law of Forrey et al. [62], but even exceeds our value of $1.65(5)\ 10^{-3}$ measured in the broad maximum region, where the KO effect contribution is expected to be predominant.

Several previous experimental studies had showed that indeed the Thomas model fails to fit the measured results because its simple formalism does not consider the KO mechanism contribution which is dominant at lower photon energies. The present work gives further evidence that theoretical models describing more accurately the mechanisms governing the double photo-ionization probability are needed. Recently, Schneider et al. [71, 72] developed a theoretical approach describing the knock-out mechanism as a quasi-classical process and the shake-off as a simple quantum process, and stated that there is no interference between the two processes. They applied their model to He and showed that the latter reproduced quite well the experimental data of Samson et al. [73]. Kanter et al. measured the double to single K-shell photo-ionization ratio in silver [10], and rescaling the SO and KO He calculations of Schneider [71, 72], they were able to fit quite well their silver data. However, as pointed out by Diamant et al. [7], the scaling of the calculations performed by Schneider et al. for He [71, 72] to heavier atoms might be not reliable. Schneider-like calculations for higher Z atoms would thus be welcome to clarify this problem. Assuming that the Thomas model [64] describes the shake process only and locking the asymptotic ratio $P_{KK}(\infty)$ to the value of $5.2 \cdot 10^{-4}$ obtained from the Z^{-2} scaling law of Forrey [62], we obtain the dashed curve of Fig. 29. The difference between the dashed curve and our experimental data corresponds then to the KO contribution since according to Schneider et al. [71, 72] there is no interferences between the KO and SO processes.

4.4 Comparison between the double to single K-shell ionization cross sections produced by photon and electron impact

In contrast to photons, direct multiple ionization is possible for impact with charged particles. A charged particle like for instance an electron can indeed interact sequentially with two bound electrons, producing a direct double ionization in the target atom. However, this TS2 process is negligibly small for charged projectiles with a ratio $Z/\upsilon < 0.05$ [23, 74, 75],

which is the case for the present measurements (Z stands for the projectile charge and υ for the collision velocity expressed in atomic units).

Fig. 31 shows the ratios of the double to single K-shell ionization cross sections as a function of the average electron energy $\overline{E}_{KK}$. Here again we have reached the broad maximum region, but data clearly beyond the maximum are missing due to the highest possible voltage of 20 kV of our electron gun. The ratio seems to reach a maximum value of 9.81 10^{-5} at an average electron energy of about 15 keV. In the spectrum measured at an electron beam energy of 5 keV, which corresponds to an average electron energy of 4.6 keV, a weak $K\alpha^h$ structure was observed but the fitted intensity was consistent with zero. Thus, for electrons, the threshold energy to produce a double K-shell ionization should be at least 4.6 keV, i.e., approximately 1 keV higher than the threshold for photon impact. This could be explained by the fact that a photon imparts almost its total energy to the photoelectron, while in electron impact ionization; the energy of the incoming electron is shared between the scattered and ejected electrons. One may thus indeed expect that the threshold energy of double ionization is somewhat higher in electron impact ionization than in photo-ionization [44].

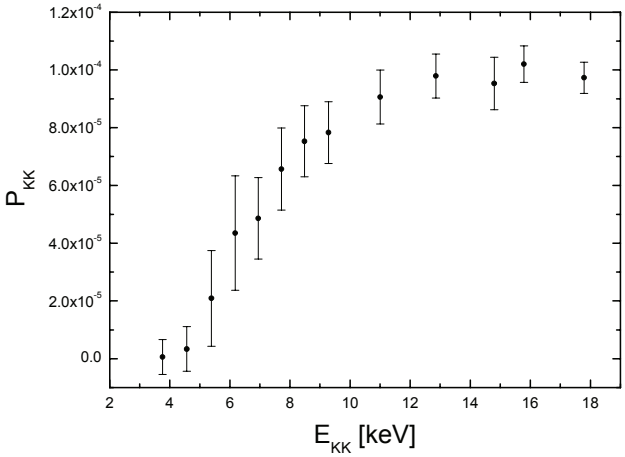

Fig. 31: Ratio of double to single K-shell ionization cross sections for electron impact as a function of the average electron energy $\overline{E}_{KK}$.

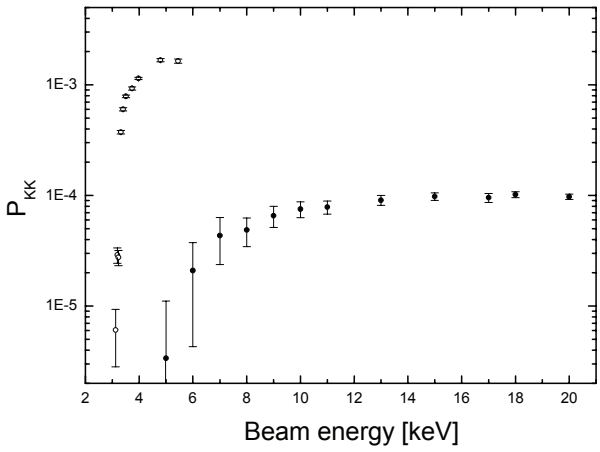

Fig. 32: Ratio of double to single K-shell ionization cross sections obtained in this work as a function of the beam energy (○: photon impact, ●: electron impact).

The maximum double to single K-shell ionization cross section ratio of 9.81 10^{-5} measured in the electron measurements is considerably lower than the corresponding maximum ratio of $1.65 \cdot 10^{-3}$ measured with photons. Similar dissimilarities were observed in He measurements where an asymptotic ratio of 1.7% was found [17, 57, 66] for photo-absorption, whereas the value obtained for charged particles impact[2] was only 0.27 % ([76] and references therein). On the other hand, Mauron et al. [44], in measurements of the KαL satellites in Al, Ca and Co induced by photon and electron impact, found that the cross section ratio of the photo-induced and electron-induced double KL to single K ionization were very similar. They were even able to estimate the small contribution of the TS2 process by comparing the photo-induced and electron-induced spectra. Likewise, Krause et al. [77] found that the KαL satellites of neon measured with both 3.2 keV electrons and 1.5 keV photons had the same intensity. It is well known that electron correlations in the same shell are stronger than those between electrons located in different shells. Thus, the fact that the double KL ionization cross sections for photons and electrons are similar, whereas the double K ionization cross sections are different, can be related to electron correlations. Actually, this statement is confirmed by the fact that in the present measurements quite different $K\alpha^h/K\alpha$ intensity ratios were observed for photons and electrons, whereas for the $K\alpha^h L/K\alpha^h$ intensity ratios similar values were obtained.

For charged particle impact, electrons are ejected with a continuous energy distribution and most of them leave the atom with small velocities comparable to their original orbital velocities [74]. Consequently the sudden approximation (SA) is no more valid [78, 79]. The same holds for photon impact at small energies: while SO is well defined in the framework of the SA model at the asymptotic energy limit, its meaning at low photon energies is not clear. If the outgoing electron leaves the atom with a low velocity, the corresponding atomic orbital has enough time to adapt to the new atomic potential. As a consequence, there will be no overlap between the initial and final wave functions and shake-off of a second electron will not occur. In other words, when the sudden approximation is no more valid since the velocity of the outgoing electron is too low, the meaning of the SO process which is in principle defined within the SA model is not clear.

Pattard et al [80] gave recently an excellent overview of the different SO definitions reported in the literature. Examining the SO probabilities in He from the threshold energy to the asymptotic limit in the photo-ionization case, they found that surprisingly the models of

[2] Experimental data for helium show that the double to single ionization asymptotic ratio does not depend on the projectile mass and charge (see [76] and references therein). The binding energy changes of the target electrons due to the presence of the charged projectile are negligible at high projectile velocities (see [79] and references therein).

Thomas [64] and Pattard [81], which depend respectively on v and v^2 (v denotes the photoelectron velocity) yield both approximately the same values as those predicted by the more recent model of Schneider et al. [71, 72] which does not depend on v. Although Thomas and Pattard models are based on more physical arguments, Pattard and co-workers were rather in favour of the Schneider's model because the latter is based on a mixed quantum-classical Ansatz which leads to a better separation of the SO and KO processes. They suggested also a ''working definition'' of the SO process at finite energies based on the same assumptions, specifying, however, that this definition is limited in its physical meaning. We come to the conclusion that for charged particle impact, the SO process contributes certainly to the double ionization probability, yet its physical meaning is not clear.

Concerning the KO process, it is well known that its amplitude depends strongly on the velocity of the primary electrons. At high photon energies, when the photoelectron velocity exceeds considerably the orbital velocity, the KO probability vanishes. In contrast to that, in the case of charged particle impact, most electrons continue to be ejected with small velocities, comparable to their original orbital velocities, independently of the projectile energy, so that the KO probability tends to a constant value at the asymptotic energy limit [79, 82, 83].

In a series of pioneering works aiming to investigate the relationship between the double ionization induced by photons and charged particles, McGuire and co-workers demonstrated that within the framework of the dipole approximation describing the photo-absorption process (i.e., photo-ionization ascribed solely to the photo effect without any contribution from the Compton effect), the ratio of double to single total ionization cross section for He in case of photon impact is much higher than that for charged particle impact [82], while being similar to the ratio of double to single differential cross section for charged particle impact corresponding to the same energy of the ejected electron [84].

Above McGuire's statement was confirmed experimentally by Cocke et al. [85] who performed measurements of the double to single ionization differential cross sections ratio of He bombarded with 1 and 3 MeV protons. By measuring the energy loss of the scattered protons, they were able to isolate the fast ejected electrons and they obtained ratios of about 2%, close to the ratios of double to single total cross section found in the case of photo-ionization for the same energies of the ejected electrons (600 eV and 900 eV) (Fig. 33). However, McGuire [74] pointed out that the conclusions of Cocke's measurements should be considered cautiously since at these proton energies a small contribution from the TS2 process is possible. Similar measurements were performed by Datz et al. [86]. Using 2, 3 and 6 MeV protons, they also found a ratio close to 2% at an energy transfer of about 1 keV (Fig. 33). Measurements of DeHaven et al. [87] yield, however, to a lower value for this ratio. Using

binary kinematics to compute the energy transfer corresponding to their measured proton scattering angles, they found over a large energy transfer range, a practically constant ratio of about 1.25%.

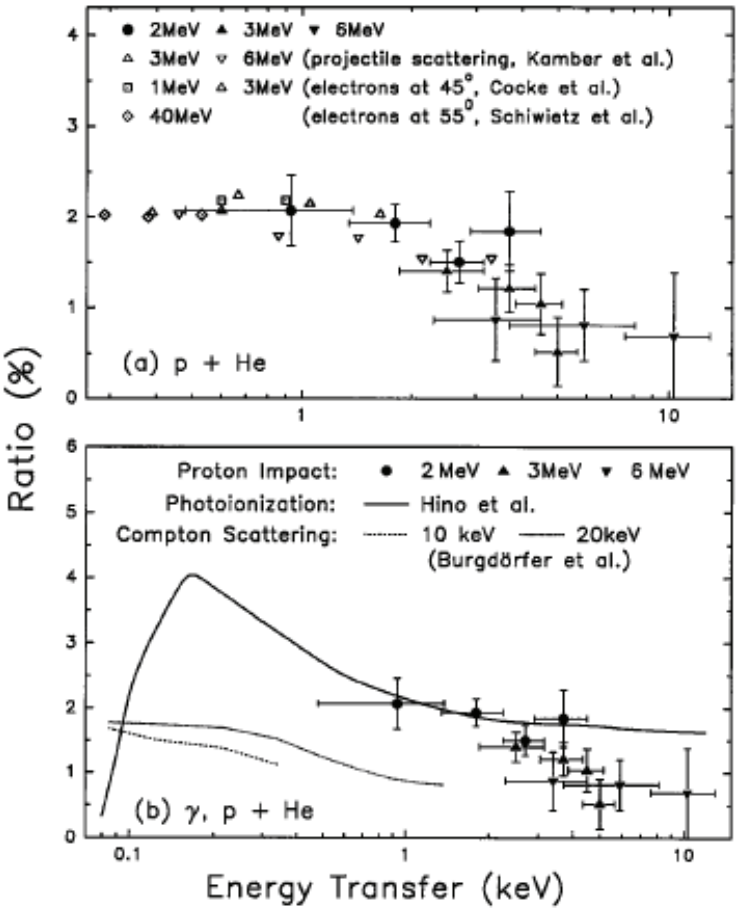

Fig. 33 (taken from Ref. [86]): Ratio of double to single ionization of He as a function of the energy transfer from the projectiles to He. The solid symbols are the experimental data of Datz et al. [86]. The open symbols are the experimental data for proton impact of Kamber et al. [88], Cocke et al. [85], and Schiwietz et al. [89]. Theoretical curves are from calculations for photo-ionization by Hino et al. [90] (solid line), and for Compton scattering by Burgdörfer et al. [91] (dashed lines).

As discussed by different authors [74, 86, 88, 92], even when the primary ejected electron after photo-absorption leaves the atom with the same energy as the one ejected after projectile impact ionization, the residual ion does not receive the same recoil momentum in both processes because the photo-absorption and projectile impact ionization processes probe different parts of the wave function in the target atom momentum space. In the case of photo-

absorption, momentum conservation requires that the momentum of the recoil ion mirrors the one of the ejected photoelectron, whereas for projectile impact ionization, the momentum lost by the projectile is transferred to the ejected electron and the ion is left with its initial momentum. This situation was suggested to be very similar to ionization induced by Compton scattering. Indeed, measurements in He using the COLTRIMS method have confirmed that the momentum distribution of the He^+ ions are very similar in Compton scattering and projectile impact ionization experiments [93]. On the theoretical side, Burgdörfer et al. [91] demonstrated within the Born approximation that for a given energy transfer to the primary ejected electron the ratio of double to single ionization for projectile impact is equal to the one obtained for Compton scattering.

Direct differential cross section measurements of Datz et al. [86] for He using fast protons as projectiles resulted in an asymptotic ratio of 0.8% (Fig. 33), which is lower than the value of 1.25% deduced from the kinematic measurements of DeHaven et al. [87]. No experimental data concerning the differential cross section ratio for Compton scattering are available in the literature. However, according to Burgdörfer et al. [91], the dominant contribution to the total cross section ratio for Compton scattering originates from large energy transfer. Using the COLTRIMS method, Spielberger et al. [94] found that in He the ratio of total cross section for Compton scattering in the energy range 40–100 keV appears to be 0.98 %, and they noted that over the investigated energy range, the asymptotic ratio was not yet reached. Comparing this value to the well established 1.7% asymptotic photo-absorption cross section ratio, Dorner et al. [93] concluded that ‘’the probability for shaking off the second electron differs significantly whether the first electron is removed by photo-absorption or by Compton scattering’’, in contradiction with a previous prediction of Mukoyama et al. [95], stating that ‘’in the sudden approximation, the shake probability is independent of the primary ionization mechanism ‘’.

Experimental data concerning the asymptotic ratios for Compton scattering and charged particle impact are not available for heavier elements. Our present measurements in Al do not reach the asymptotic region, but confirm that the cross section ratio in the broad maximum region is smaller for charged particle impact than for photon impact. Other measurements at higher energies are planned by our group in the near future.

Chapter 5

Concluding remarks and future perspectives

The energy dependence of the Kα hypersatellite x-ray spectrum of Al was measured, using synchrotron radiation and electron beams with energies ranging from 3122 eV to 5451eV for the synchrotron radiation and from 4 keV to 20 keV for the electrons. The measurements were performed by means of high-resolution x-ray spectroscopy, using a von Hamos crystal spectrometer. The threshold energies for the production of double 1s vacancy states were found to be comprised between 3235 eV and 3318 eV in the case of photo-ionization and at about 4.6 keV for the electron-induced ionization. No trace of the $K\alpha_1^h$ hypersatellite was detected in our measurements, due to the fact that this transition is forbidden by the E1 selection rules within the LS coupling scheme which prevails for light elements like Al. The $K\alpha_2^h$ transition energies and natural line widths were determined from the measurements performed with both particle types. Consistent values of 1610.38(10) and 1610.37(11) were obtained for the energies whereas for the widths, results of 1.88(10) eV and 1.87(17) eV, in near perfect agreement, too, were found. Since in light atoms the K shell fluorescence yields for double 1s vacancy states are higher than those of single 1s vacancy states, the $K\alpha_2^h$ natural line width was found to be better reproduced by the formula $\Gamma(K\alpha^h) = \Gamma_{KK}+(\Gamma_K+\Gamma_L)$, where Γ_x stands for the width of the x vacancy state, than by the standard Mossé formula $\Gamma(K\alpha^h) = 3\Gamma_K+\Gamma_L$ [41].

The energy dependence of the double K-shell ionization cross section was determined from the measured hypersatellite to diagram intensity ratios and the single K-shell ionization cross sections reported in the literature. The ratio of the double to single K-shell photo-ionization cross sections was found to reach the broad maximum at about 5 keV, in good agreement with the prediction of 4.984 keV derived from the Kornberg's scaling law [60]. For the maximum value of the ratio, a result of 1.65(5) 10^{-3} was obtained, which is also in good agreement with the value of 1.85 10^{-3} deduced from the $1/Z^{1.61}$ scaling law of Kanter et al. [10]. We have also shown in our study that the Thomas model does not fit properly the evolution of the measured double to single K-shell ionisation.

A detailed comparison between the data obtained by photo-ionization and electron impact was also done. Measurements performed by means of electron impact provide a maximum double to single K-shell ionization cross section ratio of $9.81 \cdot 10^{-5}$ considerably smaller than the corresponding ratio of $1.65 \cdot 10^{-3}$ obtained from the photon measurements. Likewise, a substantially lower double to single cross section ratio for charged particle impact ionization compared to photo-ionization was also found for He. These observations could be explained theoretically and confirmed by a variety of experiments.

Our objective for the near future is to determine the photo-absorption asymptotic ratio to get a complete understanding of the energy dependence of the double K-shell ionization cross section. These future investigations at higher energies should also allow us to determine the Compton scattering asymptotic ratio which is expected to be comparable to the value obtained by electron impact. Measurements of other elements heavier than Al are also planned.

Bibliography

[1] J. H. McGuire:
''Electron correlation dynamics in atomic collisions.''
Cambridge, UK:Cambridge University Press (1997).

[2] T.A. Carlson:
''Double electron ejection resulting from photo-ionization in the outermost shell of He, Ne, and Ar, and its relationship to electron correlation.''
Phys. Rev. **156** (1967) 142.

[3] F. W. Byron Jr and Ch. J. Joachain:
''Multiple ionization processes in helium.''
Phys. Rev. **164** (1967) 1.

[4] E. P. Kanter, R. W. Dunford, B. Krassig and S. H. Southworth:
''Double K-vacancy production in molybdenum by X-ray photoionization. ''
Phys. Rev. Lett. **83** (1999) 508.

[5] M. Oura, H. Yamaoka, K. Kawatsura, K. Takahiro, N. Takeshima, Y. Zou, R. Hutton, S.Ito, Y. Awaya, M. Terasawa, T. Sekioka and T. Mukoyama:
''Correlative multielectron processes in K-shell photoionization of Ca, Ti, and V in the energy range of 8–35 keV. ''
J. Phys. B **35** (2002) 3847.

[6] R. Diamant, S. Huotari, K. Hamalainen, C.C. Kao and M. Deutsch:
''Cu $K^h\alpha_{1,2}$ hypersatellites: suprathreshold evolution of a hollow-atom X-ray spectrum.''
Phys. Rev. A **62** (2000) 052519.

[7] R. Diamant, S. Huotari, K. Hamalainen, C.C. Kao and M. Deutsch:
''The evolution of inner-shell multielectronic x-rays spectra from threshold to saturation for low- to high- Z atoms. ''
Rad. Phys. Chem. **75** (2006) 143.

[8] R. Diamant, S. Huotari, K. Hamalainen, C.C. Kao and M. Deutsch:
''Diagram x-ray emission spectra of a hollow atom: The $Kh\alpha_{1,2}$ and $Kh\beta_{1,3}$ hypersatellites of Fe. ''
Phys. Rev. Lett. **91** (2003) 193001.

[9] S. H. Southworth, E.P Kanter, B. Krassig, L. Young, G.B. Armen, J. C. Levin, D. L. Ederer and M. H. Chen:
''Double K-shell photoionization of neon.''
Phys. Rev. A **67** (2003) 062712.

[10] E. P. Kanter, I. Ahmad, R. W. Dunford, D. S. Gemmel, B. Krassig, S. H. Southworth and L. Young:
''Double K-photoionization of silver.''
Phys. Rev. A **73** (2006) 022708.

[11] C. Dal Cappello, R. El Mkhanter, and P. A. Hervieux:
''Mechanisms of double ionization of atoms by electron impact.''
Phys. Rev. A **57** (1998) R693.

[12] A. Dorn, A. Kheifets, C. D. Schröter, C. Höhr, G. Sakhelashvili, R. Moshammer, J. Lower, and J. Ullrich :
''Appearance and disappearance of the second Born effects in the (e,3e) reaction on He.''
Phys. Rev. A **68** (2003) 012715.

[13] M. W. Carlen, B. Boschung, J.-Cl. Dousse, Z. Halabuka, J. Hoszowska, J. Kern, Ch. Rhême, M. Polasik, P. Rymuza and Z. Sujkowski:
''M-shell ionization resulting from near-central collisions of mid-Z atoms with 5.5-MeV/amu oxygen ions.''
Phys. Rev. A **49** (1994) 2524.

[14] S. L. Carter and H. P. Kelly:
''Double photoionization of helium.''
Phys. Rev. A **24** (1981) 170.

[15] T. Ishihara, K Hino and J. H. McGuire:
''Photoionization of two electrons in helium.''
Phys. Rev. A **44** (1991) R6980.

[16] J.A.R Samson:
''Proportionality of electron-impact ionization to double photoionization.''
Phys. Rev. Lett. **65** (1990) 2861.

[17] J. C. Levin, D. W. Lindle, N. Keller, R. D. Miller, Y. Azuma, N. Berrah Mansour, H. G. Berry, and I. A. Sellin:
''Measurement of the ratio of double-to-single photoionization of helium at 2.8 keV using synchrotron radiation.''
Phys. Rev. Lett. **67** (1991) 968.

[18] J. A. R. Samson, Chris H. Greene and R. J. Bartlett:
Comment on ''Measurement of the ratio of double-to-single photoionization of helium at 2.8 keV using synchrotron radiation.''
Phys. Rev. Lett. **71** (1993) 201.

[19] R. Dörner, H. Schmidt-Böcking, T. Weber, T. Jahnke, M. Schöffler, A. Knapp, M. Hattass, A. Czasch, L. Ph. H. Schmidt and O. Jagutzki:
''Double ionization by one and many photons.''
Rad. Phys. Chem. **70** (2004) 191.

[20] J. P. Briand, P. Chevalier, M. Tavernier, and A. Touati:
''Observation of K Hypersatellites and KL satellites in the x-ray spectrum of doubly K-ionized Gallium.''
Phys. Rev. Lett. **27** (1971) 777.

[21] J. P. Briand, P. Chevalier, A. Chetioui, A. P. Rozet, M. Tavernier, and A. Touati:
''Correlation effects in double-K-vacancy production.''
Phys. Rev. A **23** (1980) 39.

[22] T. Åberg, J. P. Briand, P. Chevalier, A. Chetioui, A. P. Rozet, M. Tavernier, and A. Touati:
''The Kα hypersatellite ratio in intermediate coupling.''
J. Phys. B **9** (1976) 2815.

[23] J. A. Tanis, R. D. DuBois, A. S. Schlachter:
Comment on ''Double and single ionization of helium by high-velocity N^{7+} ions''.
Phys. Rev. Lett.**68** (1992) 897.

[24] H. Knudsen, L. H. Andersen, P. Hvelplund, G. Astner, H. Cederquist, H. Danared, L. Liljeby and K. –G. Rensfelt:
''An experimental investigation of double ionisation of helium atoms in collisions with fast, fully stripped ions.''
J. Phys. B **17** (1984) 3545.

[25] M. Kobal, M. Kavčič, M. Budnar, J.-Cl. Dousse, Y.-P. Maillard, O. Mauron, P.-A. Raboud and K. Tökési:
''Double- K -shell ionization of Mg and Si induced in collisions with C and Ne ions.''
Phys. Rev. A **70** (2004) 062720.

[26] T. Åberg, K.A. Jamison, and P. Richard:
''Origin of two-electron, one-photon K X-ray transitions.''
Phys. Rev. Lett. **37** (1976) 63.

[27] J. Auerhammer, H. Genz, A. Kumar, and A. Richter:
''Two-electron–one-photon transition in aluminium following double-K-shell ionization.''
Phys. Rev. A **38** (1988) 688.

[28] W. Wolfli, Ch. Stoller, G. Bonani, M. Suter, and M. Stockli:
''Two-electron-one-photon transitions in heavy-ion collisions. ''
Phys. Rev. Lett. **35** (1975) 656.

[29] W. Wolfli et al.:
In the Proceedings of the 2nd International Conference on Inner-Shell Ionization Phenomena. Edited by W. Melhorn and R. Brenn, Freiburg, (1976) p. 272.

[30] S. I. Salem, A. Kumar, B. L. Scott and R. D. Ayers:
''Splitting of the Two-Electron, One-Photon Transitions in Fe and Co.''
Phys. Rev. Lett. **49** (1982) 1240.

[31] S. I. Salem, A. Kumar and B. L. Scott:
''Two-electron, one-photon transitions in Cr, Fe, Co, and Cu.''
Phys. Rev. A **29** (1984) 2634.

[32] M. H. Chen, B. Crasemann and H. Mark:
''Effect of the Breit interaction on K x-ray hypersatellite spectra.''
Phys. Rev. A **25** (1982) 391.

[33] B. Boschung, J,-Cl. Dousse, B. Galley, Ch. Herren, J. Hoszowska, J. Kern, Ch. Rhême, Z. Halabuka, T. Ludziejewski, P.Rymuza, Z. Sujkowski and M. Polasik:
''Kα hypersatellite lines of medium-mass atoms induced by 100-MeV 4He^{2+} ions.''
Phys. Rev. A **51** (1994) 3650.

[34] J. Ahopelto, E, Rantavuori, O. Keski-Rahkonen:
''Kα hypersatellite spectra in photon excitation and K shell double photoionization cross section for transition metals Ti, Cr, Fe, Ni.''
Phys. Scr. **20** (1979) 71.

[35] K. Ilakovac , M. Vesković, V. Horvat, S. Kauić:
''Hypersatellite and satellite transitions in xenon atoms.''
Phys. Rev. A **42** (1990) 3984.

[36] Y. Isozumi, Ch. Friançon and R.J. Walen:
''Double K-hole creation accompanying K-electron capture decay of ^{131}Cs.''
Phys. Rev. C **28** (1982) 3070.

[37] N. Cue, W. Scholz, and A. Li-Scholz:
Phys. Lett. A **63** (1977) 54.

[38] V. Horvat, K. Ilakovac:
''Decay of the double–K-shell-vacancy state in silver atoms created in the decay of ^{109}Cd.''
Phys. Rev. A **31** (1985) 1543.

[39] S. I. Salem:
''Kα hypersatellites of Mo.''
Phys. Rev. A **21** (1980) 858.

[40] J. P Briand et al.:
Phys. Fenn. **9** (1974) 409.

[41] J.P. Mossé, P. Chevallier and J.P. Briand:
Z. Phys. A **322** (1985) 207.

[42] J. S. Levenger:
''Effects of radioactive disintegrations on inner electrons of the atom.''
Phys. Rev. **90** (1953) 11.

[43] R. D. Deslattes, E. G. Kessler, Jr, P. Indelicato, L. de Billy, E. Lindroth and J. Anton:
''X-ray transition energies: new approach to a comprehensive evaluation.''
Rev. Mod. Phys. **75** (2003) 35.

[44] O. Mauron and J.-Cl. Dousse:
''Double KL ionization in Al, Ca, and Co targets bombarded by low-energy electrons.''
Phys. Rev. A **66** (2002) 042713.

[45] J.L Campbell and T. Papp:
''Widths of the atomic K-N_7 levels.''
At. Data Nucl. Data Tables **77** (2001) 1.

[46] O. Keski-Rahkonen, E. Mikkola, K. Reinikainen and M. Lehkonen:
''The Kβ X-ray satellite spectra in sodium, magnesium and aluminium: the $K\alpha^h$ hypersatellite spectrum in aluminium.''
J. Phys. C **18** (1985) 2961.

[47] M. Fritsch, C. C. Kao, K. Hämäläinen, O. Gang1, E. Förster, and M. Deutsch:
''Evolution of the Cu $K\alpha_{3,4}$ satellites from threshold to saturation.''
Phys. Rev. A 57 (1997) 1686.

[48] http://physics.nist.gov/PhysRefData/Xcom/Text/XCOM.html

[49] M. H. Chen:
''Auger transition rates and fluorescence yields for the double-K-hole state.''
Phys. Rev. A **44** (1991) 239.

[50] E. Storm and H.I. Israel:
''Photon cross sections from 1 keV to 100 MeV for elements Z=1 to Z=100.''
Nucl. Data Tables 7 (1970) 565.

[51] http://physics.nist.gov/PhysRefData/Star/Text/contents.html

[52] M. Liu, Z. An, C.Tang, Z. Luo, X. Peng, and X. Long:
''Experimental Electron-Impact K-Shell Ionization Cross Sections''
At.Data Nucl. Data Tables **76** (2000) 213, and references therein.

[53] A. M. Costa, M. C. Martins, J. P. Santos, P. Indelicato and F. Parente:
''Relativistic calculation of Kα hypersatellite line energies and transition probabilities for selected atoms with 12≤Z≤80.''
J. Phys. B **40** (2007) 57.

[54] M. Gavrila and J. M. Hansen:
''Calculation of transition probabilities for two-electron one-photon and hypersatellite transitions for ions with two vacancies in the K shell.''
J. Phys. B **11** (1978) 1353

[55] T. K. Mukherjee and P. K. Mukherjee
Z. Phys. D **42** (1997) 29

[56] M. Kavčič, K. Tökési:
''Double 1s shell ionization of Si induced in collisions with 1–3 MeV protons.''
Phys. Rev. A **72** (2005) 062704.

[57] J. Auerhammer, H. Genz, G. Kilgus, A. Kumar, and A. Richter:
''Electron-impact energy dependence of the sodium K-shell double-ionization cross section: A study of hypersatellite spectra.''
Phys. Rev. A **35** (1987) 4505.

[58] J.Hoszowska et al.
''Hollow Mg: Photon energy dependence of double 1s ionization''
In preparation.

[59] Ž. Šmit, M. Žitnik, L. Avaldi, R. Camilloni, E. Fainelli, A. Mühleisen, and G. Stefani:
''Auger hypersatellites in Ne atoms induced by electron impact.''
Phys. Rev. A **49** (1993) 1480.

[60] C. Foese Fisher:
''The Hartree-Fock Method for Atoms.''
Willey Interscience, New York (1977).

[61] M. A. Kornberg and J. E. Miraglia:
''Scaling laws in double photoionization.''
Phys. Rev. A **49** (1994) 5120.

[62] R. C. Forrey, H. R. Sadeghpour , J. D. Baker, J. D. Morgan, III and A. Dalgarno:
''Double photoionization of excited 1S and 3S states of the helium isoelectronic sequence.''
Phys. Rev. A **51** (1995) 2112.

[63] J. C. Levin, G. Bradley Armen, and I. A. Sellin:
''Photoionization and Compton Double Ionization of Helium from Threshold to 20 keV.''
Phys. Rev. Lett. **76** (1996) 1220.

[64] T. D. Thomas:
''Transition from adiabatic to sudden excitation of core electrons.''
Phys. Rev. Lett. **52** (1984) 417.

[65] P.-A. Raboud, M. Berset, J.-Cl. Dousse, Y.-P. Maillard, O. Mauron, J. Hoszowska, M. Polasik, J. Rzadkiewicz:
''Energy-dependent KL double photoexcitation of argon.''
Phys. Rev. A **65** (2002) 062503.

[66] L. Spielberger et al.:
''Separation of Photoabsorption and Compton Scattering Contributions to He Single and Double Ionization.''
Phys. Rev. Lett. **74** (1995) 4615.

[67] S.K. Ko, H.J. Cho, S.K. Nha:
''X-ray spectroscopy in the EC nucleus.''
Nucl. Phys. A **641** (1998) 49.

[68] J. A. Miskel, M. L. Perlman:
''Double vacancies in the K shell associated with K-electron capture in ^{37}Ar.''
Phys. Rev. **94** (1954) 1683.

[69] J. P. Briand, P. J. Chevallier, A. Johnson, J.P. Rozet, M. Tavernier, A. Touati :
''Experimental determination of the energy of K hypersatellite lines for various elements.''
Phys. Lett. A **49** (1974) 51.

[70] G. Schupp, H.J. Nagy:
''Double K-shell ionization in the electron capture decay of ^{85}Sr.''
Phys. Rev. C **29** (1984) 1414.

[71] T. Schneider, P. L. Chocian, and J. M. Rost:
''Separation and identification of dominant mechanisms in double photoionization.''
Phys. Rev. Lett. **89** (2002) 073002.

[72] T. Schneider and J. M. Rost:
''Double photoionization of two-electron atoms based on the explicit separation of dominant ionization mechanisms.''
Phys. Rev. A **67** (2003) 062704.

[73] J. A. R. Samson, W. C. Stolte, Z.-X. He, J. N. Cutler, Y. Lu and R. J. Bartlett:
''Double photoionization of helium.''
Phys. Rev. A **57** (1998)1906.

[74] J. H. McGuire, N. Berrah, R. J. Bartlett, J. A. R. Samson, J. A. Tanis, C. L. Cocke and A. S. Schlachter:
''The ratio of cross sections for double to single ionization of helium by high energy photons and charged particles.''
J. Phys. B **28** (1995)913.

[75] A. S. Schlachter and J. A. Tanis:
Comment on "High-Velocity Limit for the Ratio of Helium Double-to-Single Ionization for Highly Charged, Bare-Ion Impact".
Phys. Rev. Lett. **73** (1994) 3596.

[76] J. Ullrich, R. Moshammer, H. Berg, R. Mann, H. Tawara, R. Dörner, J. Euler, H. Schmidt-Böcking, S. Hagmann, C. L. Cocke, M. Unverzagt, S. Lencinas, and V. Mergel:
''High-velocity limit for the ratio of helium double-to-single ionization for highly charged, bare-ion impact.''
Phys. Rev. Lett. **71** (1993) 1697.

[77] M. O. Krause et al. :
Phys. Lett A **31**(1970) 81.

[78] S. T. Manson, R. D. DuBois and L. H. Toburen:
''Multiple-ionization mechanisms in fast proton-neon collisions.''
Phys. Rev. Lett. **51** (1983) 1542.

[79] L. H. Andersen, P. Hvelplund, H. Knudsen, S. P. Moller, A. H. Sorensen, K. Elsener, K.-G. Rensfelt, and E. Uggerhoj:
''Multiple ionization of He, Ne, and Ar by fast protons and antiprotons.''
Phys. Rev. A **36** (1987) 3612.

[80] T. Pattard, T. Schneider and J. M. Rost:
''On the role of shake-off in single-photon double ionization.''
J. Phys. B **36** (2003) L189.

[81] T. Pattard and J. Burgdörfer:
''Half-collision model for multiple ionization by photon impact.''
Phys. Rev. A **64** (2001) 042720.

[82] J H McGuire:
''High-velocity limits for the ratio of double to single ionisation by charged particles and by photons.''
J. Phys. B **17** (1984) L779.

[83] L. H. Andersen, P. Hvelplund, H. Knudsen, S. P. Møller, K. Elsener, K. -G. Rensfelt, and E. Uggerhøj:
''Single and double ionization of helium by fast antiproton and proton impact.''
Phys. Rev. Lett **57** (1986) 2147.

[84] S. T. Manson and J. H. McGuire:
''Ratio of double to single ionization of helium: The relationship between ionization by photons and by bare charged particles.''
Phys. Rev. A **51** (1995) 400.

[85] C. L. Cocke, R. Dörner, A. D. Gonzalez, and E. Horsdal-Pedersen:
''Abstracts of XVIII International Conference on the Physics of Electronic and Atomic Collisions.''
Edited by T. Andersen et al. (IFA, arhus University, Aarhus, 1993) p. 845.

[86] W. Wu, S. Datz, N. L. Jones, H. F. Krause, B. Rosner, K. D. Sorge, and C. R. Vane:
''Double Ionization of He by Fast Protons at Large Energy Transfer.''
Phys Rev Lett. **76** (1996) 4324.

[87] W. R. DeHaven, C. Dilley, A. Landers, E. Y. Kamber and C. L. Cocke:
''Measurement of the ratio of differential cross sections for double and single ionization of He by (4–10)-MeV protons.''
Phys. Rev. A **57** (1998) 292.

[88] E. Y. Kamber, C. L. Cocke, S. Cheng, and S. L. Varghese:
''Angular Distribution of Fast Protons from Singly and Doubly Ionizing Collisions with He.''
Phys. Rev. Lett. **60** (1988) 2026.

[89] G. Schiwietz, G. Xiao, P. L. Grande, B. Skogvall, R. Köhrbrück, B. Sulik, K. Sommer, A. Schmoldt, U. Stettner, and A. Salin:
''Double Ionization of Helium by 40 MeV Protons.''
Europhys. Lett. **27** (1994) 341.

[90] K. -I. Hino, P. M. Bergstrom and J. H. Macek:
''Contribution of Compton scattering to the double ionization of helium.''
Phys. Rev. Lett. **72** (1994) 1620.

[91] J. Burgdörfer, L. R. Andersson, J. H. McGuire and T. Ishihara:
''Inelastic atomic scattering by high-energy photons and charged particles.''
Phys. Rev. A **50** (1994) 349.

[92] L. Végh and J. Burgdörfer:
''Shake off induced by fast charged projectiles.''
Phys. Rev. A **42** (1990) 655.

[93] R. Dörner, V. Mergel, O. Jagutzki, L. Spielberger, J. Ullrich, R. Moshammer, H. Schmidt-Böcking:
''Cold Target Recoil Ion Momentum Spectroscopy: A 'Momentum Microscope' to View Atomic Collision Dynamics.''
Physics Reports **330** (2000) 95.

[94] L. Spielberger et al.:
''Cross-section ratio of double to single ionization of helium by Compton scattering of 40–100-keV x rays.''
Phys. Rev. A. **59** (1999) 371.

[95] T Mukoyama, Y. Ito and K. Taniguchi:
''Atomic excitation and ionization os the result of inner-shell vacancy creation.''
X-Ray Spectrom.**28** (1999) 491.

Acknowledgements

This work was carried out at the department of Physics, University of Fribourg (Switzerland). I would like to express my sincere gratitude to my supervisor Prof. Dr. Jean-Claude Dousse who gave me the opportunity to perform this work in his research group. I am especially grateful to him for proofreading my thesis, for his support and great supervision, and for just about everything during these years.

I'm very thankful to Prof. Dr. Gunther L. Borchert, Prof. Dr. Dionys Baeriswyl and Dr. Joanna Hoszowska for their kind acceptance to be members of my PhD committee and for their careful reading of my thesis and useful comments.

Financial support from the Swiss National Science Foundation and the University of Fribourg is greatly acknowledged.

I would like to thank Michel Berset for all the great help and support during measurements both at our lab and at the ESRF, for taking the nice spectrometer pictures, for always being friendly and for always having a perfect solution for all spectrometer and computer related issues.

I owe particular thanks to Dr. Joanna Hoszowska for helping me out in data analysis and in various matters…, for her support during the thesis writing period, and for always being very helpful and having time for questions and discussions.

I would also like to thank Yves-Patrik Maillard for his friendship, for always arranging our group's social activities and for all the help and great company during these years.

Many thanks to all past and present members of the FRAP group for creating a pleasant and friendly atmosphere and for always being helpful and supportive. '' Un très grand Merci'' to Sebastien Baechler, Olivier Mauron and Pierre-Alexandre Raboud. Special ''Dziękuję'' to Monika and Jakub Szlachetko,''Grouss Merci'' to Yves Kayser and many 谢谢 to Wei Cao for the nice Chinese gifts I received from him.

I wish to add special thanks to the fantastic ladies in the secretariat for the excellent administrative support. I especially thank Eliane Esseiva for always, with a smile, answering

my questions. Many thanks as well to the mechanical and electronics workshop and to all people at the Physics department for making it such a great place to work.

My deep and sincere gratitude goes to all my friends, especially Fatima and Bea Gigger, Aicha and Peirre-Alain Dessonnaz, Asmaa El Hannani, Samira Makham, Fatima Mastour, Hayat Mounasser, Dalila Mekhaldi, Soraya and Ghita Kouadri Mostéfaoui, Caterina Pedrioli and Sabrina for a lot of good times, for support and help whenever needed, for encouraging phone calls and for the things I got from my mailbox •.

Finally, my most sincere gratitude goes to my parents, sisters, brother, brothers-in-law and nieces for all the endless love and care, and for the constant support and encouragement throughout my entire life. I'm especially grateful to my brother for being such a nice, fun and caring person, you are simply the best!

To my parents:

أهدي هذه الاطروحة الى والدي العزيزين مع متمنياتي لهما بالصحة.
كما اقدم لهما شكري الخاص لمساندتهما الدائمة لي.

Curriculum Vitae

Education and Qualifications

2003-2007: PhD student in experimental atomic physics and teaching assistant.
Physics department – University of Fribourg – Switzerland.

2000-2002: Master in physics.
University of Hassan II – Casablanca – Morocco.

1996-1999: Bachelor in physics.
University of Mohammed V – Rabat – Morocco.

1994-1996: Diploma of Mathematics.
Classes préparatoires – Mohammedia – Morocco.

1990-1994: Mathematical gymnasium.

List of publications

Refereed articles

• J. Szlachetko, M. Berset, J.-Cl. Dousse, K. Fennane, M. Szlachetko ; R. Barrett, J. Hoszowska ; A. Kubala-Kukus, M. Pajek :
''Resonant x-ray Raman scattering for Al, Si and their oxides.''
Proc. 4th Conference on Synchrotron Radiation in Materials Science, Grenoble, France, Aug. 23-25, 2004.
Nucl. Instrum. Meth. Phys. Res. B 238 (2005) 353.

• J. Szlachetko, J.-Cl. Dousse, J. Hoszowska, M. Pajek, R. Barrett, K. Fennane, A. Kubala-Kukus, M. Szlachetko:
''High-resolution study of x-ray resonant Raman scattering at the K-edge of silicon.''
Phys. Rev. Lett. 97 (2006) 073001.

• J. Szlachetko, J.-Cl. Dousse, M. Berset, K. Fennane, and M. Szlachetko; J. Hoszowska and R. Barrett; M. Pajek, and A. Kubala-Kukus:
''High-resolution study of the x-ray resonant Raman scattering process around the 1s absorption edge for aluminium, silicon and their oxides.''
Phys. Rev. A 75 (2007) 022512.

• K. Fennane, J.-Cl. Dousse, M. Berset, J. Hoszowska, J. Szlachetko, M. Szlachetko, M. Kavčič, W.Cae:
''Double K-shell ionization of Aluminium induced by photon and electron impact.''
(In preparation)

• K. Fennane, J.-Cl. Dousse, J.L. Campbell, M. Berset, J. Hoszowska:
''Re-examination of $M_{2,3}$ atomic-level widths of elements $69 \leq Z \leq 95$.''
(In preparation)

Conference abstracts

• K. Fennane, M. Berset, J.L. Campbell, J.-Cl. Dousse, P.-A. Raboud:
''Reexamination of $M_{2,3}$ atomic-levelwidths of elements $69 \leq Z \leq 95$.''
20th Int. Conf. on X-Ray and Inner-Shell Processes, Melbourne, Australia, July 4-8 2005, book of abstr., p. 151.

• J. Szlachetko, R. Barrett, M. Berset, J.-Cl. Dousse, K. Fennane, J. Hoszowska, A. Kubala-Kukus, Y.-P. Maillard, M. Pajek, M. Szlachetko:
''Resonant Raman scattering for Al, Si and their oxides.''
Fourth Conference on Synchrotron Radiation in Materials Science, Aug. 23-25, 2004, Grenoble, France, book of abstr.

• J. Hoszowska, J.-Cl. Dousse, M. Berset, K. Fennane, Y.-P. Maillard, J. Szlachetko and M. Szlachetko:
''Size-dependent Kβ resonant x-ray emission spectra of MnO2 nanopowder.''
15th ESRF Users' Meeting, Feb. 8-9, 2005, ESRF, Grenoble, France.

• J. Szlachetko, R. Barrett, M. Berset, J.-Cl. Dousse, K. Fennane, J. Hoszowska, A. Kubala-Kukus, M. Pajek, M. Szlachetko:
''X-ray resonant Raman scattering in Si at 1s absorption edge.''
15th ESRF Users' Meeting, Feb. 8-9, 2005, ESRF, Grenoble, France

• J. Hoszowska, M. Berset, J.-Cl. Dousse, K. Fennane, J. Szlachetko, M. Szlachetko:
''Size-dependent resonant K x-ray emission spectra of Mn and Fe oxide nanopowders.''
20th Int. Conf. on X-Ray and Inner-Shell Processes, Melbourne, Australia, July 4-8 2005, book of abstr., p. 13.

• J.-Cl. Dousse, J. Hoszowska, M. Berset, K. Fennane, J. Szlachetko, M. Szlachetko:
''First high-resolution study of the double 1s photoionization of Mg.''
20th Int. Conf. on X-Ray and Inner-Shell Processes, Melbourne, Australia, July 4-8 2005, book of abstr., p. 58.

• J. Szlachetko, R. Barrett, M. Berset, J.-Cl. Dousse, K. Fennane, J. Hoszowska, A. Kubala-Kukus, M. Pajek, M. Szlachetko:
''X-ray resonant Raman scattering in Si and SiO2 at Si K absorption edge.''
XXIV International Conference on Photonic, Electronic and Atomic Collisions (ICPEAC), July 20-26, 2005, Rosario, Argentina, book of abstr.

• J. Szlachetko, R. Barrett, M. Berset, J.-Cl. Dousse, K. Fennane, J. Hoszowska, A. Kubala-Kukus, M. Pajek., M. Szlachetko:
''First high-resolution observation of x-ray resonant Raman scattering in Si at 1s absorption edge.''
International Workshop on Photoionization IWP2005, Campinas, Brazil, July 27-31, 2005, book of abstr.

• J. Szlachetko, R. Barrett, M. Berset, J.-Cl. Dousse, K. Fennane, J. Hoszowska, A. Kubala-Kukus, M. Pajek., M. Szlachetko:
''High-resolution study of the x-ray resonant Raman scattering forAl, Si, Al2O3 and SiO2 in the region of the K-absorption edge.''
International Workshop on Photoionization IWP2005, Campinas, Brazil, July 27-31, 2005, book of abstr.

• J. Slachetko, R. Barrett, M. Berset, J.-Cl. Dousse, K. Fennane, J. Hoszowska, A. Kubala-Kukus, M. Pajek, M. Szlachetko:
''X-ray resonant Raman scattering in Si and SiO2 at Si K-absorption edge.''
8th International School and Symposium on Synchrotron Radiation in Natural Sciences (ISSRNS06), June 12-17, 2006, Zakopane, Poland, book of abstr.

• J.-Cl. Dousse, M. Berset, W. Cao, K. Fennane, M. Kavcic, J. Szlachetko and M. Szlachetko; J. Hoszowska:
''Double K-shell photoionization of Magnesium and Aluminium.''
European Conference on X-Ray Spectrometry EXRS 2006, Paris, France, July 19-23, 2006, book of abstr., O1-1, p. 4.

• J. Hoszowska, J.-Cl. Dousse, M. Berset, W. Cao, K. Fennane, M. Kavcic, J. Szlachetko, and M. Szlachetko:
''Double 1s photoionization of Ca and V beyond maximum.''
European Conference on X-Ray Spectrometry EXRS 2006, Paris, France, July 19-23, 2006, book of abstr. O1-4, p. 7.

• J. Szlachetko, R. Barrett, M. Berset, J.-Cl. Dousse, K. Fennane, M. Szlachetko, J. Hoszowska, A. Kubala-Kukus, M. Pajek:
''X-ray resonant Raman scattering below the Si K-absorption edge.''
European Conference on X-Ray Spectrometry EXRS 2006, Paris, France, July 19-23, 2006, book of abstr. O10-2, p. 64.

• M. Pajek, A. Kubala-Kukus, J. Szlachetko, M. Berset, J.-Cl. Dousse, K. Fennane, M. Szlachetko, R. Barrett, J. Hoszowska:
''X-ray resonant Raman scattering in Si and SiO2 below K-shell absorption edge.''
12th Conference on Total Reflection X-Ray Fluorescence Analysis and Related Methods TXRF 2007, June 18-22, 2007, Trento, Italy.

• J. Hoszowska, J.-Cl. Dousse, M. Berset, W. Cao, K. Fennane, J. Szlachetko, and M. Szlachetko:
''Photon energy dependence of the ratio of double to single K-shell ionization for magnesium, aluminium and silicon.''
XXV International Conference on Photonic, Electronic and Atomic Collisions (ICPEAC), July 25-31, 2007, Freiburg, Germany, book of abstr. p. We-012.

• J. Szlachetko, R. Barrett, M. Berset, J.-Cl. Dousse, K. Fennane, J. Hoszowska, A. Kubala-Kukus, M. Pajek, and M. Szlachetko:
''High-resolution study of the x-ray resonant Raman scattering process around the K-absorption edge for Al, Al2O3, Si and SiO2.''
XXV International Conference on Photonic, Electronic and Atomic Collisions (ICPEAC), July 25-31, 2007, Freiburg, Germany, book of abstr. p. We-053.